DYNAMIC FAILURE BEHAVIOR OF CERAMICS
UNDER MULTIAXIAL COMPRESSION

Thesis by

Weinong Chen

In Partial Fulfillment of the Requirements

for the Degree of

Doctor of Philosophy

California Institute of Technology

Pasadena, California

1995

(Submitted May 25, 1995)

To my family

Acknowledgments

Abstract

An experimental technique has been developed that is capable of (1) dynamically loading the specimen in multiaxial compression; (2) controlling the stress state in the specimen in the range from uniaxial stress to uniaxial strain; and (3) allowing the recovery of the sample after loaded by a single, well defined pulse for the characterization of the failure mode. In this technique, cylindrical ceramic specimens were loaded in the axial direction using a split Hopkinson pressure bar modified to apply a single loading pulse, and were confined laterally either by shrink fit sleeves, or by eletro-magnetic force.

Quasi-static and dynamic multiaxial compression experiments have been performed on a machinable glass ceramic, Macor, and a monolithic engineering ceramic, sintered aluminum nitride (AlN). The cylindrical ceramic specimens were confined laterally by shrink fit sleeves: the amount of confining pressure (0-230 MPa) was varied by using different sleeve materials. The quasi-static axial load was applied by a hydraulic driven Material Test System (MTS), whereas the dynamic axial load was provided by a modified split Hopkinson (Kolsky) pressure bar (SHPB). Under both quasi-static and dynamic loading conditions, the experimental results for both materials showed that the failure mode changed from fragmentation by axial splitting under conditions of uniaxial stress (without lateral confinement) to localized deformation on faults under moderate lateral confinement. The fault initiation process was studied experimentally in detail. Based on the experimental results, a compressive brittle failure process was summarized. A transition from brittle to ductile behavior was observed in Macor under high confinement pressure which was achieved using a second sleeve around the inner sleeve. The compressive failure strengths of both materials increased with increasing confinement pressure under both quasi-static and dynamic loading conditions. The highest dynamic compressive stren ths of Macor and AlN measured in the experiments were 1.35 GPa and

5.40 GPa, respectively, whereas their quasi-static compressive strength were measured to be 0.43 GPa and 2.5 GPa, respectively.

Based on the experimental results on AlN together with available data in the literature, a failure/flow criterion was developed for ceramic materials under multiaxial loading. A Mohr-Coulomb criterion and an improved Johnson-Holmquist model were found to fit the experimental data for brittle failure, whereas the materials exhibited pressure insensitive plastic flow at high pressures. Observations made in other types of dynamic experiments (e.g., shock wave loading) were rationalized based on the postulated failure mechanisms and the possibility of plastic flow beyond the Hugoniot elastic limit (HEL). The effect of various material properties on the failure behavior was investigated using the proposed failure criterion. The applicability of the present model to a range of ceramics was also explored and the limitations of the model were outlined.

TABLE OF CONTENTS

Chapter 1

Introduction

1.1 Motivation

Ceramics and ceramic composites are being used increasingly as structural materials in impact related applications. Due to rapid advances in processing technology, high strength ceramics and ceramic composites are being developed with exceptional mechanical properties. Since relatively little is known about the mechanical behavior of ceramic materials in comparison to metallic structural materials, monolithic ceramics and ceramic composites have been at the forefront of advanced materials research. In general, ceramic materials have lower densities. higher compressive strengths, better electrical insulating properties, and better resistance to high temperatures and severe environmental conditions as compared to metals. Ceramics and their composites are used in numerous structural applications such as cutting tools, armor, turbo chargers, gas turbine components and bio-implants (hip ball joint, jaw bone). It has been found that armor consisting of confined ceramic blocks or plates outperforms metallic armor when impacted by long rod projectiles (Klopp *et al.*, 1994). In order to improve the performance of ceramic materials in the impact related applications, it is of significant interest to understand the mechanical behavior of these materials under dynamic loading conditions. The specific objective of this research was to identify the constitutive behavior and failure mode of ceramic materials under multiaxial loading conditions and various loading paths.

The constitutive and failure behavior of some engineering ceramics under quasi-static multiaxial compression has been investigated, e.g., Heard and Cline (1980). Typically, the experiments were conducted using a tri-axial compression technique

commonly used for the study of geological materials in which the material was loaded axially inside a hydraulic pressure chamber. The loading path in such a tri-axial experiment can be varied by independently controlling the axial load and the hydraulic pressure. Under dynamic loading conditions, due to the limitations in the available experimental techniques, experiments were performed under either uniaxial stress or uniaxial strain. Split Hopkinson (Kolsky) pressure bar and its modified versions were the primary tools to dynamically load ceramic specimens in the uniaxial stress state, see Lankford (1977), Ravichandran and Chen (1991) and Nemat-Nasser *et al.* (1991). The ceramic specimens failed in a brittle manner by axial splitting as a result of microcrack propagation and coalescence. The plate impact technique has commonly been used to load specimens under uniaxial strain at very high strain rates, e.g., Raiser et *al.* (1994), Grady (1995). The spall strength (the dynamic tensile strength under uniaxial strain) and Hugoniot elastic limit (HEL, the dynamic compressive elastic limit under uniaxial strain) of ceramic materials are measured using plate impact experiments. Although plate impact experiments have been used widely, the specimen failure mechanisms have not been well characterized due to the difficulty in recovering the tested specimens.

In actual applications, it is clear that impacted materials will experience a combination of uniaxial stress and uniaxial strain loadings. Unfortunately, due to the lack of reliable experimental techniques, little is known about the mechanical behavior of ceramic materials under the stress states between dynamic uniaxial stress and uniaxial strain. Lankford (1994) developed a tri-axial compression technique with an SHPB to characterize the compressive behavior of ceramics and ceramic composites. In these experiments the shear strength of SiC fiber reinforced lithium-alumino-silicate was found to be independent of pressure (P) for P>50 MPa. However, the stress-strain curves and the associated failure modes were not reported. In order to determine the fundamental failure mechanism and the constitutive behavior of ceramic materials, it is necessary to

develop a reliable experimental technique that is capable of (1) dynamically loading the specimen in multiaxial compression; (2) controlling the stress state in the specimen over the range of uniaxial stress to uniaxial strain; (3) allow the recovery of the sample after loaded by a single, well defined pulse for the careful characterization of the failure mode.

This dissertation focuses on both the development of experimental techniques that meet the three requirements mentioned above and the subsequent utilization of these techniques in the investigation of the dynamic compressive behavior of ceramic materials under various multiaxial compressive loading conditions. Based on the experimental results, a failure criterion for ceramics was proposed. The applicability and the limitations of the criterion were also explored.

1.2   Overview

The split Hopkinson (Kolsky) pressure bar (SHPB) was used to dynamically load the specimen in the axial direction for all of the experimental investigations described herein. This technique is well established for the characterization of high strain rate plastic deformation behavior of metals (Follansbee, 1985). Chapter 2 introduces the modifications to the conventional SHPB necessary to investigate the mechanical behavior of brittle materials such as ceramics and to recover the specimen after loading by a well defined, single pulse. The high strain rate failure behavior of a machinable glass ceramic, Macor, was studied under uniaxial stress loading using the modified SHPB.

Macor was chosen for the present investigation because of its low compressive strength (345 MPa under quasi-static loading) but at the same time exhibits the same

physical attributes of a brittle ceramic material. Therefore, a wider range of stress states may be explored within the loading capacity of the experimental facility. Hence, Macor was expected to serve as a model ceramic material for the present investigation. The failure behavior of a monolithic engineering ceramic, aluminum nitride (AIN), was also investigated in order to check the applicability of the results from a model ceramic, Macor, to engineering ceramics.

Since ceramics under investigation are usually harder than the Hopkinson bar material (C-350 maraging steel), the specimen tends to indent the bar end faces during dynamic loading. This indentation not only damages the bar, but also creates local three dimensional stress states near the specimen edges which may cause premature failure of the specimen. Therefore, in addition to the modifications to the SHPB, attention should also be paid to the specimen geometry. In Chapter **3,** various ceramic specimen geometries and insert configurations under investigation were analyzed numerically using an explicit finite element program, DYNA2D. The objective of the analysis was to study the magnitude and locations of stress concentrations in the specimen, the degree to which the hard ceramic indents into the bar, the stress distribution within the specimen, and the effect of specimen size relative to the bar diameter.

Two lateral confinement methods are introduced in Chapter 4. The lateral confinement can be applied by electo-magnetic force or mechanically. Precision timing and shaping of the confinement pulse may be achieved easily using the electro-magnetic method. However, only low confinement pressures can be achieved due to the limitations of the facility. The second approach to apply confinement is a mechanical method in which the confinement pressure is applied by installing a shrink fit metal sleeve on the lateral surface of the cylindrical ceramic specimen. The mechanical approach can provide higher confinement, and it retains the tested specimen for failure mode characterization.

Chapter 5 describes a detailed experimental investigation of the compressive failure behavior of Macor and a sintered aluminum nitride (AlN) using the modified SHPB and the mechanical confinement technique. The results showed that the failure mode of both materials changed from fragmentation by axial splitting under conditions of uniaxial stress to localized deformation under moderate lateral confinement. The initiation sequence of the localization process was illustrated by specially designed experiments. A failure mechanism was presented based on these results together with the corresponding stress-strain behavior.

Based on experimental results, a failure/flow criterion for ceramics is proposed in Chapter 6. In addition, the criterion is corroborated using a micromechanical model. The failure strength data obtained on AlN and Macor in Chapter 5 were found to fit a Mohr-Coulomb failure criterion and an improved Johnson-Holmquist model. Other experimental data from recent literature was also used to extend failure surface into a wider range in the stress space. The effect of various material properties on the failure behavior was investigated based on the failure criterion. The applicability of the present model to various different ceramics was also explored, and the limitations of the model are outlined. Chapter 7 summarizes the current results, and suggestions for future work are presented.

1.3   References

Follansbee, P. S., (1985), "The Hopkinson Bar," in Mechanical Testing, Metals Handbook, **8,** 9th edition, American Society for Metals, Metals Park, Ohio, pp. 198-217.

Grady, D. E., (1995), "Dynamic Properties of Ceramic Materials," Sandia Report SAND94-3266, Sandia National Laboratories, Albuquerque, NM.

Heard, H. C. and Cline, C. F., (1980), "Mechanical Behavior of Polycrystalline BeO, Al_2O_3 and AlN at High Pressure," Journal of Materials Science, 15, pp. 1889-1897.

Klopp, R. W., Shocky, D. A., Seaman, L., Curran, D. R., McGinn, J. T. and de Resseguier, T., (1994), "A Spherical Cavity Expansion Experiment for Characterizing Penetration Resistance of Armor Ceramics," in Mechanical Testing of Ceramics and Ceramic *Composites*, AMD197, ASME, edited by Gilat, A., November, Chicago, Illinois, pp. 41-60.

Lankford, Jr., J., (1977), "Compressive Strength and Microplasticity in Polycrystalline Alumina," Journal of Materials Science, 12, pp. 791-796.

Lankford, Jr., J., (1994) "Utilization of the Split Hopkinson Pressure Bar Under Hydrostatic Confining Pressure to Characterize the Compressive Behavior of Ceramics and Ceramic Composites," in Mechanical Testing of Ceramics and Ceramic *Composites*, AMD197, ASME, edited by Gilat, A., November, Chicago, Illinois, pp. 1-12.

Murrel, S. A. F., (1963), "A Criterion for Brittle Fracture of Rocks and Concrete Under Tri-axial Stress and the Effect of Pore Pressure on the Criterion," in *Rock Mechanics*, edited by Fairhurst, C., Oxford, Pergamon, pp. 563-577.

Nemat-Nasser, S., Isaacs, J. B., and Starrett, J. E., (1991), "Hopkinson Techniques for Dynamic Recovery Experiments," Proc. Roc. *Soc.* London, **A435,** pp. 371-391.

Raiser, G. F., Wise, J. L., Clifton, R. J., Grady, D. E., and Cox, D. E., (1994), "Plate Impact Response of Ceramics and Glasses," Journal of *Applied* Physics, 75 (8), pp. 3862-3869.

Ravichandran, G. and Chen, W., (1991), "Dynamic Failure of Brittle Materials Under Uniaxial Compression," in *Experiments* in *Micromechanics* of Fracture Resistant Materials, AMD 130, edited by Kim, K.-S., pp. 85-90, ASME, New York.

Rosenberg, Z., (1993), "On the Relation Between the Hugoniot Elastic Limit and the Yield Strength of Brittle Materials," Journal of *Applied* Physics, 74, pp. 752-753.

Chapter 2

Dynamic Failure of Macor Under Uniaxial Compression

Abstract

The dynamic failure behavior of a glass ceramic composite, Macor, was investigated under uniaxial compression using a modified split Hopkinson (Kolsky) pressure bar (SHPB). Two necessary modifications of the conventional SHPB are described for testing brittle material as well as the single loading feature to facilitate the characterization of the failure mode. The rise time of the incident pulse was controlled using a pulse shaper to ensure that equilibrium stress state was achieved in the specimen prior to failure. Axial and lateral strain gages mounted directly on the specimen surface provided accurate time resolved strain measurement. This modified technique provides a reliable method for obtaining the deformation and failure characteristics of brittle materials although the strain rates were lower than those achieved in the conventional SHPB experiments. In order to unambiguously characterize the failure mode, the SHPB was designed to load the specimen with a single, well defined stress pulse. Results from the experiments on Macor showed that the failure strength increased as the specimen strain rate was increased from 10^{-7} to approximately 3600 s^{-1}. The dynamic Poisson's ratio remained nearly constant during the loading process until just prior to failure. Scanning electron micrographs of the fracture surfaces indicated that microcrack nucleation and propagation were responsible for the final failure by axial splitting. The fragment size of the tested specimen reduced as strain rate increased.

2.1   Introduction

Brittle materials such as monolithic ceramics and ceramic composites are finding increasing applications with impact loading. In general, ceramics and ceramic composites are very hard and brittle and failure occurs typically at strains of 1-2%. The determination of high strain rate material properties and the understanding of damage evolution in the materials under dynamic loading conditions are important in the analysis of structures made with brittle materials. Thus, reliable experimental techniques are needed to obtain the dynamic properties. However, obtaining reliable mechanical properties of brittle materials at high strain rates poses special challenges in designing and developing experimental techniques. Past investigations have shown that damage, such as microcracking and/or microplasticity, plays an important role in deformation and failure of ceramics and ceramic composites at stress levels even below the Hugoniot elastic limit (HEL) under dynamic loading conditions; see Lankford (1977), Longy and Cagnoux (1989), Raiser *et al.* (1990), and Ramesh and Ravichandran (1990). HEL is the elastic limit of a material under one-dimensional strain compression. **A** high strain rate experimental technique that is used commonly in the characterization of ductile metals is the split Hopkinson pressure bar (also referred to as the Kolsky pressure bar); see Lindholm (1964) and Follansbee (1985). The concept originally developed by Kolsky (1949), has found widespread applications in testing ductile materials at strain rates up to 10^4 s^{-1}. This technique has been directly applied without any modification to brittle ceramics and ceramic composite materials; for example, see Lankford (1977). However, the application of this technique, for testing brittle materials, has serious limitations.

In this chapter, a brief review of the conventional SHPB technique will be followed by a discussion of the limitations in testing hard and brittle materials at high strain rates. The modifications necessary to apply this technique to monolithic ceramics and ceramic composite testing will be introduced, as well as the single loading feature of the SHPB.

Results from a study on the deformation and failure characteristics of a brittle machinable ceramic, Macor, over a wide range of strain rates are presented and discussed.

2.2   Experimental Techniques

2.2.1 Review of the Split Hopkinson (Kolsky) Pressure Bar (SHPB)

The split Hopkinson pressure bar is a well established apparatus for the high strain rate testing of ductile metals. A brief review of the technique will be given below. A schematic illustration of the conventional SHPB is shown in Fig. 2.1. It consists of a striker bar, an incident bar and a transmission bar. **A** specimen of length L is sandwiched between the incident bar and the transmission bar. When the striker bar impacts the incident bar, an elastic compressive stress pulse with a rise time typically about 10 μs propagates along the incident bar: the pulse duration equals the round-trip time of a longitudinal elastic bar wave in the striker bar. When the stress pulse reaches the specimen, part of the pulse is reflected back in the incident bar and the remaining part is transmitted through the specimen into the transmission bar. The strain gages mounted on the bars provide time-resolved measures of the signals in the incident and the transmission bars respectively. Details of this experimental technique can be found elsewhere; see, for example, Lindholm (1964) and Follansbee (1985). One-dimensional calculations by Kolsky (1949) show that the nominal strain rate $\dot{\varepsilon}(t)$ in the specimen can be calculated using the relation

$$\dot{\varepsilon}(t) = -\frac{2c_0}{L}\varepsilon_r(t) \tag{2.1}$$

where L is the original length of the specimen, $\varepsilon_r(t)$ is the time-resolved reflected strain in the incident bar, and c_0 is the longitudinal bar wave velocity in the incident bar which is given by

$$c_0 = \sqrt{\frac{E}{\rho}} \tag{2.2}$$

where E is the Young's modulus and ρ is the mass density of the bar material. An integration of Eqn. (2.1) with respect to time gives the axial strain of the specimen. The nominal axial stress σ in the specimen is determined using the equation

$$\sigma(t) = \frac{A_0}{A_s} E\varepsilon_t(t) \tag{2.3}$$

where A, is the cross-sectional area of the specimen, and $\varepsilon_t(t)$ is the time-resolved strain in the transmission bar of area A_0. All the foregoing calculations are based on the assumption that the specimen undergoes homogeneous deformation. In the derivation of Eqn. (2.1), the incident and transmission bars were assumed to be of the same material and of identical and uniform cross-sectional area.

2.2.2 Limitations of SHPB in Testing Brittle Materials

When brittle materials such as ceramics/ceramic composites are tested in the conventional split Hopkinson pressure bar using the approach presented in the previous section, the limitations of the technique must be recognized if valid experimental results are to be obtained. Several of these limitations are described below.

(1) The split Hopkinson pressure bar was designed to study the high-strain-rate plastic behavior of ductile metals where the mechanical impedance of the specimen is usually much smaller than that of the incident and transmission bars, and therefore, the reflected pulse is usually tensile. The mechanical impedance in the one-dimensional wave propagation problems is defined as $\rho c A$, where ρ is the mass density, c is the bar wave velocity, and A is the area of the cross section perpendicular to the direction of the wave propagation. When the specimen is made of a brittle material, the compressive incident pulse may be reflected as a compressive pulse when $(\rho c A)_{specimen} > (\rho c A)_{bar}$, or as a tensile pulse when $(\rho c A)_{specimen} > (\rho c A)_{bar}$ depending on the mechanical impedance mismatch between the incident bar and the specimen. When the impedance is matched, the incident pulse is transmitted completely through the specimen without any reflection. Even though the specimen diameter is made small enough to ensure a tensile reflected pulse, it is very hard to get an accurate measure of the strain (typically 1-2%) in the specimen, because it is difficult to filter out a short duration signal from the reflected pulse which has been dispersed due to the variation of sound velocity with the wavelength of the excitation (Kolsky, 1963). Therefore, the reflected pulse is not reliable for estimating the strain rate while testing brittle material specimens, and hence the use of Eqn. (2.1) is severely limited.

(2) In characterization of the plastic behavior of metals using a SHPB, step incident pulses are commonly used. A typical incident pulse shape in conventional SHPB is shown by the dotted curve in Fig. 2.2. When such a step pulse is used as the incident pulse for testing of brittle materials, the specimen will either deform elastically to a strain related to the applied stress level by the Young's modulus, or fail by cracking. During the plateau portion of the step loading, the strain will remain constant until unloading occurs if the specimen remains elastic. If the stress is sufficient to cause the nucleation and

propagation of microcracks, the specimen will fail catastrophically and it would not be possible to characterize the corresponding failure mechanism.

(3) If a brittle material is tested in a conventional SHPB and the failure strain ε_f is reached within the rise time of the pulse t_r, the strain rate $\dot{\varepsilon}$ in the specimen during the deformation is on the order of ε_f/t_r. For typical values of strain to failure (1-2 %) and rise times (10μs), the strain rate in the specimen could be as high as 2×10^4 s^{-1}. During the short rise time, it is not possible for the stress to equilibrate within the specimen; see Ravichandran and Subhash (1994). However, equilibrium is an essential condition for properly interpreting the reflected and the transmitted signals in the SHPB using equations (2.1) and (2.3). This is analogous to the problems encountered in obtaining the response of ductile metals at small strains in the conventional SHPB; see Follansbee (1985).

2.2.3 Modifications on the SHPB for Brittle Materials Testing

In the study presented in this chapter, the conventional SHPB has been modified for application to dynamic testing of brittle materials. The modifications involve two changes in the conventional SHPB technique:

(1) utilization of a thin copper disc which is placed at the impact end of the incident bar to increase the rise time of the incident pulse, and

(2) direct measurement of the strain using strain gages attached to the specimen surface.

The presence of the copper disc results in a bell-shaped stress pulse in the incident bar as shown in Fig. 2.2. The shaped stress pulse of Fig. 2.2 is produced by a 100 mm

long maraging steel (VascoMax C-350, hardness Rc=57.8) striker bar with uniform cross-section and a copper (S.A.E. Standard No. 71) disc of 3.3 mm in diameter and 0.85 mm thick at the impact end of the incident bar. The copper disc will be referred to as a pulse shaper later. Shown for comparison in Fig. 2.2 is the stress pulse recorded without a copper disc. While the pulse shaping limits the strain rates at which the experiment can be performed, it does preclude the sudden straining and failure of the specimen, thus alleviating the problems mentioned in the previous section. Furthermore, since the strain is measured directly on the specimen surface as a function of time, reliable information about deformation history can be obtained. Together with the measured transmitted pulse, a complete axial stress (from Eqn.(2.3)) and deformation history of the specimen is produced. This technique has been used successfully to study the deformation and failure modes of ceramics and ceramic composites; see Ramesh and Ravichandran (1990), Ravichandran and Chen (1991), Subhash *et al.* (1993). It should be noted that in this technique, both axial and transverse strains of the specimen can be measured during the test, by suitably orienting strain gages on adjacent faces of prismatic specimens. Other geometries and materials may be used for pulse shaping, for example, Duffy *et al.* (1970) used a pulse shaper in the form a concentric tube to smooth pulses generated by explosive loading in a torsional I-Iopkinson bar. Forrestal *et al.* (1995) used a PMMA disc together with tissue paper to control the rise time and eliminate the oscillations overriding on the incident pulse of a split Hopkinson pressure bar.

The shape and duration of the incident pulse can be tailored by using copper discs of different diameters and thickness and properly designing the geometry of the striker bar as described below. The stress-strain relation of the copper disc is described by the power hardening law

$$\sigma_* = \sigma_0 \varepsilon_*^n \tag{2.4}$$

where σ_* and ε_* are the nominal stress and nominal strain in the disc; σ_0 is the reference stress and n is the strain hardening exponent of the disc material. The pulse propagating through the incident bar, $\varepsilon_i(t)$, can be obtained by solving the following integral relation,

$$\frac{t}{t_0} = \int_0^{\varepsilon_i(t)/\varepsilon_0} \frac{\xi^{(1-n)/n}}{1-\xi} d\xi \qquad \text{for } t < \tau_c \qquad (2.5a)$$

and

$$\varepsilon_i(t) = \varepsilon_i(\tau_c) - \varepsilon_i(t - \tau_c) \qquad \text{for } \tau_c < t < 2\tau_c \qquad (2.5b)$$

where $\xi = \varepsilon_i(t)/\varepsilon_0$; ε_0 is the incident strain in the striker bar, $\tau_c = 2L_s/c_0$ is the round trip time of a longitudinal bar wave in a striker bar of length L_s, and t_0 is a pulse shaping time constant. Note that the duration of the pulse is twice the pulse duration as compared to the conventional Hopkinson bar due to the elastic recovery of the pulse shaper introduced at the interface between the striker bar and the incident bar. A complete analysis of the pulse shaping technique is given in the Appendix A.

The method of mounting strain gages directly on specimen surface has been used before, see, for example, Brace et *al.* (1966) for the purpose of measuring volumetric strains that accompany deformation of rock samples under quasi-static uniaxial compressive loading. In the SHPB experiments on brittle materials, the sample gage technique can be utilized to acquire reliable sample strain history data. This technique enables time resolved profiles of axial strain, Poisson's ratio, and volumetric strain of the specimen to be obtained during the dynamic compression process. It should be recognized that the final readings of the strain gages may not represent the final failure strain of the whole specimen. The strain gage will stop functioning when a crack propagates into the gage area. Above certain stress level, the pre-existing microcracks in the specimen propagate and new microcracks nucleate and then propagate. These

growing microcracks interact with one another and coalesce to form macrocracks which lead to the final failure or fragmentation of the specimen. At any time after the onset of crack propagation, crack(s) may damage the strain gage on the sample surface, leaving the last value as the "apparent" maximum strain. However, the specimen may further deform before its catastrophic failure under dynamic loading. Therefore, close to the final failure point, the strain data (especially the maximum strain reading) from the strain gage reading are not reliable. Also, the compressive strength data should be determined from transmission bar signal instead of from the stress-strain curve where the strain was calculated from the specimen gage signal.

2.2.4 Single Loading History

In the conventional SHPB technique, if the specimen does not fail during the first loading pulse, it may be loaded repeatedly by the compressive pulses reflected from the striker end of the incident bar. The SHPB used in the present investigation has the capability of loading the specimen by a known, single loading pulse. This feature permits the further investigation of failure mode for a given loading history and the relation between the macroscopic behavior and the microstructure in the recovered specimen. The transmission bar used in this study was shorter than the incident bar (Ramesh, 1993) as shown in Fig. 2.3. The transmitted pulse has reflected several times in the shorter transmission bar before the second compressive pulse reflected from the impact end of the incident bar reaches the specimen. Therefore, this simple modification allows the transmission bar to move away from the specimen before the specimen could be loaded by a second compressive pulse from the incident bar, thus providing a single loading pulse in the specimen as being shown on a distance-time (x-t) diagram shown in Fig. 2.4. This feature is demonstrated in Fig. 2.5 by the pulse profiles recorded directly from the strain

gages located at the middle points of the incident and transmission bars and on the specimen. The strain profile directly recorded from the specimen clearly shows that the specimen is loaded by a single pulse. A simplified one-dimensional theoretical analysis of this single loading feature is given in Appendix B. The analysis indicates that the incident bar has to be at least twice as long as the transmission bar to ensure single loading when 50% of the incident pulse in magnitude is transmitted into the transmission bar. However, there are two limitations on the minimum length of the transmission bar: (1) the shortest length that minimizes three-dimensional effect at the specimen/bar interface so that the transmitted wave is essentially one-dimensional at the position of the transmission bar gage, and (2) the transmission bar gage can detect the transmitted signal without any ambiguity.

It can be demonstrated easily that if the second compressive pulse cannot load the specimen, none of the subsequent reflected pulses can either. If the majority of the incident pulse is transmitted through the specimen, as often is observed in ceramic testing, say, $\sigma_T = 0.8\sigma_I$, $\sigma_R = -0.2\sigma_I$, then, in order to achieve the single loading feature, the incident bar is required to be two striker bar lengths longer than the transmission bar when a pulse shaper is used and one striker bar length longer without the pulse shaper. σ_I, σ_R and σ_T are the maximum amplitudes of the incident, the reflected and the transmitted stress pulses, respectively. If the compressive strength of the specimen is very low, transmitted pulse will be very small compared to the incident pulse. In this case, to achieve the single loading feature, the transmission bar may be made of a material with lower mechanical impedance and smaller diameter as compared to the incident bar. It should be noted that Eqn. (2.1) becomes invalid after the modification, and the new transmission bar properties should be used in Eqn. (2.3). The axial strain in the specimen must be measured by methods other than the reflected signal in the incident bar, for example, by the strain gages mounted directly on the specimen. Alternative single pulse loading technique involving

complete momentum trapping features in the incident bar has been proposed by Nemat-Nasser *et al.* (1991). This momentum trapping feature requires complete modifications of the incident bar end. Also, when the specimen strength is very high as will be shown by the results on aluminum nitride in Chapter 5, the momentum trapping device is easily damaged by the high stress level of the pulses in the incident bar.

2.2.5 Experimental Facility

The experiments were conducted in a split Hopkinson pressure bar facility in the Graduate Aeronautical Laboratories at Caltech. The SHPB consists of a striker bar, an incident bar, a transmission bar and a light gas gun for propelling the striker bar. The dimensions of the bars used in this research are 100, 1220 and 580 mm in length for the striker, incident and transmission bars respectively, with a common diameter of 12.7 mm. All the bars are made of high strength VascoMax C-350 maraging steel (Rc=57.8). The uniaxial compressive yield strength of the bars is approximately 2.7 GPa. In order to control the duration of the incident pulse, a series of striker bars of the same material with various lengths ranging from 12.5 to 200 mm were used.

The pulse shaper placed at the impact end of the incident bar was a thin, half hardened copper disc of 3.3 mm in diameter and 0.85 mm in thickness. The size of the copper disc may be varied to control the pulse shape. Each strain gage of the bar and specimen gages forms part of a Wheatstone bridge, and the output signals from the bridges are recorded and processed using a 4 channel Nicolet 440 digital oscilloscope. The specimen strain gages used in this study were WK-06-062AP-350 manufactured by Measurements Group, Inc., Raleigh, NC, with nominal resistance of 350 Ω. The excitation voltage to the Wheatstone bridge was 10 volts. The strain gages attached on

the bar surface were WK-06-250BF-10C from the same manufacturer with nominal resistance of 1000 Ω. The excitation voltage to the Wheatstone bridges for the bar gages was 30 volts provided by a DC power supplier (Model LQD-425, Lambda Electronics, Melville, L.I., N.Y.). No pre-amplifiers were used to amplify the strain gage signals for the digital oscilloscope.

2.3 Experimental Results

2.3.1 Material

The material currently under investigation is a commercially available machinable glass ceramic composite commonly known as Macor; see Grossman (1978) and Corning (1992). Macor is a white, ceramic composite comprised of a fluorophlogopite mica phase (55%) interspersed in a borosilicate glass matrix (45%). The approximate composition of the material as provided by the manufacturer (Corning, 1992) is as follows:

Compounds	Weight %
Silica, SiO_2	46
Alumina, Al_2O_3	16
Magnesia, MgO	17
Potash, K_2O	10
Boron Oxide, B_2O_3	7
Fluorine, F	4

Some of the relevant physical properties of Macor (Corning, 1992) are listed in Table 2.1. The machinability of the ceramic composite is attributed to the growth of

microcracks and their subsequent arrest. The specimens were cut into cubes of 9.5 mm on a side, with the faces lapped to be flat and parallel to within 0.01 mm.

Table 2.1. Physical Properties of the Glass Ceramic Composite, Macor

Density, ρ	2520 kg/m^3
Young's Modulus, E	64.1 GPa
Shear Modulus, G	25.4 GPa
Poisson's Ratio, v	0.26
Quasi-Static Compressive Strength	345 MPa

Macor was chosen for the present investigation because of its low compressive strength (345 MPa under quasi-static loading) but at the same time exhibits the same physical attributes of a brittle ceramic material. Hence, Macor was expected to serve as a model ceramic material for the present investigation.

2.3.2 SHPB Results

The typical strain signals from the incident and transmission bars are shown in Fig. 2.6. Each of the transmitted signals exhibit a maximum value corresponding to the maximum stress in the specimen. This maximum stress will be referred to as the failure strength at the corresponding strain rate. The axial and transverse strains are measured directly on the specimen by the strain gages mounted on the specimen surfaces, and the corresponding Wheatstone bridge output signals are shown in Fig. 2.7. These two strain profiles provide the time-resolved strain and Poisson's ratio information in the specimen.

The experiments were conducted in the split Hopkinson bar facility at strain rates ranging from approximately 200-3600 s^{-1}, where the strain rate was determined from the average slope of the rising portion in the strain profile recorded by the axial specimen strain gage; a typical strain profile is shown as the axial signal in Fig. 2.7. The strain rates in the specimen were varied by altering the rise time characteristics of the loading pulse. Figure 2.8 shows a typical stress strain curve for an experiment at a strain rate of 245 s^{-1}. The stress-strain curve shows that the stress-strain relation is linear from the onset of loading up to a stress of approximately 60% of the failure strength. As the loading level continues to increase, the tangent modulus decreases gradually until the loading level exceeds 95% of the failure strength where the tangent modulus is close to zero. When the maximum stress is reached in the specimen, the tangent modulus becomes zero. In one experiment, the specimen was loaded to 94% of its failure strength and then unloaded. The same specimen was loaded again and failed at its compressive strength as if it were not previously loaded. The gradual degradation of the tangent modulus may indicate that nucleation and propagation of microcracks begins at approximately 60% of the failure strength. However, this gradual degradation of the tangent modulus does not affect the failure strength of the material until the stress level is very close to catastrophic failure of the specimen. Massive propagation and interaction of microcracks are considered to occur as indicated by the very low value of the tangent modulus near failure. Little inelastic deformation was observed in the uniaxial stress experiments on Macor. In each of the experiments from which the failure strength was obtained, the specimen was fragmented by axial splitting. The fragment size was observed to reduce as the strain rate was increased, indicating that the number of the cracks propagating simultaneously increases with strain rate.

The failure strengths were calculated from the maximum values of the transmitted signals from dynamic experiments, and from the maximum values of the load cell readings

from quasi-static experiments conducted using a hydraulically driven Material Test System. Figure 2.9 shows the variation of the failure strength of Macor with respect to strain rate on a logarithmic scale. Inspection of Fig. 2.9 indicates that the compressive failure strength increases slowly as the strain rate is increased in the quasi-static range ($\dot{\varepsilon} < 1\,\text{s}^{-1}$), whereas the failure strength increases rapidly with the increase of the strain rate after the strain rate enters the dynamic range where the experiments were performed on the modified SHPB ($\dot{\varepsilon} = 200 - 3600\,\text{s}^{-1}$). The relation between the compressive strength and the logarithmic strain rate can be approximately represented by two straight lines with the intersection at $\dot{\varepsilon} = 100\,\text{s}^{-1}$. The rate sensitivity exponent of the failure strength ($\partial\sigma_{F}\,I\,\partial\ln\dot{\varepsilon}$) for Macor in the low and high strain rate regions were determined to be 0.0078 and 0.132, respectively. The rate sensitivity of Macor can be attributed to the kinetics of damage accumulation such as microcracking. The issues associated with rate sensitivity of ceramics have been recently presented by Ravichandran and Subhash (1995). The maximum failure strength of Macor obtained in the experiments is 0.82 GPa at a strain rate of 3600 s^{-1}.

Figure 2.10 is a plot of typical variation of the transverse strain of the specimen as a function of the axial strain measured with the axial and transverse specimen gages of the type shown in Fig. 2.7. The slope at a point on the curve is the Poisson's ratio of the material at the corresponding axial strain. The average value of Poison's ratio before failure was measured to be 0.21. Figure 2.10 shows that the Poisson's ratio remains relatively constant until very close to catastrophic failure when massive microcrack nucleation and growth take place. The apparent increase in the Poisson's ratio during failure can be attributed to microcrack nucleation and growth causing abrupt expansion in the lateral direction.

2.3.3 Microscopic Observation of Damage

The fracture surfaces from the failed specimens were examined in a scanning electron microscope (SEM) to identify the micromechanisms of damage. These fracture surfaces are the results of macroscopic axial cracks propagating through the specimen at the later stages of deformation. Two of the micrographs are shown in Fig. 2.11 (a) and (b) at different magnifications. The dominant mechanism of damage appears to be microcracking.. Microcracking appears predominantly at the interface between glassy and crystalline phases and at triple grain boundary junctions. Also, the microcracks appear to be randomly oriented in the plane of the micrograph and are evenly distributed as shown in Fig. 2.11 (a). The cracks which appear in the micrographs are intersections of three-dimensional flaws that intersect with the fracture surface. The average grain size is observed to be 8 pm, and the average size of microcracks is approximately 6 pm.

2.4 Conclusions

The conventional split Hopkinson bar has been modified to determine reliably the deformation and failure characteristics of brittle materials. The modified technique also has the capability of recovering the tested specimen after loading with a single, well defined pulse. Model experiments have been performed on a machinable glass ceramic composite, Macor. The compressive failure strength of Macor increases as strain rate is increased. The rate of the increase in strength as a function of strain rate depends on the strain value. The rate of strength increase with respect to strain rate is low in the quasi-static range as compared to the dynamic region at strain rates greater than 200 s⁻¹. The strain rate sensitivity exponents of the failure strength under quasi-static and dynamic loading conditions are 0.0078 and 0.13, respectively. The Poisson's ratio remains nearly

constant in the dynamic loading process until very close to failure. The average value of Poisson's ratio was measured to be 0.21. The average size of the tested specimen fragments reduces as the dynamic strain rate is increased. This is consistent with the fragmentation model proposed by Grady and Kipp (1985). From microscopic observations, microcracking under macroscopic compression appears to be the dominant micromechanism of damage and failure of the glass ceramic under study. The microcracks begin to nucleate and propagate when the stress level reaches 60% of the failure strength as indicated by the stress-strain curve. Massive microcrack nucleation and propagation take place only when very close to the macroscopic catastrophic failure of the specimen.

2.5 **References**

Brace, W F., Paulding, Jr , B W and Scholz, C , (1966), "Dilatancy in the Fracture of Crystalline Rocks," *Journal of Geophysical Research*, 71, (16), pp 3939-3953

Corning Incorporated, (1992), "Macor Machinable Glass Ceramic: Safty and Health Issues," Technical Bulletin, Macor-03, Corning, New York.

Courant, R. and Hilbert, D., (1962), "Methods of Mathematical Physics," Vol. II, Inter Science, New York.

Duffy, J., Cambell, J. D. and Hawley, R. H., (1971), "On the Use of Torsional Hopkinson Bar to Study Rate Effects in 1100-0 Aluminum," *Journal of Applied Mechanics*, **38,** pp. 83-91.

Follansbee, P. S., (1985), "The Hopkinson Bar," in *Mechanical Testing, Metals Handbook*, **8,** 9th edition, American Society for Metals, Metals Park, Ohio, pp. 198-217.

Forrestal, M. J., (1995), Private Communication

Grady, D E and Kipp, M E, (1985), "Geometric Statistics and Dynamic Fragmentation," *Journal of Applied Physics*, 58, pp 1210-1222

Grossman, D., G., (1978), "Machining a Machinable Glass Ceramic," *American Machinist.*

Kolsky, H., (1949), "An Investigation of the Mechanical Properties of Materials at Very High Rates of Loading," *Proc. Roy. Soc. London,* B62, pp. 676-700.

Kolsky, H., (1963), "Stress Wave in Solids," Dover Publications, New York

Lankford, J., (1977), "Compressive Strength and Microplasticity in Polycrystalline Alumina," *Journal of Materials Science, 12,* pp. 791-796.

Lindholm, U. S., (1964), "Some Experiments with the Split Hopkinson Pressure Bar," *Journal of Mechanics and Physics of Solids,* **12,** pp. 317-335.

Longy, F. and Cagnoux, J., (1989), "Plasticity and Microcracking in Shock Loaded Alumina," *Journal of the American Ceramic Society,* 72, pp. 971-979.

Nemat-Nasser, S., Isaacs, J. B. and Starrett, J. E., (1991), "Hopkinson Techniques for Dynamic Recovery Experiments," *Proc. R. Soc. Lond.* **A435,** pp. 371-391.

Raiser, G. F., Clifton, R. J. and Ortiz, M., (1990), "A Soft Plate Impact Recovery Experiment for Studying Microcracking in Ceramics," *Mechanics of Materials, 10,* pp. 43-58.

Ramesh, K. T. and Ravichandran, G., (1990), "Dynamic Behavior of a Boron Carbide-Aluminum Cermet: Experiments and Observations," *Mechanics of Materials, 10,* pp. 19-29

Ramesh, K. T., (1993), Private Communication

Ravichandran, G. and Chen, W., (1991), "Dynamic Failure of Brittle Materials Under Uniaxial Compression," in *Experiments in Micromechanics of Fracture Resistant Materials,* AMD130, ASME WAM, Atlanta 1-6 December 1991, edited by Kim, K.-S., pp. 85-90.

Ravichandran, G. and Subhash, G., (1994), "Critical Appraisal of Limiting Strain Rates for Compression Testing of Ceramics in a Split Hopkinson Pressure Bar," *Journal of the American Ceramic Society,* 77(1), pp. 263-267.

Ravichandran, G. and Subhash, G., (1995), "A Micromechanical Model for High Strain Rate Behavior of Ceramics," *International Journal of Solids and Structures,* in press.

Subhash, G. and Nemat-Nasser, S., (1993), "Uniaxial Stress Behavior of Y-TZP," *Journal of Materials Science,* **28,** pp. 5949-5952.

Appendix A

An analysis of the pulse shaping technique (equations (2.5a) and (2.5b)) is given below to aid in the design of high strain rate testing of brittle materials using the modified split Hopkinson pressure bar. The analysis is based on one-dimensional wave propagation, and the solution is obtained using the method of characteristics (Courant and Hilbert, 1962). The governing equations for waves propagating in a one-dimensional bar can be written from the equations of motion and compatibility (strain-velocity) as follows,

$$\frac{\partial \sigma}{\partial x} = \rho \frac{\partial v}{\partial t} \tag{2A.1}$$

$$\frac{\partial v}{\partial x} = \frac{\partial \varepsilon}{\partial t} \tag{2A.2}$$

where σ is the nominal stress, ε is the corresponding nominal strain, and v is the particle velocity. x and t are the spatial and time variables.

The incident and striker bars are assumed to be made of the same material and constant cross-sectional area A_0. They are also assumed to be linearly elastic governed by Hooke's law given below,

$$\sigma = E\varepsilon \tag{2A.3}$$

where E is the Young's modulus of the bar material. A thin disc of thickness h and cross-sectional area A is placed between the striker bar and the incident bar of the SHPB. The disc (pulse shaper) material is assumed to be power hardening and rate independent, whose stress-strain relation is given by.

$$\sigma_* = \sigma_0 \varepsilon_*^n \tag{2A.4}$$

where σ_* and ε_* are the nominal stress and nominal strain in the pulse shaper; σ_0 is the reference stress and n is the strain hardening exponent of the disc material.

The time t=O corresponds to the instant of impact of the striker bar on the pulse shaper. Upon impact, compressive pulses propagate both in the incident bar and the striker bar. If one assumes the disc undergoes homogeneous deformation upon impact, using Eqn. (2.1), the strain rate in the pulse shaper can be written as,

$$\dot{\varepsilon}_* = -\frac{2c_0}{h} \varepsilon_s \tag{2A.5}$$

where ε_s is the reflected strain in the striker bar which can be written in terms of the incident strain in the striker bar, ε_0 and the strain in the incident bar, ε_i,

$$\varepsilon_0 = \varepsilon_i + \varepsilon_s \tag{2A.6}$$

The incident strain in the striker bar, ε_0, can be determined from the impact velocity of the striker bar V, through the relation,

$$V_0 = -2c_0 \varepsilon_0. \tag{2A.7}$$

Assuming that the stresses are equilibrated across the deforming pulse shaper, the stresses in the pulse shaper and in the incident bar, σ_* and σ_i, can be related using Eqn. (2.2), knowing that $\sigma_i = E\varepsilon_i$,

$$\sigma_* = \frac{A_0}{A} E \varepsilon_i \tag{2A.8}$$

One can rewrite Eqn. (2A.6) in terms of ε_i by eliminating ε_* and ε_s using equations (2A.4), (2A.5), (2A.7), and (2A.8) as

$$t_0 \xi^m \frac{d\xi}{dt} = 1 - \xi \tag{2A.9}$$

where $\xi = (\varepsilon_i / \varepsilon_0)$ and m=(1-n)/n; t_0 is a pulse shaping time constant which is a function of the material properties and the geometry of the bars and the pulse shaper, and the amplitude of the input loading,

$$t_0 = \frac{1}{n} \left(\varepsilon_0 \frac{EA_0}{\sigma_0 A} \right)^{\frac{1}{n}} \left(\frac{h}{V_0} \right). \tag{2A.10}$$

Using separation of variables and integrating (2A.9), one obtains the following integral relation for the compressive pulse propagating through the incident bar, $\varepsilon_i(t)$,

$$\frac{t}{t_0} = \int_0^{\varepsilon_i(t)/\varepsilon_0} \frac{\xi^m}{1-\xi} d\xi \qquad \text{for } t < \tau_c \tag{2A.11}$$

where $\tau_c = (2L/c_0)$ is the round trip time of a longitudinal bar wave in a striker bar of length L. The pulse propagating through the striker bar $\varepsilon_s(t)$ can be obtained by using (2A.6) and (2A.11),

$$\varepsilon_s(t) = \varepsilon_0 - \varepsilon_i(t) \qquad\qquad \text{for } t<\tau_c. \qquad\qquad (2A.12)$$

At time $t=\tau_c$, the pulse propagating in the striker bar reaches the disc/striker bar interface as a tensile pulse and begins unloading   This information is propagated as the unloading part of the incident pulse, ε_i,

$$\varepsilon_i(t) = \varepsilon_i(\tau_c) - \varepsilon_i(t - \tau_c) \qquad\qquad \text{for } \tau_c<t<2\tau_c. \qquad\qquad (2A.13)$$

Note that the duration of the incident pulse $(2\tau_c)$ is twice the pulse duration in the conventional Hopkinson bar.

For arbitrary values of n, one can solve (2A.11) using numerical quadrature. However, for some specific values of n, such as n=1/2 or 1, one can obtain a closed form solution for the pulse in the incident bar, $\varepsilon_i(t)$. For an elastic disc, n=1, one can explicitly write the incident pulse using **(2A.**11) and (2A.13):

$$\frac{\varepsilon_i(t)}{\varepsilon_0} = 1 - \exp\left(-\frac{t}{t_0}\right) \qquad\qquad \text{for } t<\tau_c \qquad\qquad (2A.14a)$$

$$\frac{\varepsilon_i(t)}{\varepsilon_0} = \exp\left(-\frac{t-\tau_c}{t_0}\right) - \exp\left(-\frac{\tau_c}{t_0}\right) \quad \text{for } \tau_c<t<2\tau_c. \qquad (2A.14b)$$

The expressions (2A.14a) and (2A.14b) indicate that the shape of the pulse is strongly governed by the pulse shaping time constant, t_0. By choosing proper pulse shaper material (o, and n), geometry (h and A_0/A), and impact velocity (V, and hence ε_0), one can produce a pulse of desired shape and duration. It is clearly seen from Eqn. (2A.10) that in

the absence of a pulse shaper, $t_0=0$, and one recovers the one-dimensional result, $\varepsilon_i(t)/\varepsilon_0=1$ for $t<\tau_c$ and $\varepsilon_i(t)/\varepsilon_0=0$ for $t>\tau_c$, indicating a step pulse from the longitudinal impact between the two bars. Equations (2A.11) and (2A.13) provide a simple methodology to shape pulses for the Hopkinson bar experiments.

In this simple analysis, the effects of friction, radial inertia, and strain rate on the pulse shaper have been neglected. The stress-strain relation (2A.4) for the pulse shaper material should not be viewed as a one-dimensional constitutive description for the material, but rather as an effective stress-effective strain model which include the radial inertial and frictional constraints on the pulse shaper.

Appendix B

From one-dimensional elastic wave propagation theory (I-D stress), the displacement u at a point in the loading direction is related to the nominal stress σ at that point by

$$\frac{\partial u}{\partial t} = \frac{\sigma}{\rho c_0} \qquad (2B.1)$$

where ρ and c, are the mass density and the longitudinal bar wave velocity of the media in which the wave is propagating. If σ is a constant amplitude stress pulse with duration of At, the above equation can be rewritten as

$$\Delta u = \frac{\sigma}{\rho c_0} \Delta t \qquad (2B.2)$$

where Au is the displacement of the material point after the passage of the stress pulse.

After loading the specimen, the first (1) compressive pulse moved the incident bar end which is in contact with the specimen by a distance which is determined by

$$(\Delta u_1)_1 = \frac{\Delta t}{\rho c_0} (\sigma_1 - \sigma_R) \qquad (2B.3)$$

where σ_I and σ_R are the amplitudes of the incident and reflected stress pulses in the incident bar, respectively. σ_I and σ_R usually have opposite signs in SHPB experiments, i.e., the reflected pulse is usually tensile if the incident pulse is compressive. Therefore, A u_1 is actually the result of the linear addition of the contributions from $\left| \sigma_1 \right|$ and $\left| \sigma_R \right|$. The

reflected pulse σ_R will travel down the bar and reflect back again from the impact end of the incident bar as a compressive pulse. If the transmission bar did not move away from the specimen, this pulse would load the specimen for a second time. When this second compressive pulse reaches the specimen end of the incident bar, the incident bar end will move without any resistance if the transmission bar has already moved away. Therefore, the second (2) compressive pulse in the incident bar would move the specimen end of the incident by a distance

$$(\Delta u_I)_2 = \frac{\Delta t}{\rho c_0}(-2\sigma_R) \tag{2B.4}$$

Thus, if the pulse duration is assumed to be much shorter than the time for the bar wave to travel through the incident bar, then at time $t = 2\frac{L_1}{c_0} + 2\Delta t \approx 2\frac{L_1}{c_0}$, where L, is the incident bar length, the incident bar-specimen interface has moved by a distance of

$$\Delta u_I = \frac{\Delta t}{\rho c_0}(\sigma_I - 3\sigma_R). \tag{2B.5}$$

To prevent the specimen from being loaded repeatedly, at time $t = 2\frac{L_1}{c_0}$, the transmission bar-specimen interface must have moved a distance larger than Δu_I in (2B.5). The distance the transmission bar end has moved at $t = 2\frac{L_1}{c_0}$ will be determined below using a similar analysis. Each reflection of the transmitted pulse in the transmission bar moves the bar farther away from the specimen. After the first transmission pulse and N reflections, the specimen end of the transmission bar has moved by

$$\Delta u_T = (N+1)\frac{\Delta t}{\rho c_0}\sigma_T. \tag{2B.6}$$

If $\Delta u_T > Au_I$, then the specimen will not be loaded for the second time. The inequality can also be expressed as follows by using (2B.5) and (2B.6)

$$(N+1)\frac{\Delta t}{\rho c_0}\sigma_T > \frac{\Delta t}{\rho c_0}(\sigma_I - 3\sigma_R). \tag{2B.7}$$

If λ is defined as the fraction of the incident pulse transmitted, then $\sigma_T = \lambda\sigma_I$, and $\sigma_R = -(1-\lambda)\sigma_I$. When combined with (2B.7), the resulting expression is

$$(N+1)\lambda\sigma_I > (4-3\lambda)\sigma_I$$

or $\qquad N > \dfrac{4}{\lambda} - 4.$ $\hfill (2B.8)$

In the case where the magnitudes of the reflected and transmitted pulses are the same, i.e., $\sigma_T = 0.5\sigma_I$, $\sigma_R = -0.5\sigma_I$, or, $\lambda=0.5$, then,

$$N > 4 \tag{2B.9}$$

which implies that the transmitted pulse must be reflected at least four times in the transmission bar prior to the arrival of the second compressive pulse at the specimen to avoid loading the specimen a second time. This condition requires that the incident bar has to be at least twice as long as the transmission bar to ensure single loading.
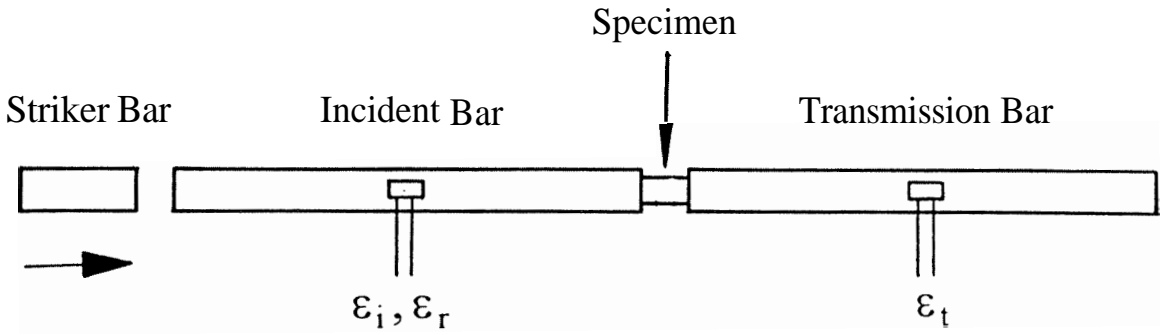
Figure 2.1   A schematic illustration of conventional split Hopkinson pressure bar.
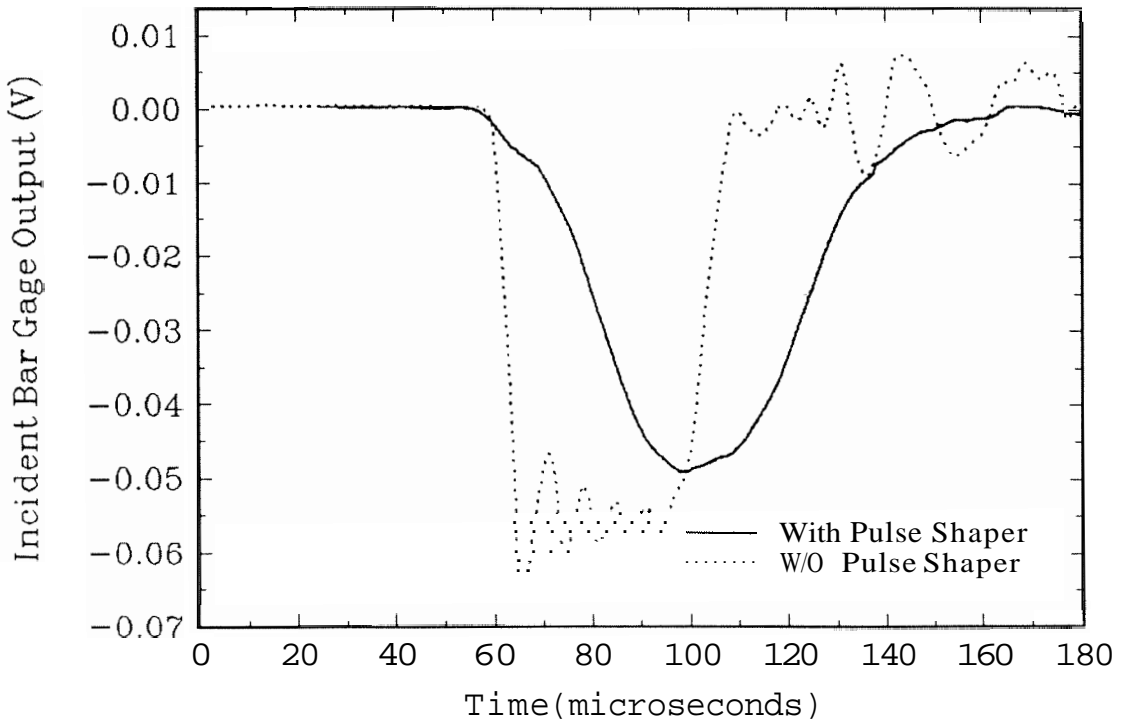
Figure 2.2   The incident pulses with and without a pulse shaper.
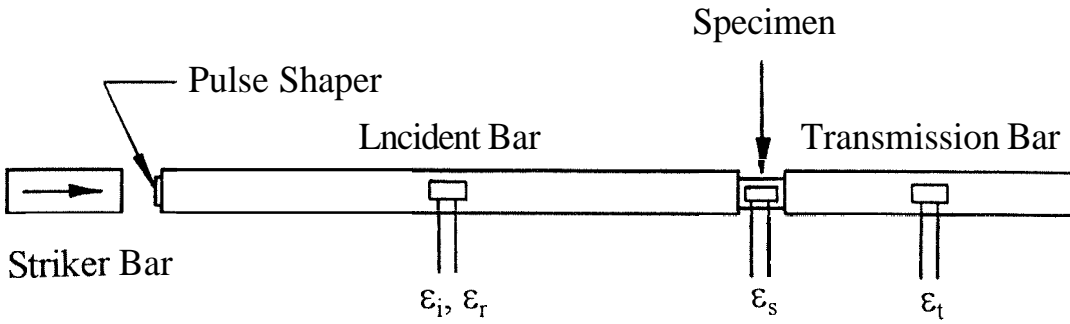
Figure 2.3　A schematic illustration of the modified SHPB.
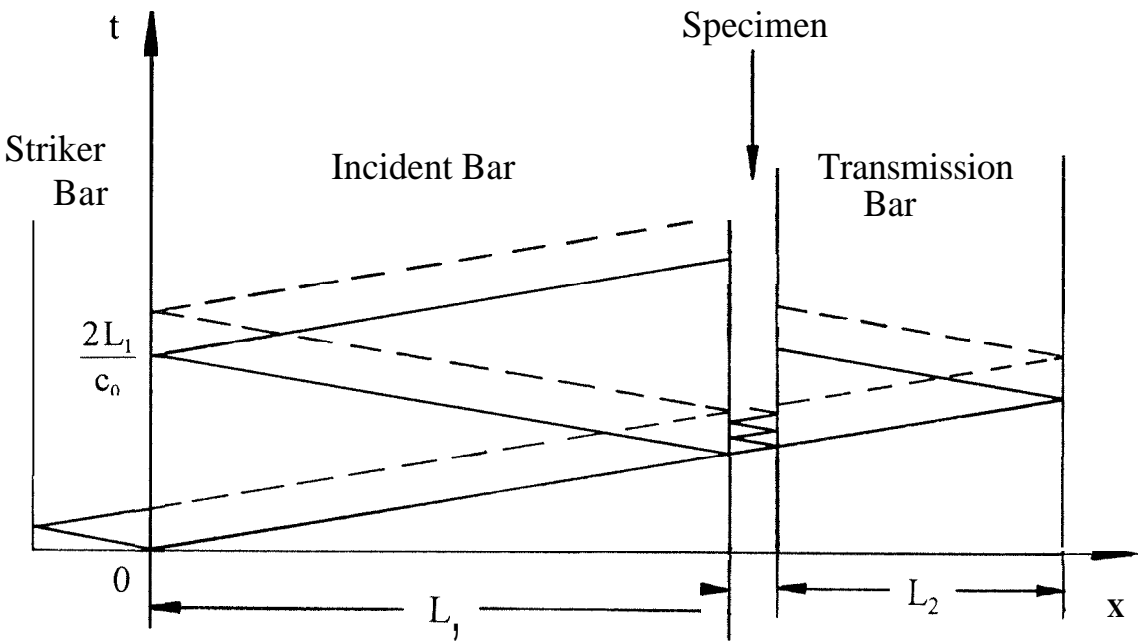
Figure 2.4　Distance-time (x-t) diagram illustrating single loading feature.
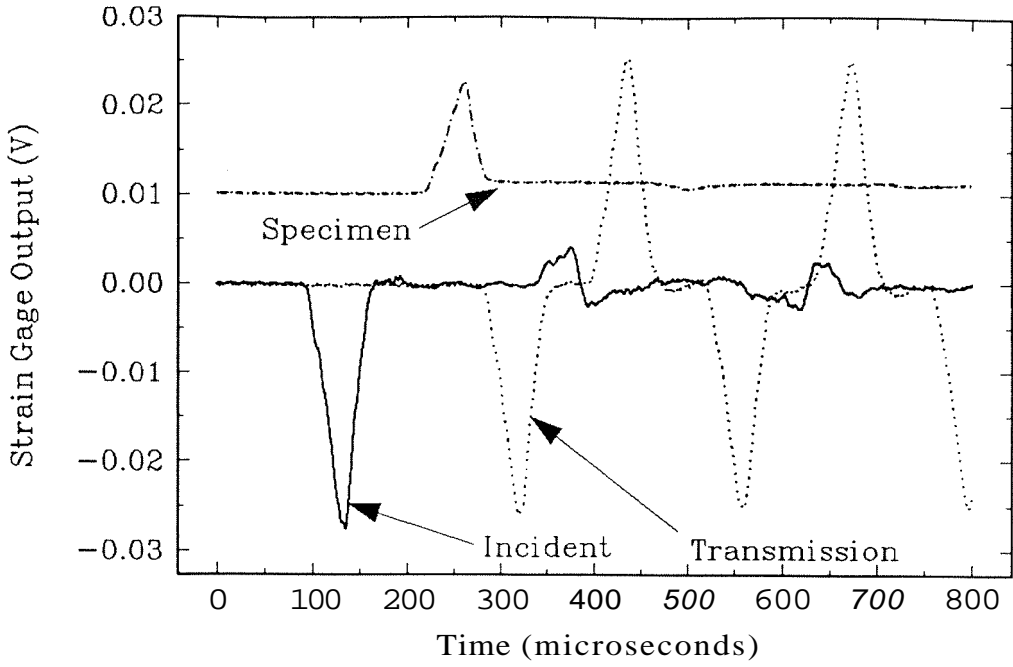
Figure 2.5   Strain gage signals from incident bar, transmission bar and specimen illustrating single loading feature of the modified SHPB.
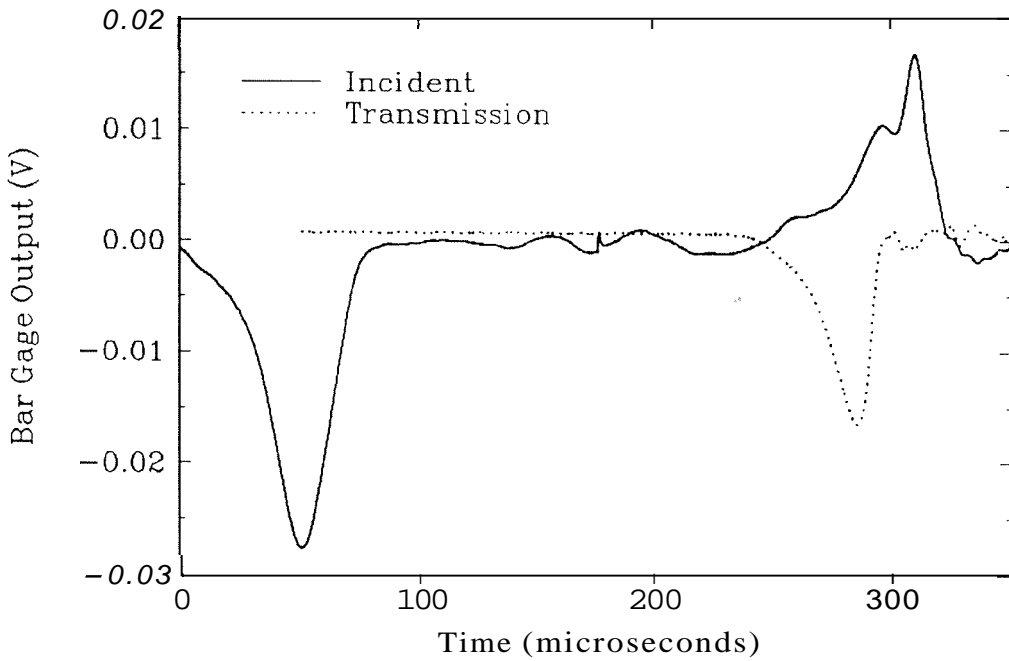
Figure 2.6   Typical incident and transmission bar strain gage signals in an experiment.
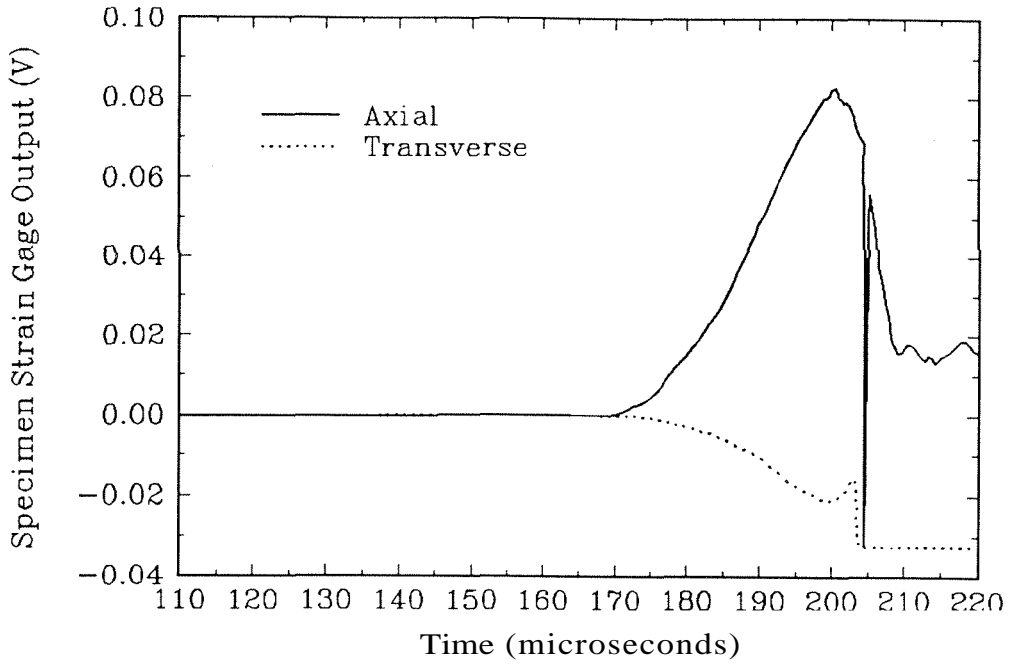
Figure 2.7   Axial and lateral specimen strain gage signals from a typical experiment.
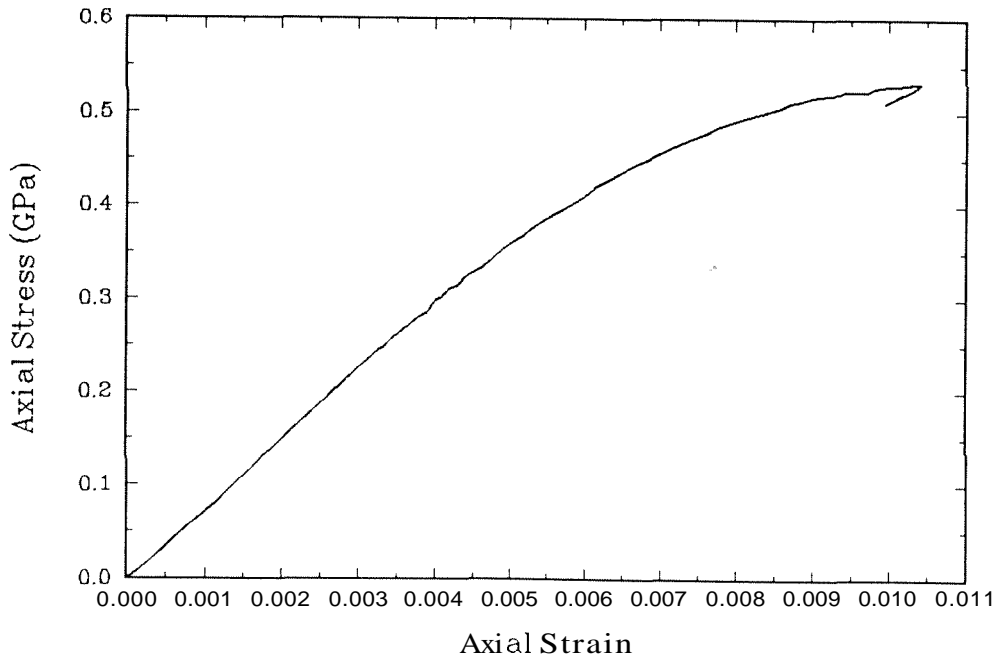
Figure 2.8   Stress-strain curve of Macor under dynamic uniaxial compression at a strain rate of 280 s^{-1}.
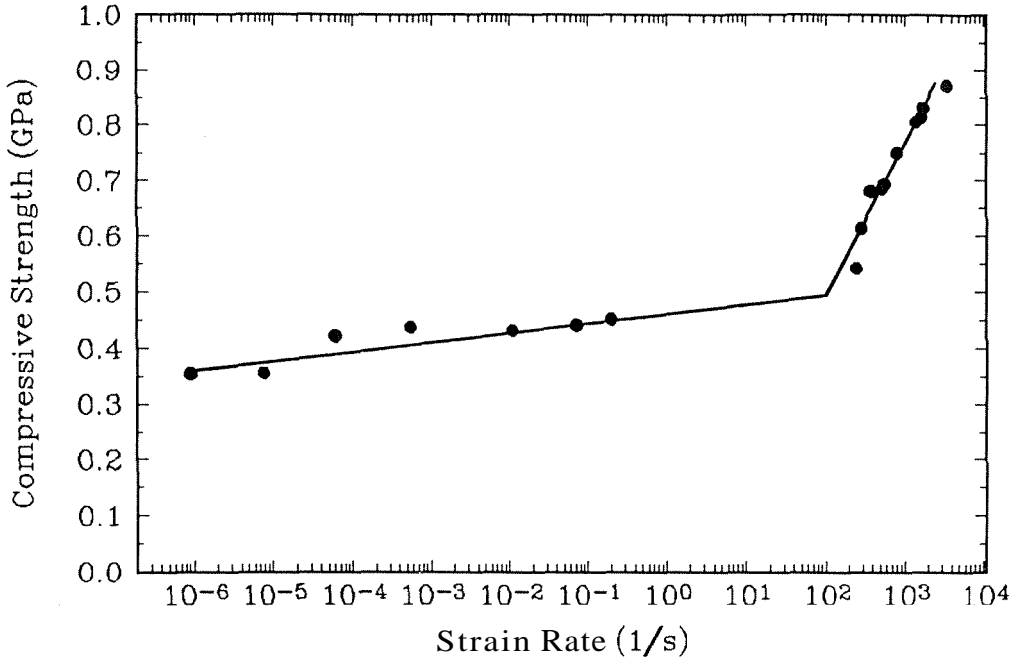
Figure 2.9   Variation of compressive failure strength of Macor with strain rate.
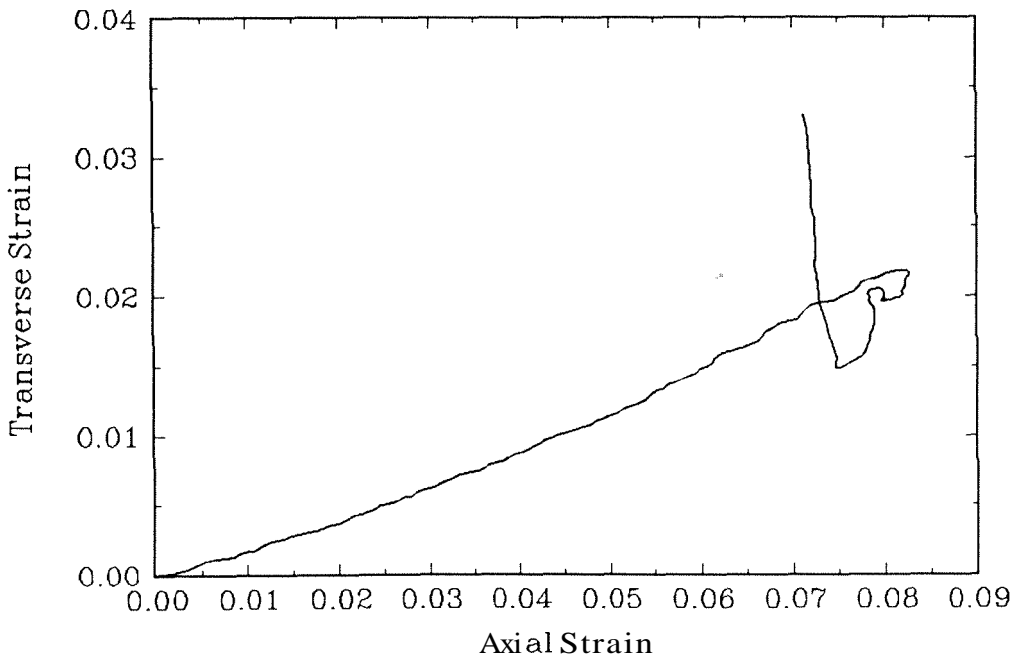
Figure 2.10   Variation of lateral strain with axial strain--the slope is the Poisson's

ratio.
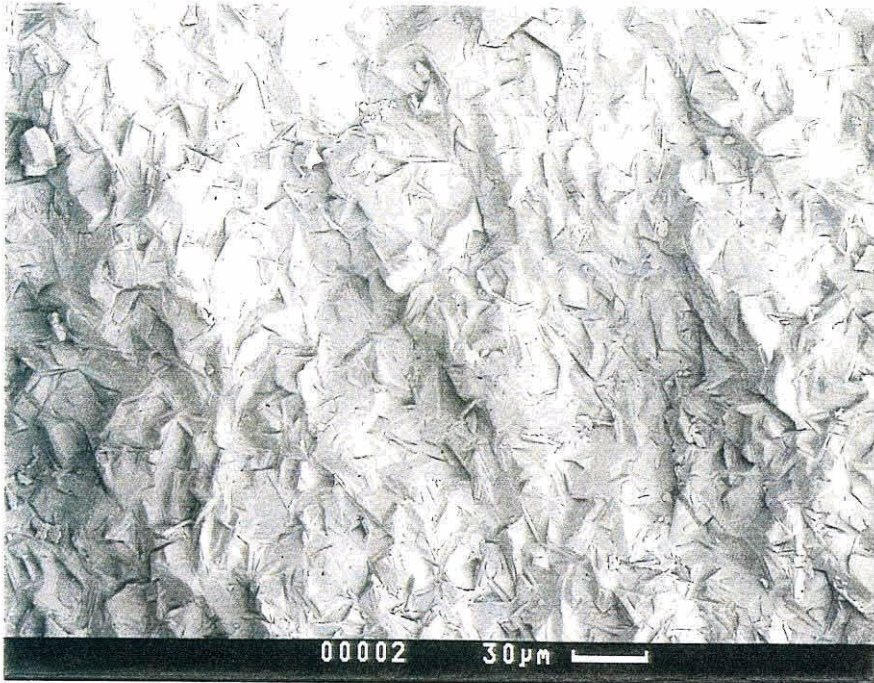
(a)

(b)

Figure 2.11   SEM micrographs of the failure surface.

Chapter 3

Evaluation of Ceramic Specimen Geometries Used In Split Hopkinson Pressure Bar

Abstract

Various ceramic specimen geometry and insert configurations being used for dynamic compression testing in a split Hopkinson pressure bar were analyzed numerically using DYNA2D. The objective of the analysis was to study the magnitude and locations of stress concentrations in the specimen, the degree to which the hard ceramic specimen indents into the bar, the stress distribution within the specimen, and the effect of specimen size relative to the bar diameter. It is demonstrated that a dog-bone shaped specimen with the end diameter matching the bar diameter is the ideal geometry which yields a uniform stress distribution within the gage length of the specimen. A cylindrical specimen with impedance matched tungsten carbide inserts is also found to be a sound combination for obtaining reliable experimental data on the failure strength of ceramics. A cylindrical specimen tested with diameter matched conical alumina inserts performs equally well but has the disadvantage of additional machining costs associated with fabricating conical ceramic inserts

3.1   Introduction

The dynamic compressive failure strength is an important mechanical property that determines the suitability of ceramics and ceramic composites in various structural applications subjected to impact. Due to rapid advances in processing technology, high strength ceramics and ceramic composites are being developed with exceptional mechanical properties. Determination of the failure strength of these high strength ceramics at high strain rates poses special challenges in designing and developing new experimental techniques. An experimental technique that is commonly used in the characterization of ductile metals at high strain rates is the split Hopkinson pressure bar (SHPB), also referred to as the Kolsky pressure bar, see Lindholm (1964), Follansbee (1985). Originally developed by Kolsky (1949), the concept has found widespread applications in testing ductile materials at high strain rates in the range of 10^2 to 10^4s^{-1}.

In general, ceramics and ceramic composites are very hard and brittle materials: they fail typically at strains of 1-2%. In order to obtain reliable and consistent experimental data when testing these materials with the SHPB, appropriate modifications must be incorporated in both the experimental technique and in the design of specimen geometry. Many modifications to the SHPB technique and the specimen design have been proposed in the recent literature. For example, shaping of the loading pulse has been used to prevent the ceramic specimen from failing before equilibrium is attained. Reliable strain data has been obtained during testing by mounting strain gages on the ceramic specimen surface, see Blumenthal *et al.* (1990), Ravichandran and Chen (1991), Nemat-Nasser *et al.* (1991), Blumenthal (1992), and Subhash *et al.* (1993). Based on a detailed analysis of one-dimensional elastic wave propagation between the specimen and the elastic bars in

SHPB, Ravichandran and Subhash (1994) established limiting strain rates that can be attained in a ceramic specimen using the SHPB technique.

In this chapter, several aspects of the stress distribution within the specimen and the interaction between the hard ceramic and the pressure bars are investigated by means of numerical simulations of dynamic uniaxial compression experiments in SHPB. In Section 3.2 the problems associated with testing of hard ceramic in SHPB such as the indentation by hard ceramic into the bars, the resulting stress concentrations within the ceramic specimens and the influence of nonuniform stress distribution on failure strength of ceramics are discussed. In Section 3.3, experimental modifications presently available to the conventional SHPB technique are summarized briefly. The finite element model adopted for each specimen configuration is described in Section 3.4, and the results are presented and discussed in Section 3.5. Finally, in Section 3.6, conclusions are drawn based on the analysis, and recommendations are made for the testing of brittle materials using the SHPB.

3.2   Indentation of the Bar by a Hard Specimen

The conventional split Hopkinson pressure bar technique is a well established experimental method for high strain rate testing of ductile metals as discussed in Chapter 2. Strain gages mounted at midway points on the incident and transmission bars provide time-resolved measurement of pulses in the bars. The reflected pulse in the incident bar gives a measure of axial strain rate in the specimen, and the transmitted pulse in the transmission bar provides a measure of the axial stress in the specimen. The axial strain

rate is integrated with respect to time to yield the axial strain. The equations for strain rate $\dot{\varepsilon}$ and strain ε in the specimen can be estimated using

$$\dot{\varepsilon}(t) = -\frac{2c_0}{L}\varepsilon_r(t) \tag{3.1}$$

$$\varepsilon(t) = \int_0^t \dot{\varepsilon}(\tau)d\tau \tag{3.2}$$

where L is the original length of the specimen, ε_r is the time-dependent reflected strain in the incident bar, and c_0 is the elastic longitudinal bar wave velocity in the bar material. It should be noted that equations (3.1) and (3.2) become invalid when a dog-bone shaped specimen (Tracy (1987) and Cosculluela *et al.* (1991)) is used unless an appropriate value of the length (not just the gage length) can be determined to account for the non-uniform cross-section. If the appropriate value of length can not be determined, specimen strain gages must be used to record the strain history in the gage section of the specimen (Blumenthal et *al.* (1990) and Blumenthal (1992)). The axial stress σ in the specimen is determined using

$$\sigma(t) = \frac{A_0}{A_s}E\varepsilon_t(t) \tag{3.3}$$

where A_0 and A_s are the cross-sectional area of the transmission bar and the specimen respectively, E is the Young's modulus of the transmission bar material, and ε_t is the time-dependent axial strain in the transmission bar.

The major assumptions in deriving the above equations (3.1)-(3.3) are: (1) the specimen must be under a state of uniform stress during deformation; (2) the pressure bars must remain elastic at all times, and the ends of the bar in contact with specimen must remain flat and parallel during the deformation of the specimen; and (3) the various stress

pulses undergo minimal dispersion as they travel along the length of the bars, and the stress distribution across the cross-section of the bar is fairly uniform, (i.e., such that surface measurement techniques, such as strain gages, provide reliable measurement of the stress pulse).

The SHPB has traditionally been used to investigate plastic behavior of metals which are usually softer than the bar material. In this situation, the end surfaces of the bars in contact with the specimen remain nearly flat and parallel during the deformation, and all the assumptions are satisfied easily. This makes the SHPB a suitable technique for dynamic compressive testing of ductile materials. However, when working with ceramics which often undergo only elastic strain before failure, care must be taken to avoid violation of any of the assumptions detailed above. For example, a hard ceramic specimen will indent into the end surfaces of the pressure bars during loading, thus causing the following two problems. First, a stress concentration develops on the specimen edges, clearly violates the assumption of uniform stress distribution within the specimen which must be satisfied if transmission bar signal is to be used to estimate the stress in the specimen. Also, damage may initiate from the edges at a much lower stress level as compared to the stress level for damage initiation during the homogeneous deformation. Second, the indentation violates the second assumption that the ends of the bars in contact with the specimen will remain flat and parallel. This has been confirmed by numerical simulations as shown in Fig. 3.1 and will be discussed in detail in section 3.5. In addition, it has been noticed in actual experiments that the permanent indentation of the steel bars will affect the future experiments requiring more effort to maintain the equipment. Modifications have been suggested in the literature which are discussed in the following section to remedy these problems associated with indentation.

3.3   Modifications on SHPB to Remedy Indentation

In order to effectively make use of the conventional SHPB technique for ceramic testing, several specimen configurations have been used or proposed to reduce the effects of indentation and stress concentration. They include: (A) placing the specimen between two impedance matched tungsten carbide (WC) inserts, where the whole assembly is placed in the SHPB, as shown in Fig. 3.2, Case (5) as used by Cocculluela *et al.* (1991) and Subhash *et al.* (1993); (B) placing the specimen between two conical alumina (Al$_2$O$_3$) inserts as shown in Fig. 3.3, Case (6) (Anderson *et al.* (1992)); and (C) using a dog-bone shaped ceramic specimen shown in Fig. 3.2, Case (7) (Tracy (1987), Blumenthal *et al.* (1990), Cosculluela *et al.* (1991), and Blumenthal (1992)). The effectiveness of these modifications has been analyzed by numerical simulations of the experiments. A brief description of these modifications is given in the paragraphs that follow.

(A) In this case, the ceramic specimen is placed between a pair of identical cylindrical tungsten carbide inserts and the whole assembly is placed in between the incident and transmission bars in SHPB. The diameter of the inserts is determined by matching the impedance of the insert and the bar

$$(\rho c A)_{insert} = (\rho c A)_{bar} \qquad (3.4)$$

where ρ is the mass density, c is the elastic longitudinal bar wave velocity, and A is the cross-sectional area.

This method may be applied conveniently to the SHPB experiment with little additional cost. Since impedance of the inserts is matched with the bars, introduction of inserts should not alter the characteristics of the wave propagation in the bars.

(B) In this case, the experimental set up is similar to the one described above except that the inserts have a conical shape. The diameter of the inserts varies from that of the bar at one end to that of the specimen on the other end as shown in Fig. 3.2, Case (6). This gradual variation in diameter eliminates the indentation of the specimen into the bar. The impedance of this type of insert does not match with the bar impedance due to the variation of cross-sectional area along the length of the insert, although the impedance of the larger end of the insert is close to that of the bars. The matching diameters at each interface may significantly reduce indentation into the bars and stress concentrations in the specimen. However, this type of insert is not versatile, since different specimen diameters will require different inserts. In addition, the cost of fabricating this type of insert is considerably higher than the relatively simple cylindrical tungsten carbide inserts.

In experiments with hard ceramic specimens, the inserts in modifications (**A**) and (B) may fail before the specimen fails, especially when the inserts are used repeatedly. Once the inserts fail, the specimen often fails prematurely due to stress concentrations caused by the insert fragments. The tungsten carbide inserts have the advantage of higher strength as compared to the alumina inserts.

(C) The dog-bone shaped specimen design, which is shown in Fig. 3.2, Case (7), effectively combines the conical inserts and the specimen with smooth geometrical transition. This geometry is expected to minimize indentation into the bar and stress concentrations in the specimen. Clearly, making a dog-bone shape out of a ceramic material requires extreme care, and hence it is expensive to manufacture this type of specimen.

3.4. Finite Element Analysis

Numerical simulations of the SHPB technique have been performed by several investigators. Bertholf and Karnes (1975) conducted two-dimensional numerical analysis of SHPB experiments involving the effects of inertia and the friction between a metallic specimen and the elastic bars. Lichtenberger, *et al.*, (1988), examined specimen length-to-diameter ratio effects. Anderson, *et al.*, (1992), investigated the dynamic behavior of a ceramic up to failure and after failure using a two-dimensional numerical analysis.

The present study was undertaken to analyze the magnitude of the indentation in the bars and the resulting stress concentration in the specimen for various geometries discussed in the previous sections. Numerical simulations were performed on the Cray Y-MP at the San Diego Supercomputer Center using DYNA2D. DYNA2D is a Lagrangian, finite element code for analyzing the transient dynamic response of two-dimensional solids developed by the Lawrence Livermore National Laboratory. For details on DYNA2D, see Whirley, Engelmann and Hallquist (1992). A pre-processor, MAZE was used to construct the finite element model and to write the input file for DYNA2D. MAZE was also developed by Lawrence Livermore National Laboratory, see Hallquist (1983). ORION, an interactive color post-processor for two-dimensional finite element codes, was used to obtain the numerical simulation results. For details of ORION, see Hallquist *et al.* (1985).

Table 3.1. Details of the Finite Element Models Used in Various Cases of Fig. 3.2.

	Dimensions	Number of elements
Incident Bar	$\phi 1.27 \times 61$ cm	10x240
Transmission Bar	$\phi 1.27 \times 51$ cm	10x200
Striker Bar	$\phi 1.27 \times 10$ cm	10x40
Specimen (All Cases)	See Text	10x20
Each Al_2O_3 Insert	$\phi 1.27 \rightarrow \phi 0.635 \times 0.635$ cm	10×10
Each WC Insert	$\phi 0.8466 \times 0.3175$ cm	10×10

Table 3.2. Material Properties of the Bars, Inserts and Ceramic Specimens

	C-350 steel	WC	Alumina	AlN
Young's Modulus, E (GPa)	200	565.8	385	320
Mass Density, ρ (kg/m³)	8100	14500	3960	3250
Poisson's ratio, ν	0.29	0.20	0.215	0.237

The details of the finite element models adopted are given in Table 3 1, whereas the material properties of the bars, specimen, and inserts and are given in Table 3.2 The various finite element models analyzed are illustrated in 8 separate cases in Fig. 3.2. In order to demonstrate the magnitude of indentation during ceramic testing, a metallic specimen (Aluminum 6061-0) was used for Case 1. In Case 2, an aluminum nitride (AlN) ceramic is used without any inserts The results from these two cases are compared to emphasize the deviations from the basic assumptions in equations (3.1), (3.2) and (3.3) while testing hard ceramics In order to evaluate the effect of inserts on the wave propagation within the bars, the inserts were used without the ceramic specimen in Cases 3 and 4 Ceramic specimens with inserts were analyzed in Cases 5 and 6, and in Case 7, the dog bone specimen with a gage section diameter similar to those in Cases 5 and 6 was analyzed and compared. To investigate the effect of specimen size on the amount of indentation and the shape of transmitted pulse, Case 8 was considered for comparison with Case 7 The smaller specimen adopted in Case 8 was similar to that used by Cosculluela et *al.* (1991). This small size is found to cause indentation as well as distortions in pulse shape as will be discussed later The ceramic specimen, the inserts and the bars are assumed to be homogeneous and linearly elastic. The constitutive behavior of the aluminum specimen in Case 1 was described by a bilinear elastic-plastic, rate independent, isotropic hardening model with a Young's modulus of 68 GPa, Poisson's

ratio of 0.33, yield stress of 55 MPa, hardening modulus of 3.17 GPa and mass density of 2700 kg/m³.

In order to avoid unnecessary computing time, the incident and transmission bar lengths are chosen to be shorter than the actual lengths in the experiment (typically, a 12 7 mm diameter incident bar is 1200 mm in length). However, they are long enough to clearly distinguish the incident pulse, the transmitted pulse and specimen stress history on the same time-resolved plot for the given striker bar length. The element from which the incident and reflected pulses are read is located on the incident bar surface 30.5 cm from the end of the incident bar, representing the incident bar strain gage. The transmission bar strain gage was represented by an element 30.5 cm from the specimen end of the transmission bar. The cylindrical specimens were 1.27 cm long with a diameter of 0.635 cm. In Case 7, the gage section of the dog-bone specimen has the same dimension as the cylindrical specimens. The diameter of the end faces was matched with the bar diameter (1.27 cm). The overall length of the dog-bone specimen is 3.98 cm. The dog-bone specimen in Case 8 has the same shape as the one in Case 7, but the linear dimensions were reduced by a factor of 3 The initial velocity of the striker bar in all cases was 40 m/s. The impact of the striker bar with the incident bar generated the incident pulse in the incident bar. The rise time of the incident pulse increased from nearly zero at the impact surface to a finite value down the bar (6.4 μs at the mid-point of the incident bar). Since all the bars, inserts and the specimen have circular cross section, axisymmetric analysis was performed using 4-node elements. All the nodes on the symmetrical axis are constrained to move only along the axis. All the contacting surfaces between the bars, inserts and specimen were allowed to slide freely without any friction. For each case in Fig. 3 2, the simulation time was 240 μs which was sufficiently long to detect the complete signals at the effective strain gage positions. The time step was calculated automatically by the program depending on the element size used. Node and element data

were generated every 1.0 μs. It took 270 CPU seconds on the Cray Y-MP at the San Diego Supercomputer Center to simulate each case.

3.5. Results and Discussion

The results of the numerical simulations are presented and discussed in seven groups corresponding to each simulation geometry.

3.5.1 Magnitude of Indentation on the Bar Ends and the Specimen End Faces

Figure 3.1 illustrates the magnitude of indentation caused by the hard ceramic specimen (aluminum nitride) as compared to a metallic (aluminum) specimen in the absence of inserts. The maximum end surface deflections of the specimen and the bar, respectively, at the time of peak load are represented by "a" and "b" as shown in Fig. 3.1 (B). "a" is the axial distance from the center point to an edge point on the specimen end face deformed by the peak load, whereas "b" is corresponding distance on the bar end face. These deformed meshes were plotted at a time corresponding to the peak stress in the specimens for the same initial velocity of the striker bar (i.e., same incident pulse magnitude). Figure 3.1 illustrates clearly that, while testing metals in SHPB, the indentation in the bar (by the specimen) is negligible which assures uniform stress distribution throughout the specimen except near the end faces where stress state is affected by the friction between the specimen and the bars. However, in simulations of tests on high strength ceramics, the magnitude of indentation was significantly large resulting in a three-dimensional stress state in the specimen and obvious stress

concentrations. For all the cases that were analyzed, the magnitude of indention was determined and tabulated in Table **3.3.** These values are used as a measure of indentation in all the cases. Inspection of Table **3.3** indicates that the indentation is **13** to **17** times more in Case 2 than in Case 1. When evaluating ceramics, clearly the indentation into the bars was considerably higher, which calls for methods to minimize the problem by using various kinds of inserts between the specimen and the bars as described in Section **3.3.** When impedance matched high strength tungsten carbide inserts were placed between the specimen and the bar, the values reduced almost **3.5** times. When conical alumina inserts were used, the indentation on the specimen, i.e., the value of "a" was reduced by the same amount as the tungsten carbide inserts, while the indentation on the bars was reduced by 10 times as a result of the diameter match. For practical applications, the alumina conical inserts have the disadvantage of having lower strength as compared to tungsten carbide inserts. For the case of dog-bone shaped specimen with end diameter matched with that of the bars (Case 7), there was negligible indentation, thus making this specimen geometry ideal for ceramic testing. However, this geometry has the disadvantages of high cost of machining the specimens, and the difficulty in defining the specimen length. On the other hand, if the specimen end diameter does not match with the bar diameter as shown in Case 8, severe indention will occur as indicated in Table **3.3.**

Table **3.3** Magnitude of Indentation for Each Case Depicted in Figure **3.2.**

Case	a (mm)	b (mm)
1	0.0026	0.0066
2	0.034	0.11
3	/	0.03
4	/	0.011
5	0.01	0.03
6	0.01	0.011
7	~0	~0
8	0.025	0.077

3.5.2 Axial Stress Concentration in the Specimen

Figure **3.3** compares the profiles of axial stress in the ceramic specimen shown in Case 2 of Fig. 3.2 at two points on an end face of the specimen. Point "e" was on the circumferential boundary while point "c" was on the axis of the specimen. Inspection of Fig. **3.3** indicates that upon loading the stress at the corners was 2.7 times the stress at the axis, which demonstrates that the ceramic specimen would not be under uniform state of stress. The stress concentration at the corners may initiate failure before the specimen reaches equilibrium. Hence under such circumstances, reliable data on failure strength cannot be obtained experimentally.

The stress concentration factor K is defined as the ratio of the axial stress at the circumferential element σ_e to the axial stress value at the center element σ_c at peak load (see Fig. 3.3), i.e.,

$$K = \frac{\sigma_e}{\sigma_c} \qquad (3.5)$$

The peak load occurred approximately 150 μs after impact. The values of K for the various cases are listed in Table **3.4.** The corresponding stress distribution in each of the specimen configurations will be discussed later. Clearly, high stress concentrations may initiate failure in these locations and give erroneous data on failure strength.

Table 3.4 Stress Concentration in the Specimen in Various Cases.

Case	K
1	≈1
2	2.7
5	1.75
6	1.58
7, 8*	~1

* Gage section only

From the data shown in Table 3.4, it is apparent that the largest stress concentration occurs in Case 3 where the ceramic was tested in SHPB without any inserts. This is due to the large indentation of the specimen into the relatively soft bar end as shown in Fig. 3.1 (B)   When the specimen was placed between tungsten carbide inserts, the specimen surfaces in contact with the WC remain nearly flat since the tungsten carbide is much harder than the bar material, thereby reducing the stress concentrations considerably. The conical alumina inserts krther reduced the stress concentrations since there was very little indentation occurred as a result of the matching diameters. There are two factors which may induce stress concentrations in the specimen when conical inserts are used. First, if the Poisson's ratios of the specimen and the inserts are different, a mismatch in the diameter at the interface will occur during axial loading. In addition, if damage develops in the specimen or in the inserts during loading, the lateral expansion produced by the opening of the axial cracks may cause further diameter mismatch. Second, although the geometric transition from the insert to the specimen was continuous, it was not smooth   In the case of the dog-bone specimens where the transition is smooth, there were virtually no stress concentrations in the entire gage section of the specimen. In Case 7, there was no indentation and no stress concentration where a diameter matched dog-bone specimen was used. In Case 8, the stress concentration factor on the end faces of the specimen (i.e., the bar contacting faces) was equal to 2. Since the area of the bar end face was 4 times the cross-sectional area of the gage section, the stress in the gage section is 2 times the stress value at the edges. Therefore, for homogeneous material, the damage in the specimen will initiate from in uniformly stressed gage section.   For this reason, failure would be expected to occur in the gage section in both dog-bone specimen geometries shown in Cases 7 and 8, resulting in more realistic values of the failure strength at high strain rates

3.5.3 Stress Equilibration in the Specimen

The axial stress profiles in the elements at the centers of both end faces of the specimen for Case 2 are presented in Fig. 3.4. Element "a" is at the center of the incident bar interface, and element "b" is at the center of the transmission bar interface. The relative stress difference ratio, D, is defined as:

$$D = \left| \frac{\sigma_a - \sigma_b}{\sigma_a} \right| \tag{3.6}$$

The ratio D is also plotted against the time on Fig. 3.4. It should be noted that the ratio D continues to fall as time progresses indicating that the specimen eventually reaches equilibrium. The value of D oscillates around small values near zero as time increases further (>132 ps). Ideally, the difference in stress across the specimen length would be zero to satisfy the assumption of uniaxial stress prior to failure initiation and data on failure strength is obtained. In practice, this situation may never be realized in dynamic conditions where the incident stress continues to rise very rapidly. Hence, it will be assumed that the stress within the specimen is equilibrated when the ratio falls below 5%. It can be seen from Fig. 3.4 that it takes $\Delta t = 9.2 \, \mu s$ for the relative stress difference to be within 5% for this specimen geometry and strain rate condition.

The elastic longitudinal bar wave velocity, c_{AlN}, of the aluminum nitride specimen is 9.92×10^3 m/s. The specimen length, I, is 1.27 cm. Thus, the number of the round-trips, N, the axial stress wave travels in the specimen before D<5% is:

$$N = \frac{\Delta t}{2l / c_{AlN}} = 3.59 \qquad (3.7)$$

implying that the stress wave must travel through the specimen at least 4 times before the stress reaches equilibrium. If failure occurs before this condition is met, then the data on failure strength may be considered invalid. In addition, it has been demonstrated that the data obtained from the strain gages on the bars become invalid beyond a critical strain rate as a result of wave dispersion effects, see Ravichandran and Subhash (1994).

3.5.4 Reflected Pulses in the Incident Bar in the Presence of Inserts

It is important to keep in mind that the main purpose of the inserts is to avoid indentation of the ceramic into the bar during loading without altering wave propagation in the bar. Ideally, when no specimen is present, and if both the incident and transmission bars are in good contact with the inserts, then there should be no reflected pulse ($\varepsilon_r=0$): all the incident pulse should be transmitted to the transmission bar through the inserts without distortion, The inserts which cause minimal distortion of the waves should be chosen whenever possible. Figure 3.5 compares the magnitude of reflected pulses in the incident bar from impedance matched tungsten carbide cylindrical inserts and conical alumina inserts (in the absence of specimen) as shown in Cases 3 and 4 of Fig. 3.2, for the incident pulse shown in Fig. 3.6. In Case 3, 9.37% of the incident pulse was reflected primarily due to the mismatch in diameters of the bars and the tungsten carbide inserts which may cause local three-dimensional effects. In Case 4 where conical alumina inserts are used, 21.25% of the incident pulse was reflected. The larger reflected pulse in Case 4 was due to the impedance mismatch between the bars and the inserts. In addition, it is possible that the continuous change in cross section of the conical shape may contribute to such a large

reflected pulse. Considering the cost, strength, and wave propagation characteristics of these two types of inserts, the impedance matched tungsten carbide cylindrical inserts generally are recommended.

3.5.5 Pulse Shapes in the Bars and in the Specimen

The SHPB was designed originally to investigate the plastic deformation behavior of metals: the transmitted and the reflected pulses indicate the plastic behavior of the metal under investigation as expressed by equations (3.1), (3.2) and (3.3). Figure 3.7 illustrates the axial stress profiles detected at the mid-points of the transmission bar and the specimen for Case 1 of Fig. 3.2. The amplitude of the specimen pulse has been normalized by the ratio of the bar to specimen cross-sectional area. The incident pulse in this case was identical to that shown in Fig. 3.6. The shapes of the stress pulses from the specimen and the transmission bar were very similar, but clearly different from the incident pulse. This was caused by the plastic behavior of the ductile aluminum specimen. In the case of elastic ceramic specimen under uniaxial stress wave propagation, it is clear that the pulse shape and duration should not change as the incident pulse travels through the specimen and the transmission bar as illustrated in Fig. 3.6 for Case 5 (the specimen pulse was again normalized by the cross-sectional area ratio). Analysis of Cases 6 and **7** yielded very similar results in terms of pulse shape. There was a slight increase in rise time of the stress pulse as it traveled through the specimen and the transmission bar due to the dispersive nature of wave propagation, however, the shape of the pulses remained nearly the same as shown in Fig. 3.6. Hence, it may be concluded that the stress in a ceramic specimen undergoing elastic deformation can be determined from either the strain gage on the specimen or from the strain gage on the transmission bar, provided that the stress distribution in the bar is one-dimensional. The requirement of a stress state again

demonstrates the importance of considering indentation effects that may result in a three-dimensional stress state. If a ceramic specimen is made suitably small as in Case 8, it acts as an indentor into the bar resulting in a three-dimensional state of stress in the bar and the specimen. Even though the ceramic specimen undergoes elastic deformation, the shape of the pulse will not remain the same as it travels through the specimen and in the transmission bar due to three-dimensional state of stress. Figure 3.8 illustrates the profiles of stress pulses for Case 8 where the specimen size was very small as compared to Case 7. The specimen pulse was normalized by the cross-sectional area ratio. Comparing Fig. 3.8 to Fig 3.6, it can be clearly seen that, the two sets of pulses were drastically different due to the three-dimensional state of stress at the specimen/bar interfaces even though the specimen shape and loading conditions were identical in both cases. Under these circumstances, the failure stress obtained in ceramics cannot be considered to be a correct measure since the stress state in the specimen is not uniaxial.

In Fig. 3.8, it is also seen that the rise time of the pulse increased as it traveled through the specimen and the transmission bar. The rise time of the stress pulse in the specimen was 31 μs, whereas that of the incident pulse was 6.4 μs. The rise time is defined as the duration between the points where the pulse magnitude reaches 5% and 95% of its peak value. In order to investigate the specimen size effect and its influence on the rise time, a series of simulations were run with a range of specimen/bar diameter ratios based on the specimen of Case 8. The length of the specimen was kept constant (1.27 cm) in these simulations. The results are presented in Fig. 3.9 in which the specimen gage section diameter normalized by the bar diameter is plotted versus axial stress pulse rise time detected at the center of the specimen normalized by incident pulse rise time. In the normalized diameter range of 0.15-0.50, the rise time decreased almost linearly as the diameter increased. At normalized diameters greater than 0.5, the specimen stress pulse rise time approaches the incident pulse rise time asymptotically (gage section diameter was

used for Cases 7 and 8). This result indicates that the specimen diameter is a key parameter which determines the strain rate in the specimen as compared to the incident stress rate or imposed strain rate. Typically, ceramic specimen diameters are kept less than half of the bar diameter corresponding to normalized diameters less than 0.5, in order to obtain the very high stress levels required to fracture ceramics. Consequently, the strain rates achieved in the ceramics are often considerably less than those observed in metals.

3.5.6 Stress Signals in the Transmission Bar

In order to verify the assumption that the stress distribution across the cross section of the bar remained uniform, the profiles of axial stress pulses were plotted at three points on the cross section where the strain gage representing element was located on the transmission bar (not shown in figures). One point was on the circumference, another was at the center, and the third was half way in between. These three profiles were found to be identical on the plot, which implies that the stress distribution across the bar was uniform. Hence, surface measurement techniques, such as strain gages, may be used to measure axial strain in the bars. This result was repeated in all the cases at the selected striker bar velocity of 40 m/s used in this investigation.

In dynamic uniaxial compression experiments using the SHPB technique, the axial stress in the specimen is calculated from the transmission bar signal (see equation (3.3)). Therefore, it is important to be aware of the possible differences between the stress value calculated from the transmission bar signal and the actual stress in the specimen. For all the cases analyzed in this study, the stress calculated from transmission bar signal were within 5% of the actual stress read directly from the center of the specimen. However.

the transmission bar signal cannot resolve the local three-dimensional state of stress caused by any possible indentation due to dispersion.

3.5.7 Stress Distribution in the Specimen

At the peak load on the specimen, the axial stress distributions in the specimens for Cases 1, 2, 5, 6, 7 and 8 are shown in Fig 3.10   Evaluation of Fig. 3.10 shows that in all Cases except Cases 1 and 7, there were local stress concentrations near the edges of the specimens. The magnitude of the stress concentration has been discussed in section 3.5.1 for all these cases. Away from the edges, the stress distributions inside the specimens are quite uniform.   For Case 1, there was no apparent stress concentration because the metallic specimen deformed plastically and specimen end friction was neglected.   The material near the corners yielded first, after a certain loading level was reached.   Therefore, if ductile materials are of interest, the stress concentrations would not affect the stress-strain data obtained from the SHPB experiment.   In the case of hard and brittle materials, these stress concentrations may cause premature failure (for example, chipping) of the specimen by initiating crack growth in these regions.   For the dog-bone shaped specimen shown in Case 7, the stress distribution in the whole gage section was uniform, and there was no stress concentration at the edges due to the matched specimen and bar diameters, thereby completely eliminating the problems associated with stress concentration and indentation.   This design is ideally suited for testing of ceramics to obtain their failure strength.   The smaller size dog-bone specimen shown in Case 8 also did not introduce stress concentration in the gage section and the magnitude of stress at the edges is smaller than in the gage section   It should be noted that Cosculluela *et al.* (1991) obtained similar results on their dumb-bell shaped specimen.   However, the geometry has

the disadvantage of introducing a three-dimensional state of stress in the bar which affects the magnitude and duration of the transmitted pulse as discussed before in Section 3.5.5.

3.6. Conclusions

Based on the results and discussion above, the following conclusions can be drawn from this numerical simulation study:

(I) The conventional SHPB technique where the specimen diameter is less than the bar diameter may not be applied directly to hard and brittle material testing due to indentation of the specimen into the bars and the resulting stress concentration in the specimen. Modifications must be incorporated to overcome these problems.

(2) The impedance matched cylindrical tungsten carbide inserts and the diameter matched conical alumina inserts had roughly the same effect in reducing the indentation and stress concentrations within the specimen. The impedance matched tungsten carbide inserts are recommended over the alumina conical inserts due to their higher strength and lower cost.

(3) Of the three modifications investigated in this analysis, the dog-bone specimen design with diameter matching ends with the bar was the best method to overcome the stress concentrations caused by indentation. However, extreme care is required to make such a complicated geometry from a ceramic material. In addition, these would add drastically in the cost of specimen fabrication.

(4) Specimen diameter is an important parameter in the strain rate reduction in the specimen from the imposed incident strain rate. Reducing the specimen diameter beyond a reasonable limit may also violate the basic assumption of a uniaxial stress state.

3.7 References

Anderson Jr., C. E.. O'Donoghue, P. E., Lankford, J. and Walker. J. D., (1992), "Numerical Simulations of SHPB Experiments for the Dynamic Compressive Strength and Failure of Ceramics," *International Journal of Fracture*, 55, pp. 193-208

Bertholf, L. and Karnes, C., (1975), "Two-Dimensional Analysis of the Split Hopkinson Pressure Bar System," *Journal of Mechanics and* Physics *of* Solids, **23,** pp. 1-19.

Blumenthal, W R. and Gray, III, G. T., (1990), "Characterization of Shock-Loaded Aluminum-infiltrated Boron Carbide Cermets," in *Shock Compression of Condensed Matter*--1989, edited by Schmidt, S. C., Johnson, J. N. and Davison, L. W., Elsevier Science Publishers, pp. 393-396.

Blumenthal, W. R., (1992), "High-Strain-Rate Compression and Fracture of B_4C-Aluminum Cermets," in Shock-Wave and *High-Strain-Rate* Phenomena *in Materials*, edited by Meyers, M. A., Murr, L. E. and Staudhammer, K. P., Marcel Dekker, Inc., pp. 1093-1100.

Cosculluela, A., Cagnoux, J. and Collombet, F., "Two Types of Experiments for Studying Uniaxial Dynamic Compression of Alumina," in *Shock Compression of Condensed* Mutter, edited by Schmidt. S. C., Dick, R. D., Forbes, J. W., and Tasker, D. G, pp. 951-954.

Follansbee, P. S., (1985), "The Hopkinson Bar," in *Mechanical Testing, Metals Handbook*, **8,** 9th edition, American Society for Metals, Metals Park, Ohio, pp. 198-217.

Hallquist, J., (1983), "MAZE: An Input Generator for DYNA2D and NIKE2D," UCID-19029.

Hallquist, J. and Levatin, J., (1985), "ORION: *An* Interactive Color Post-Processor for Two-Dimensional Finite Element Codes," UCID-19310.

Kolsky, H., (1949), *"An* Investigation of the Mechanical Properties of Materials at Very High Rates of Loading," *Proc. Roy. Soc., London,* **B62,** pp. 676-700.

Lichtenberger, A., Gazeaud, G. and Lach, E., (1988), "Essais de Compression Sur Barres d'Hopkinson: Simulation Numerique et Etude Experimentale," *Journal de Physique,* **49**(NC-3), pp. 589-594.

Lindholm, U. S., (1964), "Some Experiments with the Split Hopkinson Pressure Bar," *Journal of Mechanics and Physics of Solids, 12,* pp. 317-335.

Nemat-Nasser, S., Isaacs, J. B. and Starrett, J. E., (1991), "Hopkinson Techniques for Dynamic Recovery Experiments," *Proc. R. Soc. Lond.* **A435,** pp. 371-391.

Ravichandran, G and Chen, W., (1991), "Dynamic Failure of Brittle Materials Under Uniaxial Compression," in *Experiments in Micromechanics of Fracture Resistant Materials,* AMD130, ASME WAM, Atlanta 1-6 December 1991, edited by Kim, K.-S., pp. 85-90

Ravichandran, G. and Subhash, G.. (1994), "Critical Appraisal of Limiting Strain Rates for Compression Testing of Ceramics in a Split Hopkinson Pressure Bar," *Journal of the American Ceramic Society*, **77**(1), pp. 263-267.

Subhash, G. and Nemat-Nasser, S., (1993), "Uniaxial Stress Behavior of Y-TZP," *Journal of Materials Science*, **28,** pp. 5949-5952.

Tracy, C. A., (1987), "A Compression Test for High Strength Ceramics," *Journal of Testing and Evaluation* JTEVA **15**(1), pp. 14-19.

Whirley, R., Engelmann, B. and Hallquist, J., (1992), "DYNA2D: A Nonlinear, Explicit, Two- Dimensional Finite Element Code For Solid Mechanics, User Manual," UCRL-Ma-110630.
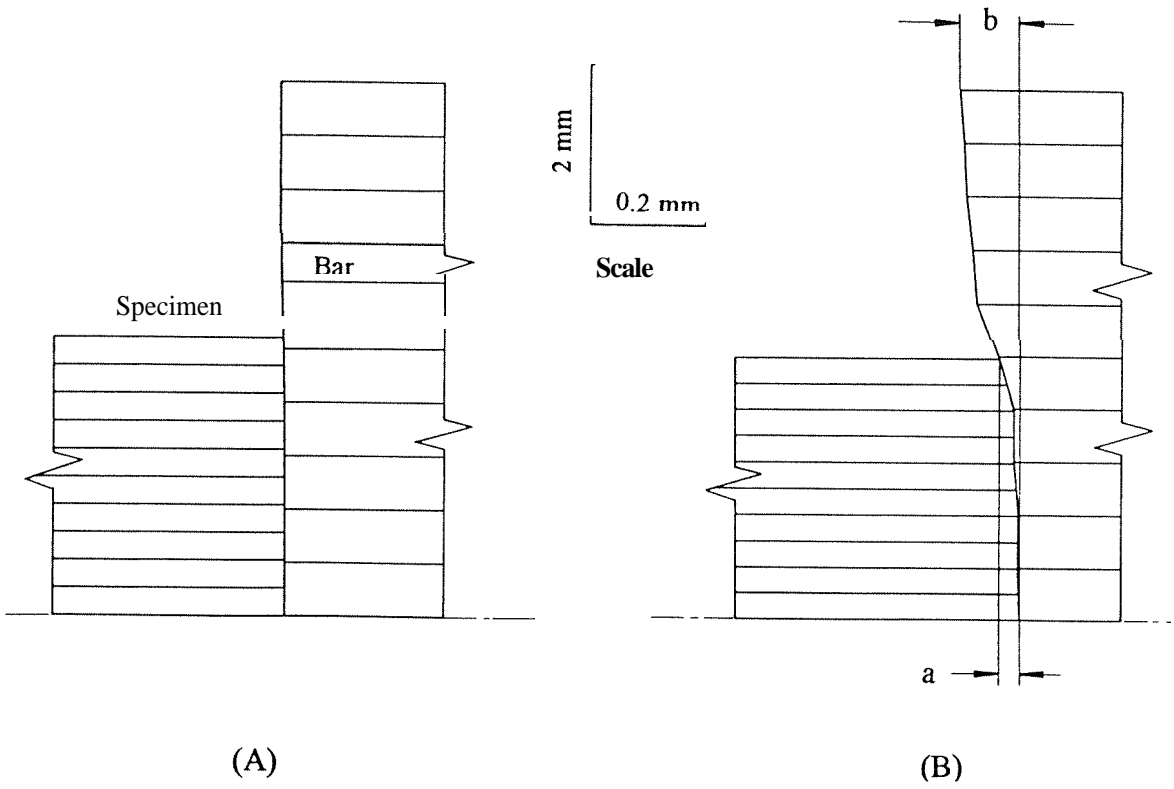
Figure 3.1 An illustration of indentation at the specimen/bar interface.
(A) Aluminum specimen   (B) AIN specimen
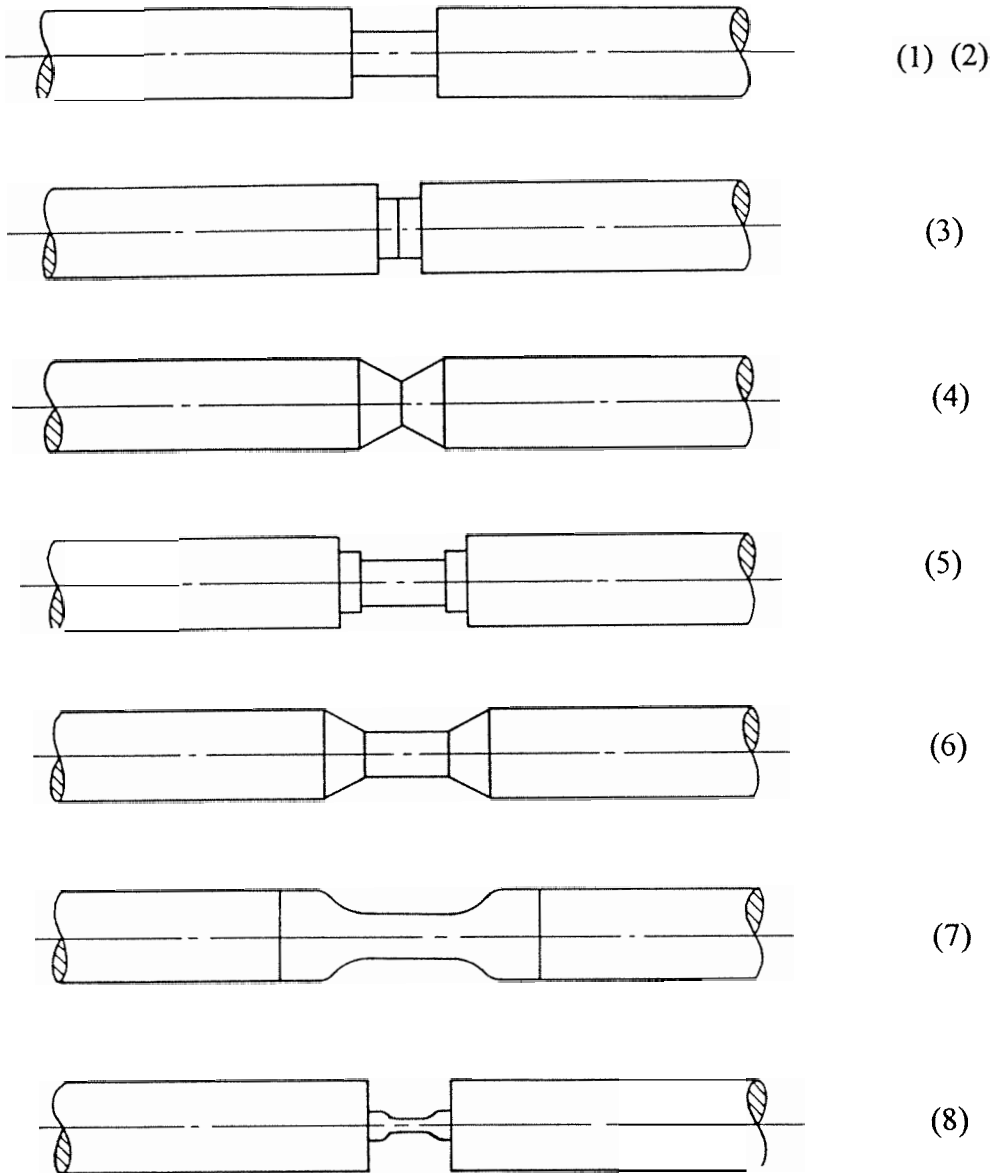
Figure 3.2 Schematic of various cases:
(1) Metallic specimen without inserts, (2) Ceramic specimen without inserts, (3) Cylindrical WC inserts only, (4) Conical Al_2O_3 inserts only, (5) Ceramic specimen with cylindrical WC inserts, (6) Ceramic specimen with conical Al_2O_3 inserts, (7) Dog-bone specimen with matching diameters, (8) Dog-bone specimen with non-matching diameters.
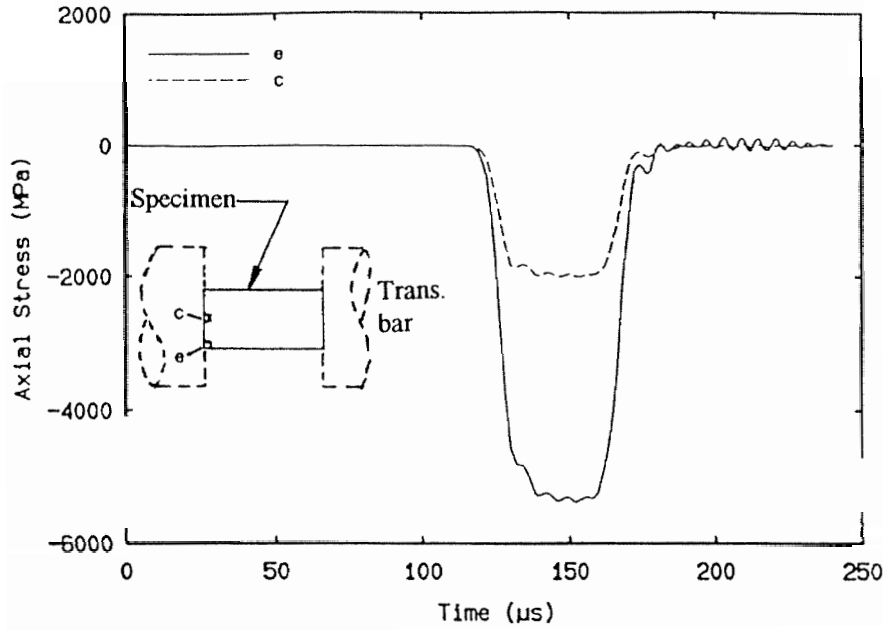
Figure 3.3 Axial stress profiles illustrating the stress concentration at the specimen corner for Case 2.
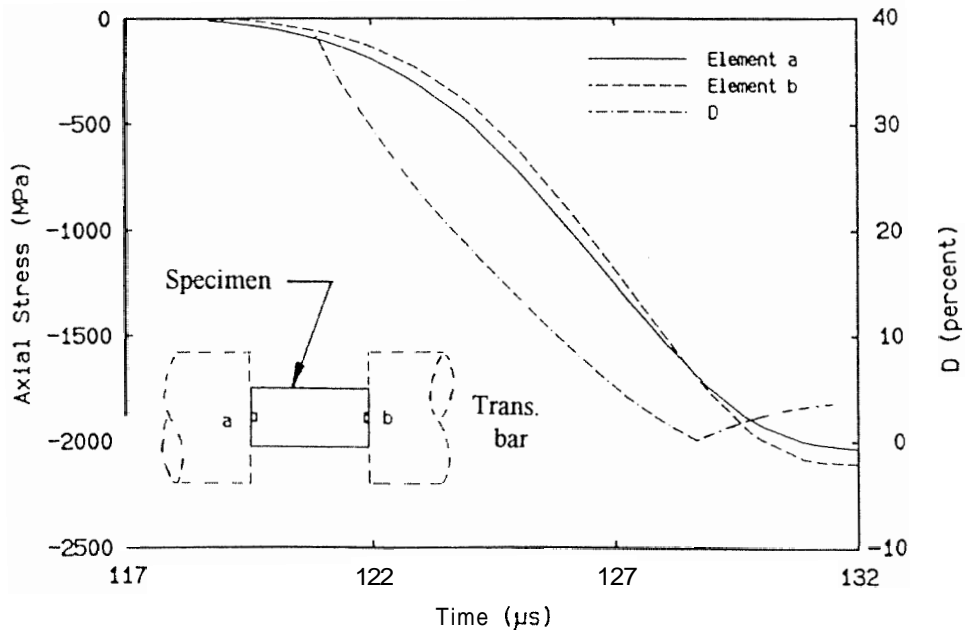
Figure 3.4 Time to equilibrium in the Case 2 specimen during an SHPB experiment.
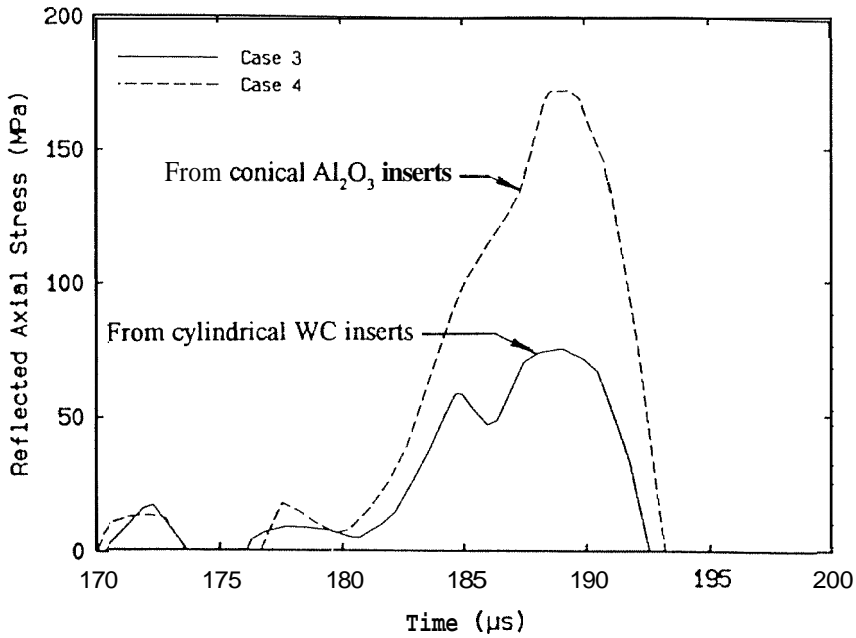
Figure 3.5 Details of reflected pulses for Cases 3 and 4:
Note that, when impedance matched WC inserts (Case 3) are used, the magnitude of the reflected pulse is considerably smaller than the reflected pulse when conical inserts (Case 4) are used.
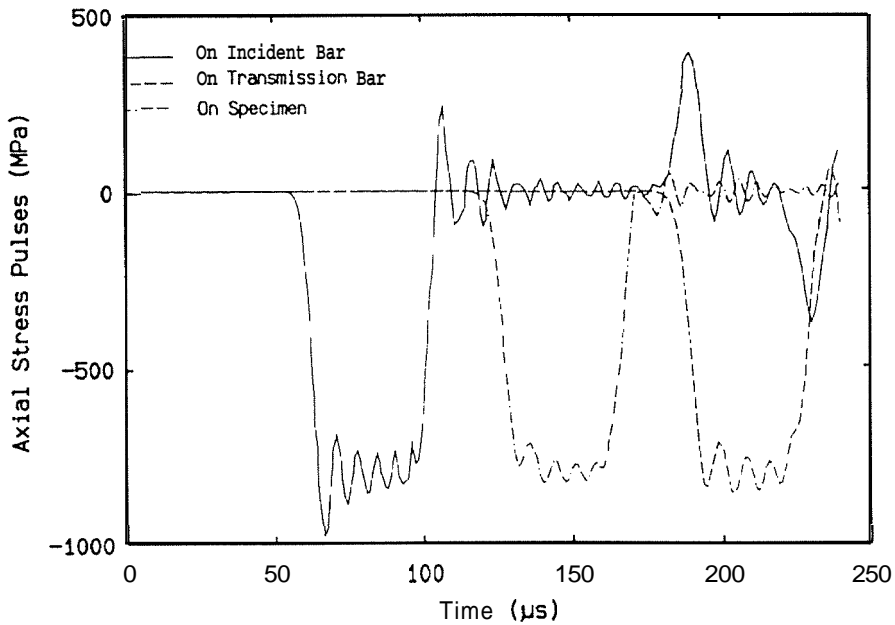
Figure 3.6 Profiles of stress pulses measured on incident bar, transmission bar and specimen for Case 5. These pulses are very similar for Cases 6 and 7 also.
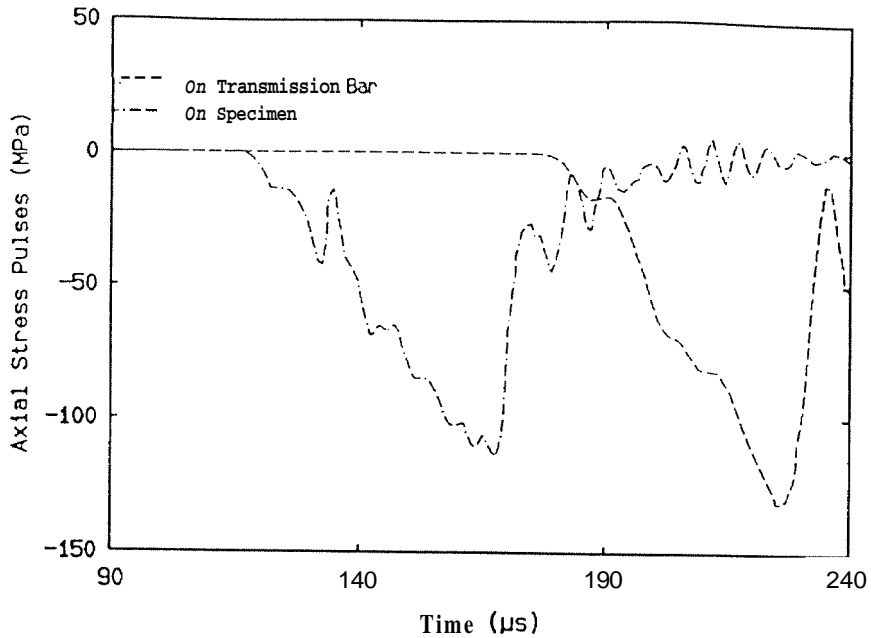
Figure 3.7   Stress profiles measured on the ductile specimen and transmission bar
for the same incident pulse shown in Fig. 3.6 for Case 1.
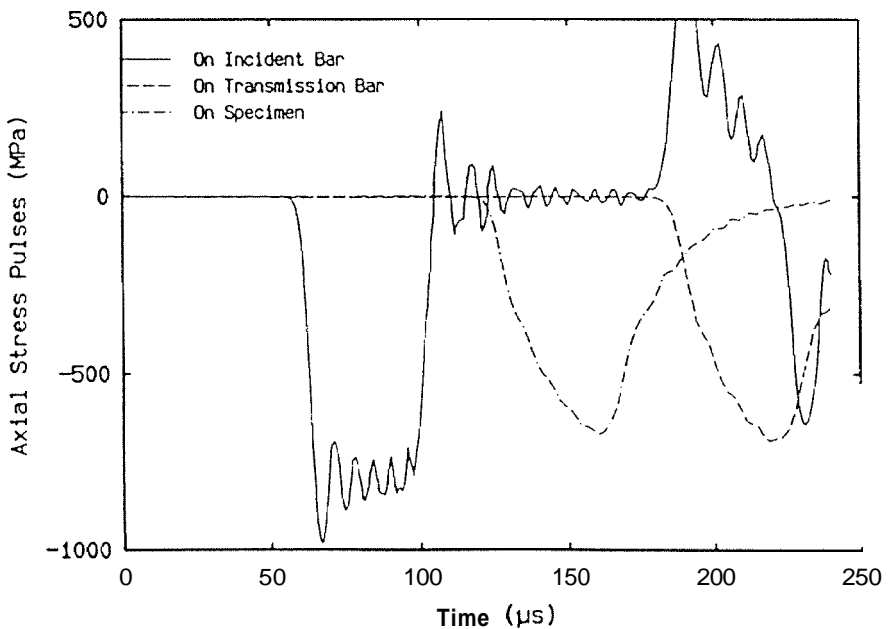
Figure 3.8 Incident, transmission arid specimen axial stress pulses for Case 8.
Note the reduction in amplitude and the increase in rise time and duration in
specimen and transmitted pulses as compared to the pulses in Fig. 3.6.
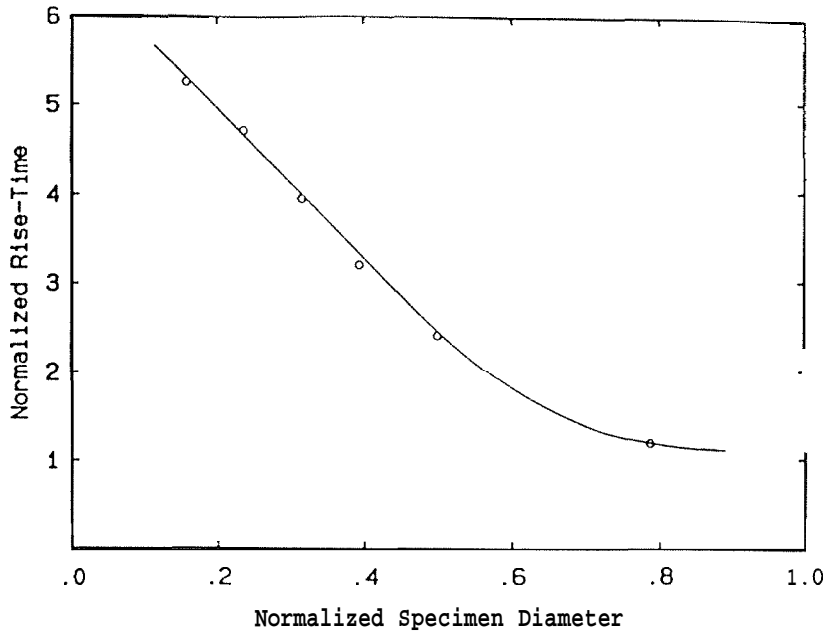
Figure 3.9 Specimen axial stress rise time as a function of specimen diameter:
        As the specimen diameter approaches the bar diameter, the rise time of the
        axial stress pulse in specimen equals that of the incident bar.
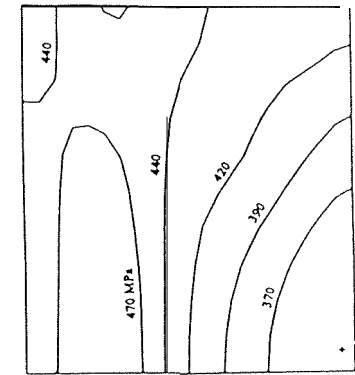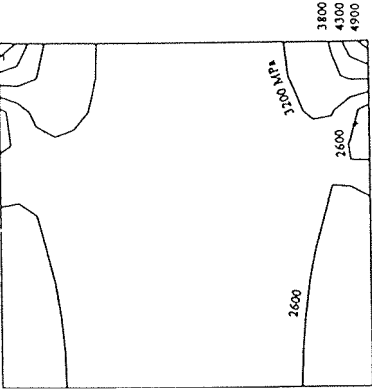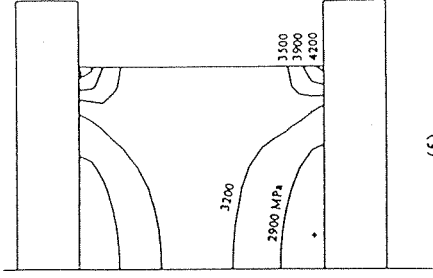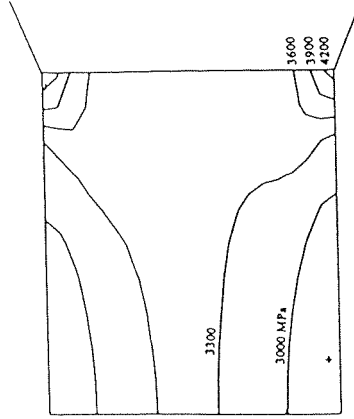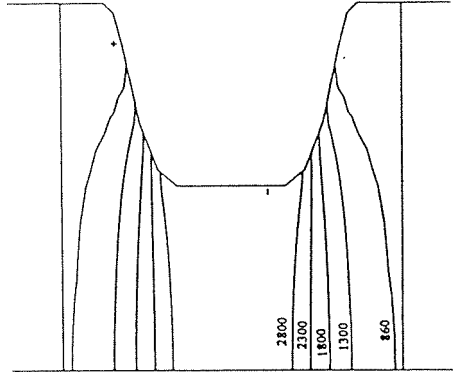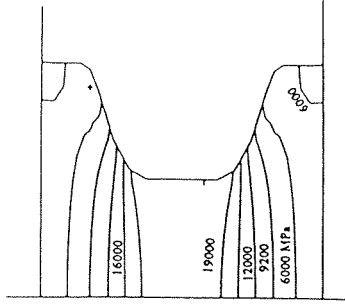
Figure 3.10 Axial stress distributions in the specimens for various cases.

Chapter 4

Experimental Techniques for Imposing Controlled Dynamic Multiaxial Compression

Abstract

Two experimental techniques have been developed for imposing controlled lateral confinement on specimens subjected to dynamic uniaxial compression. Descriptions of the experimental techniques, as well as demonstrative experimental results on Macor and aluminum nitride are presented in this chapter. The axial compression was applied using a split Hopkinson pressure bar modified to apply a single loading pulse. The cylindrical specimens were confined laterally either by eletro-magnetic force, or by a shrink fit metal sleeve. The electro-magnetic confinement is an ideal approach to apply dynamic proportional loading, whereas the metal sleeve can retain the tested specimen for failure mode characterization. Macor was tested using the electro-magnetic method, and aluminum nitride was tested by the metal sleeve approach. The results show that the failure occurs by fragmentation due to axial splitting under uniaxial stress condition for both materials. Under moderate lateral confinement provided by the metal sleeves, failure of aluminum nitride occurs by localized deformation on faults. The propensity of the Macor to fragment under uniaxial stress was suppressed even by very low lateral confinement generated electro-magnetically. The dynamic compressive failure strength of Macor increased from 0.53 GPa under uniaxial stress (without confinement) to 0.63 GPa when a confining pressure of −10 MPa was imposed The dynamic compressive strength of aluminum nitride increased from 4.3 GPa without confinement to 5.4 GPa with 230 MPa of confinement.

4.1 Introduction

Due to rapid advances in processing technology, high strength ceramics and ceramic composites are being developed with exceptional mechanical properties, and they are being used increasingly in structural applications. In order to use these materials properly and efficiently in a variety of impact related applications, it is necessary to develop constitutive models to describe the mechanical behavior and failure modes in these materials under multiaxial dynamic loading conditions. The failure strength of brittle materials has been predicted to increase even under moderate amounts of lateral confinement. This has been observed experimentally in rocks and ceramics under static confinement and quasi-static loading, see Heard and Cline (1980), Horii and Nemat-Nasser (1986), Arrowood and Lankford (1987), Ashby and Sammis (1990). Currently, the experimental techniques available to evaluate the dynamic response of ceramics essentially are limited to either one-dimensional stress (Lankford, 1977) or one-dimensional strain (Raiser and Clifton, 1993, Grady, 1995) loading conditions. New experimental techniques need to be developed which are capable of dynamically loading the brittle specimens over the range of stress states from 1-D stress to 1-D strain.

In this chapter, two experimental techniques to apply radial confining pressure to an axially loaded cylindrical specimen are presented. The axial loading device was the modified split Hopkinson (Kolsky) pressure bar (SHPB) which was presented in Chapter 2. Using this technique, it is possible to recover the specimen after subjecting it to a single loading pulse; this feature facilitates further investigation of failure modes and the of relation between the microstructure and the macroscopic behavior. The cylindrical ceramic specimens were confined laterally either by electro-magnetic force or by a shrink fit metal sleeve. Experimental results have been obtained for a machinable glass ceramic,

Macor, under electro-magnetic confinement, and for a monolithic ceramic, sintered aluminum nitride (AlN) under mechanical confinement.

The principles, the experimental setups and the experimental results for the electro-magnetic and mechanical confinement methods are presented in Sections 4.2 and 4.3, respectively. Conclusions based on the experimental results are drawn in Section 4.4.

4.2   Eletro-Magnetic Confinement

4.2.1 Experimental setup

A schematic of the experimental setup is shown in Fig. 4.1. The same SHPB facility described in Chapter 2 was used for generating uniaxial compression pulses of known duration, shape and amplitude. Impedance matched tungsten carbide (WC) platens were placed between the specimen and the bar end faces as described in Chapter 3. Dynamic confinement was achieved by using an eiectro-magnetic force generator, which consists of a copper strip surrounding the specimen and a capacitor bank. The capacitor bank, which has an energy capacity of −120 kJ, is consisted of capacitors connected by inductances such that the capacitors will discharge in a given sequence. The capacitor bank was used by Ravi-Chandar and Knauss (1984) to apply dynamic load on the surfaces of a mode I crack in a PMMA plate. The copper strip provides a path for high intensity electric currents flowing in opposite directions around the specimen, as shown in Fig. 4.2. When current passes through the copper strip, the resulting eletro-magnetic force will move the two layers apart from each other. The outer layer of the copper strip tends to expand outwards but is restricted by a rigid mass, and the inner strip tends to move inwards against the specimen. Thus, the electro-magnetic force will generate pressure on

the specimen lateral surface. A cylindrical specimen shape is preferable to obtain an evenly distributed confining pressure over the lateral surface of the specimen The electro-magnetic method of applying confinement has two principal advantages: (1) Pulse tailoring: the dynamic confining pressure pulse can be tailored to the desired shape, amplitude and duration through proper design of the circuitry associated with the capacitor bank. This feature enables the application of the multiaxial compression loading either proportionally or non-proportionally. Due to the transient nature of impact related applications, it is desired that the experimental technique be able to apply both proportional and non-proportional loading paths to study failure mode transition in engineering ceramics at different strain rates and under various amounts of confinement. In proportional multiaxial loading, the loads in principal directions increase and decrease proportionally. The dynamic lateral confinement induced by inertial effect, for example, is proportional to the axial impact loading. (2) Timing: in order to apply proportional loading on the specimen, the confinement pressure should initiate and terminate with the axial loading. Therefore, the timing of the confinement pulse should be very accurate in every experiment. In the electro-magnetic technique, the timing is controlled by an ignition trigger delay circuit and a thyratron/mercury switch ignition unit as shown in Fig. 4.1, and a repeatable accuracy of within one microsecond is achievable.

In the experiments presented later in this Section, the timing of the SHPB and the capacitor bank discharge system were coordinated by a photo-interrupter and a time delay circuit. When the projectile passed through the photo-interrupter, the time delay circuit was triggered, which in turn triggered the discharge system at the instant when the axial stress pulse arrived at the specimen The modified SHPB loaded the specimen by a single, well defined pulse, and the electro-magnetic pressure pulse could be tailored and timed to match the axial compressive pulse. Therefore, the specimen was loaded by well-

characterized loading pulses both in the axial and lateral directions. This facilitates the investigation failure mode in the recovered specimen.

As described in Chapter 2, the acquisition and interpretation of data for the SHPB have been well established. For the confinement loading, the rate of current flow in the copper strip was measured by a Rogovski coil (Ravi-Chander and Knauss, 1984). The output of the coil was integrated with respect to time by a simple integration circuit to obtain the current history. In the case of two concentric layers of currents at same amplitude but opposite directions as shown in Fig. 4.3, the electro-magnetic confining pressure P is given by

$$P = \frac{\mu_0}{4} \left(\frac{i}{b} \right)^2 (\cos\alpha_1 - \cos\alpha_2) \qquad (4.1)$$

where μ_0 is the coefficient of permeability ($4\pi \times 10^{-7}$ henry/m in vacuum), and i is the total current in one layer. The dimension b and the angles, a, and a, are defined in Fig. 4.3. It is clear from Eqn. (4.1) that the confining pressure will not be uniform along the axial direction on the lateral surface of the specimen. The non-uniformity will depend on the length to diameter ratio of the specimen. The calculated pressure distribution along the specimen axis is shown in Fig. 4.4 for a length to diameter ratio of 1. Inspection of Fig. 4.4 indicates that the pressure near the specimen ends is 35% less than the pressure on the middle section of the specimen.

4.2.2 Results

The feasibility of the experimental technique was assessed using a machinable glass ceramic, Macor. The mechanical behavior of Macor under uniaxial stress was described in

detail in Chapter 2. The glass ceramic has a Young's modulus of 68 GPa and a quasi-static compressive strength of 350 MPa The cylindrical specimens used in these experiments were 8.10 mm in diameter and 5.38 mm in length.

In order to investigate the failure mode change, a striker bar (projectile) velocity of 17 m/s was used in all the experiments. The specimen completely fragmented in uniaxial stress condition (no confinement) when the projectile velocity reached 14 m/s. The capacitor bank was configured to generate trapezoidal pressure pulses with durations of −400 μs and rise times of approximately 10 μs. The axial stress pulse was also trapezoidal, but with a shorter duration of 120 μs. The confining pressure was applied −100 μs before the arrival of the axial loading pulse on the specimen The capacitor bank was charged to 5 kV, which corresponds to a stored energy of 7.5 kJ. Three experiments numbered 93-1, 93-2, and 93-3 were conducted on Macor, with respective confining pressures of 0, 0.5 and 10 MPa. All the experiments were conducted at a nominal axial strain rate of 350 s^{-1}.

The compressive failure strength was defined in Chapter 2 as the stress calculated from the peak of the first compressive pulse recorded at the transmission bar gage. In the actual experiments, however, the signal from the transmission bar strain gage was difficult to resolve due to the high amplitude electro-magnetic noise created by the discharge of the capacitor bank. The electro-magnetic noise ceased to exist approximately 800 μs after the initiation of the discharging. During the time interval when the noise was significant, the transmitted stress pulse was reflected back and forth in the transmission bar. The fifth reflected pulse was the first one that could be clearly recorded by the transmission bar strain gage without noise. The peak value of this reflected pulse was calibrated to the peak value of the original transmitted pulse by an experiment without the capacitor bank discharge.

Failure strengths are listed in Table 4.1 for the three experiments. From Table 4.1, it is clearly seen that the failure strength increased from 530 MPa to 630 MPa for a confining pressure of about 10 MPa and a strain rate of 350 s^{-1}.

Table 4.1. Experimental Conditions and Failure Strength of Macor.

Experiment	Projectile velocity	Confinement	Failure Strength
93-1	16.26 m/s	0	530 MPa
93-2	15.21 m/s	~ 0.5 MPa	565 MPa
93-3	16.91 m/s	~ 10 MPa	630 MPa

The recovered specimens are shown in Fig. 4.5. Even though it was loaded only once by the modified SHPB, the specimen without confinement was completely fragmented. In the experiment with a confinement pressure of 0.5 MPa, the specimen was also fragmented, but as can be seen from the crack density on the end face in Fig. 4.5, the fragment sizes were larger compared to the unconfined specimen. The recovered specimen from the experiment with confinement of approximately 10 MPa had only a few cracks visible the impact face. The axial stress on this specimen was also the largest among the three experiments. The confinement pressure apparently reduced the tendency for crack initiation and growth, thereby suppressing the axial splitting which would result in fragmentation.

4.2.3 Possible Improvements

The current experimental technique of applying electro-magnetic confinement needs three major improvements before it can be used to do extensive experimental research on engineering ceramics. First, during the discharge of the capacitor bank, the electro-magnetic noise obscured signals obtained from the strain gages mounted on the bars. Since the steel Hopkinson bars are excellent magnetic conductors and are aligned perfectly along the direction of maximum flux of the magnetic field, the strain gages mounted on the Hopkinson bar surfaces inevitably picked up the high amplitude noise signal. **A** Hopkinson bar made of titanium, which is not a magnetic conductor, may reduce the magnitude of the noise, but apparently will not eliminate it completely because the bar strain gages are still located in the magnetic field. Fiber optic strain gages, which are not affected by eletro-magnetic field, may be the best approach for eliminating the noise from the strain gage signals. Second, since the lateral surface of the specimen has been used to place the confinement coils, strain gages could not be mounted on specimens directly. The reflected pulse, if it can be detected by a fiber optic strain gage on the incident bar, is not expected to give detailed information on the deformation behavior of the specimen because, as discussed in Chapter 2, the axial failure strains of the engineering ceramics such as AlN or Al_2O_3 are usually very small. Therefore, new approaches to measure axial and/or lateral strains of the specimen must be developed. Third, the magnitude of the confinement generated by the present experimental setup was too small (compared to the axial load) to perform meaningful experiments on engineering ceramics. There are three approaches for increasing the confinement pressure: (1) increase the energy stored in the capacitor bank; (2) use multi-layer confinement coils similar to the straight coils used by Washabaugh (1990); and (3) use a coil configuration that will maximize the confining pressure.

4.3   Mechanical Confinement

4.3.1 Experimental setup

For the mechanical confinement experiments, the dynamic axial loading device used was once again the modified splitting Hopkinson pressure bar with single loading capability as described in Chapter 2. Tungsten carbide (WC) platens were placed in between the specimen and the bars to prevent the harder specimen from indenting the bar end faces as described in Chapter 3. The WC platens were confined by metal sleeves in the experiments with confined aluminum nitride (AlN) specimens. Without such confinement, the WC platens fail prior to the specimens. The broken fragments of the platens may cause severe stress concentrations on both the specimen and the bar end faces, leading to the premature failure of the specimen and to the damage of the bar end faces. The platens were confined laterally by a shrink fit 303 stainless steel sleeve with an estimated lateral compressive stress (confining pressure) of 210 MPa. In addition, the end faces of the confined WC platens were polished to a 1 μm diamond finish to remove any surface damage. The platens prepared in this way performed without failure, provided they were not used more than once.

The confinement pressure on the specimen was achieved by installing a shrink fit metal sleeve on the lateral surface of the cylindrical ceramic specimen as shown in Fig. 4.6. The inside diameter of the sleeve was slightly smaller than the specimen diameter. To fit the sleeve around the specimen, the sleeve was heated such that the inside diameter was slightly larger than the specimen diameter, at which point the specimen was slid into the sleeve. After the assembly was cooled, shrinkage of the sleeve provided confinement pressure on the lateral surface of the specimen. The confining pressure produced by the sleeve can be estimated by solving an axi-symmetric boundary value problem on the cross-

section of a circular elastic (E_1, v_1) rod (specimen) inside an elastic-perfectly plastic $(E_2,$ $v_2, \sigma_y)$ hollow cylinder (sleeve) with a misfit at the interface. The resulting expressions are:

$$\frac{(1-2v_2)(1+v_2)}{E_2}\sigma_y[r_1\ln r_1 - (2\ln\rho+1-\frac{\rho^2}{r_2^2})\frac{r_1}{2}] + \frac{(1-v_2^2)}{E_2}\sigma_y\frac{\rho^2}{r_1} +$$
$$+ \frac{(1-v_1)}{E_1}r_1\sigma_y[\ln\frac{\rho}{r_1} + \frac{1}{2}(1-\frac{\rho^2}{r_2^2})] = \frac{\delta}{2} \tag{4.2a}$$

$$p = \sigma_y[\ln\frac{\rho}{r_1} + \frac{1}{2}(1-\frac{\rho^2}{r_2^2})] \tag{4.2b}$$

where p is confining pressure on the lateral surface of the specimen, σ_y is the quasi-static yield stress of the sleeve material, r, is specimen radius, r, is the outer radius of the sleeve, δ is the misfit between the specimen diameter and the sleeve inner diameter, and p is the elastic-plastic boundary radius in the sleeve cross section. E and v are the Young's modulus and the Poisson's ratio, respectively. The misfit 8 can be calculated using the thermal properties of the sleeve material. The confining pressure p can be calculated directly by eliminating ρ from equations (4.2a) and (4.2b). The magnitude of the confining pressure is varied by using different materials and thickness for the sleeves. The yield strengths, σ_y, were experimentally measured for the sleeve materials which had been subjected to the same heating and cooling cycle as in the assembly of the confined specimens. This was done in order to eliminate any uncertainties associated with changes in material properties associated with the thermal cycling during specimen assembly. In the case of thin walled sleeves when the thickness of the sleeve (t) is much smaller than the specimen radius (r,), the confining pressure p can be approximated by

$$p = \frac{\sigma_y t}{r_1} \qquad\qquad (4.3)$$

This technique is advantageous since the sleeves are easy to fabricated and no further modifications to the SHPB are required. Also, the plastically deformed sleeve retains the tested specimen allowing examination of the failure mode, even though the brittle specimen itself may have fragmented during the loading. The specimen/sleeve assembly can also be axially loaded in any quasi-static loading frames. With the addition of the confining metal sleeve on the specimen in the dynamic experiments, the following formula should be used to calculate the axial stress in the ceramic specimen from the SHPB transmitted signal:

$$\sigma(t) = \frac{A_0}{A_s} E(\varepsilon_t(t) - \varepsilon_{tc}(t)) \qquad\qquad (4.4)$$

where A_s is the cross-sectional area of the specimen, A_n is the cross-sectional area of the bar of Young's modulus E. $\varepsilon_t(t)$ is the transmitted signal from the experiment with the confined specimen, and $\varepsilon_{tc}(t)$ is the transmitted signal from a test performed on only the sleeve without the specimen after the experiment with the confined specimen. Since the stress state in the sleeve without the specimen is different from the stress state of the sleeve with the specimen, the stress estimated using this approach is an approximation of the actual stress in the specimen. However, the difference in sleeve stress states is not expected to seriously affect the determination of the failure strength since the sleeve material deforms plastically at the strain level where failure strength is measured. On the other hand, the material properties measured at small strains, such as the Young's modulus of the confined specimen, are not considered to be reliable.

The AlN specimens were typically 4.76 mm in diameter and 5.48 mm in length. The AlN specimens were ground cylindrical to within 0.0025 mm on the lateral surface with the two end faces parallel to within 0.0025 mm. The sleeves were fabricated from

copper, brass, carbon steel and 303 stainless steel Chapter 5 gives the detailed specifications of these sleeve materials. The sleeves had the same length as the specimens, and an outer diameter of 8.17 mm. The inner diameter of the sleeves was 0.025 mm less than the specimen diameter on average (i.e., δ=0.025 mm, see Fig. 4.6). Theoretically, the value of δ could be varied accurately to control the magnitude of the confinement pressure by the desired amount of elastic strain in the sleeve. However, it is very difficult to machine the inner diameter of the sleeves to within the necessary tolerance. Therefore, the amount of misfit was chosen such that the sleeve material near its inner diameter would deform plastically when the sleeve/specimen assembly was cooled. The magnitude of the confinement pressure was varied by changing the sleeve material. To assemble the sleeves and the specimens, the copper and brass sleeves were heated to a temperature of − 450 ° C, whereas the steel sleeves were heated to − 850 °C for 40 seconds. After the sleeve was installed on the specimen, the end surfaces of the assembly were polished to a 1 μm surface finish using diamond paste to remove any surface damage from grinding and sleeve installation. On each specimen/sleeve assembly, an axial strain gage was mounted on the outer surface of the sleeve to record the strain in the specimen during loading. Olsson and Forrestal (1994) have used a thin-walled confining sleeve design in their investigation of the effect of confinement on the failure behavior of concrete.

4.3.2 Results

Two sets of experiments were performed at different strain rates. The quasi-static experiments were performed on a servo-hydraulic Material Test System load frame at a strain rate of 4×10^{-4} s^{-1}. The dynamic strain rate using the SHPB was nominally 5×10^{2} s^{-1}. Each group of specimens consisted of five different confining pressures: 0, 55, 120, 153, and 230 MPa which were achieved with no sleeve, a copper sleeve, a brass

sleeve, a carbon steel sleeve, and a 303 stainless steel sleeve, respectively. Detailed specifications of the sleeve materials are given in Chapter 5.

Figure 4.7 is a plot of compressive failure strength versus confinement pressure at two different strain rates. As the lateral confining pressure increased from 0 to 230 MPa, the quasi-static failure strength increased from 2.5 GPa to 3.7 GPa, whereas the dynamic compressive strength increased from 4.3 GPa to 5.4 GPa. The increase in the dynamic failure strength from the static compressive strength is indicative of the strain rate effect. It is interesting to note that the effect of strain rate on the increase in failure strength appears to be independent of the amount of confinement.

Figure 4.8 shows schematic views of the end faces and axial cross-sections of the recovered AlN specimens after being tested dynamically using the SHPB. Schematic drawings are presented because the low contrast of the photographs made it difficult to delineate the details of the damage. The specimen from the experiment with no confinement was completely powdered as shown in Fig. 4.8, even though it was loaded with a single pulse using the SHPB. As the confinement pressure was increased, the crack density decreased as can be observed in the cross-sectional views in Fig. 4.8. In all the confined specimens recovered, a cone shaped surface divides the specimen into two regions. Inside the cone, the crack density was very low, whereas the material outside the cone was cracked extensively, with the crack density decreasing as the confining pressure increased. However, on the surface of the cone, the localized crack density is very high which indicates that the conical surface is a fault formed by the localized deformation and damage that occurred during loading.

4.4   Conclusions

Two experimental techniques have been developed for imposing controlled lateral confinement on specimens subjected to dynamic uniaxial compression.   The axial compression was applied using the split Hopkinson pressure bar modified to apply a single loading pulse. The cylindrical specimens were confined laterally either by eletro-magnetic force, or by a shrink fit metal sleeve.

In the experiments using electro-magnetic confinement, the applied multiaxial loading pulses can be either proportional or non-proportional. During an experiment, the specimen is subjected to known loading pulses in both the axial and lateral directions. Experiments on Macor showed that even for a very low confining pressure of approximately 10 MPa, there was an apparent increase in compressive failure strength. Inspection of recovered specimens showed that the failure mode changed considerably, from complete fragmentation to very low visible crack density on the surface of the specimen.   However, the current experimental technique of applying electro-magnetic confinement needs major improvements in terms of noise reduction, strain measurement and an increase in confinement pressure, before it can be used to do extensive experimental research on engineering ceramics.

During an experiment with a sleeve confined specimen, the specimen is also subjected to a single, known loading pulse. The failure mode can thus be characterized in the recovered specimen. The experiments indicated that for moderate confining pressures *(55-230* MPa), the compressive failure strength of sintered AlN increases with increasing confining pressure under both quasi-static and dynamic loading conditions. Recovered specimens show that the failure mode changes from complete fragmentation by axial splitting when unconfined to localized deformation on faults in the presence of lateral

confinement. This technique is capable of applying relatively high confinement on the specimen as well as retaining the tested specimen for failure mode characterization. Therefore, it was used exclusively in the extensive experimental investigation of the mechanical behavior of Macor and aluminum nitride under multiaxial compression which will be described in the next Chapter.

4.5 References

Arrowood, R., and Lankford, J., (1987), "Compressive Fracture Processes in an Alumina-Glass Composite," Journal of Materials Science, 22, pp. 3737-3744.

Ashby, M. F. and Sammis, C. G., (1990), "The Damage Mechanics of Brittle Solids in Compression," Pure and Applied Geophysics, 133, pp. 489-521.

Grady, D. E., (1995), "Dynamic Properties of Ceramic Materials," Sandia Report SAND94-3266, Sandia National Laboratories, Albuquerque, NM.

Heard, H. C. and Cline, C. F., (1980), "Mechanical Behavior of Polycrystalline BeO, Al_2O_3 and AlN at High Pressure," Journal of Materials Science, 15, pp. 1889-1897.

Horii, H. and Nemat-Nasser, S., (1986), "Brittle Failure in Compression: Splitting, Faulting and Ductile-Brittle Transition," Phil. Trans. Roy. *Soc.* London, 319, pp. 337-374.

Lankford, J., (1977), "Compressive Strength and Microplasticity in Polycrystalline Alumina," Journal of Materials Science, 12, pp. 791-796.

Olsson, W. A. and Forrestal, M. J., (1994), Sandia National Laboratories, Albuqurque, NM, work in progress.

Raiser, G. and Clifton, R. J., (1993), "High-Strain Rate Deformation and Damage in Ceramic Materials," Journal of Engineering Materials, 115, pp. 292-299.

Ravi-Chandar, K. and Knauss, W. G., (1984), *"An* experimental investigation into dynamic fracture, 1. Crack initiation and arrest," *International Journal of Fracture, 25,* pp. 247-262.

Ravichandran, G., and Chen, W., (1991), "Dynamic Failure of Brittle Materials under Uniaxial Compression," in *Experiments in Micromechanics of Failure Resistant Materials.,* edited *by* Kim, K.-S., AMD 130, ASME, New York, pp. *85-90.*

Washabaugh, P. D., (1990), "An Experimental Investigation of Mode-I Crack-Tip Deformation", Ph.D. Thesis, California Institute of Technology.

Figure 4.1 A schematic illustration of the experimental setup for dynamic multiaxial compression using electro-magnetic confinement.
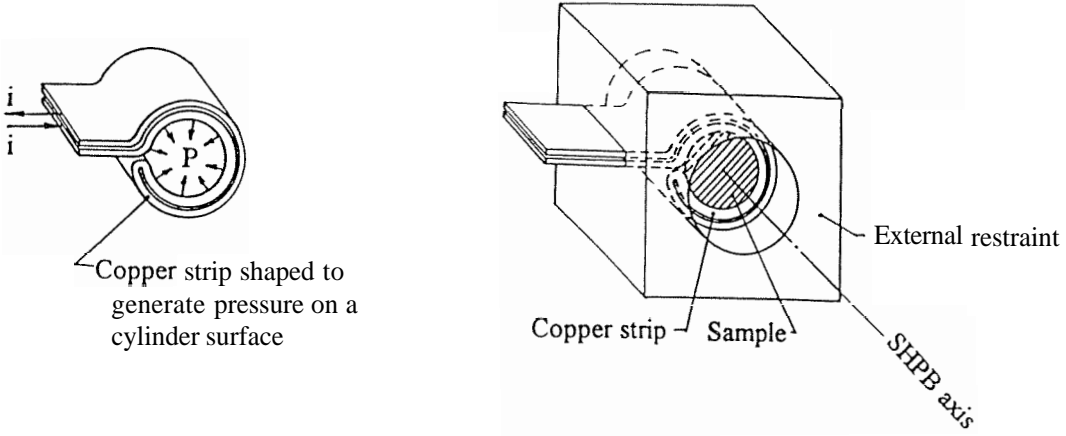
Figure 4.2 A schematic illustration of lateral confinement generated by high intensity current passing through the copper strip.
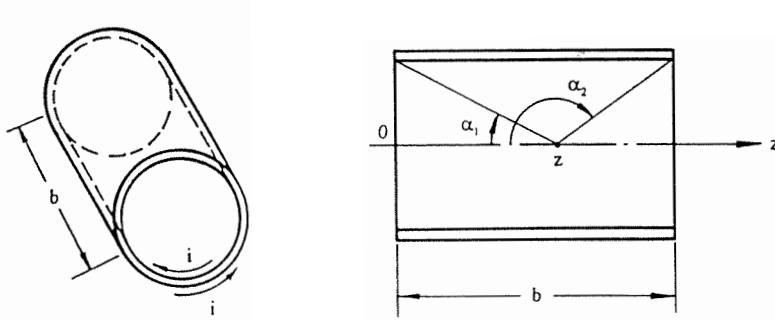
Figure 4.3 Model for confining pressure estimation.
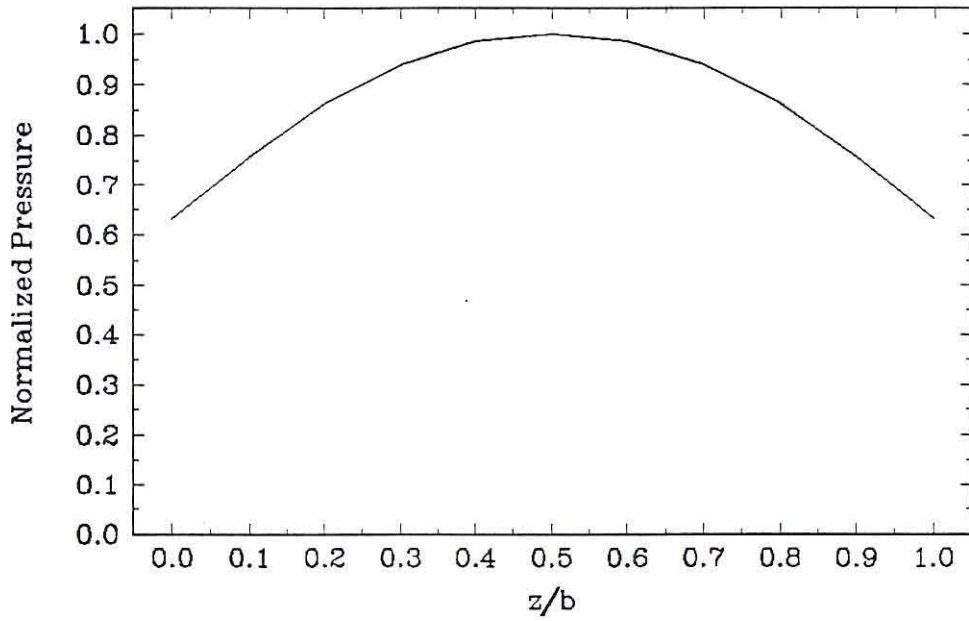
Figure 4.4 Distribution of the Confining pressure along the specimen axis.
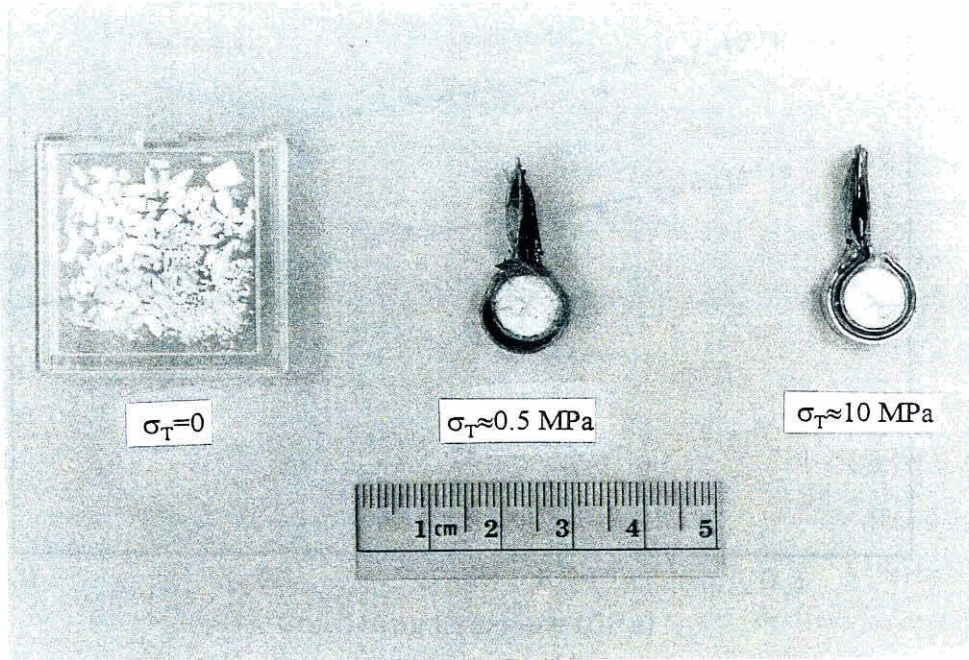
Figure 4.5 Recovered Macor specimens illustrating the effect of lateral confinement on crack density.

Specimen   Sleeve   Assembly

ϕ: specimen
diameter

δ: misfit
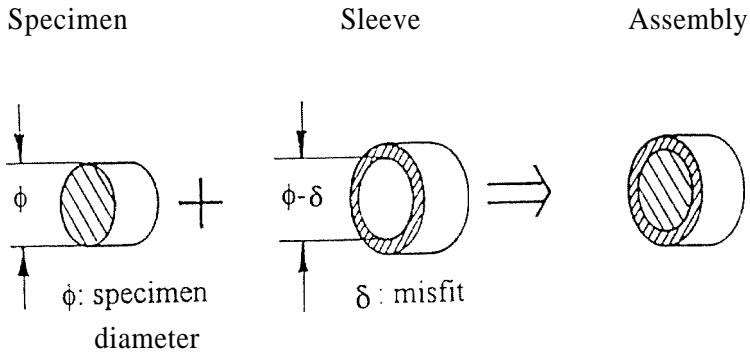
Figure 4.6 A schematic illustration of the shrink-fit metal sleeve used to confine the ceramic specimen.
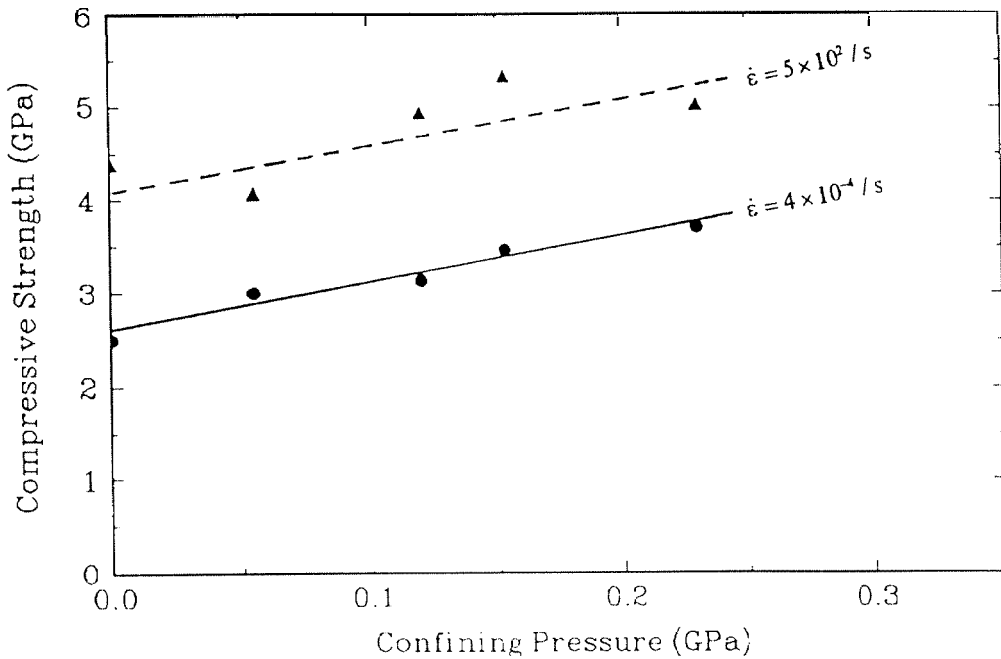
Figure 4.7 Effect of confinement on the compressive failure strength of a sintered aluminum nitride (AlN) at strain rates of 4×10^{-4} s^{-1} and 5×10^{2} s^{-1}.

Top View			
Cross-Section			
Bottom View			
Confinement	0 MPa	50 MPa	230 MPa
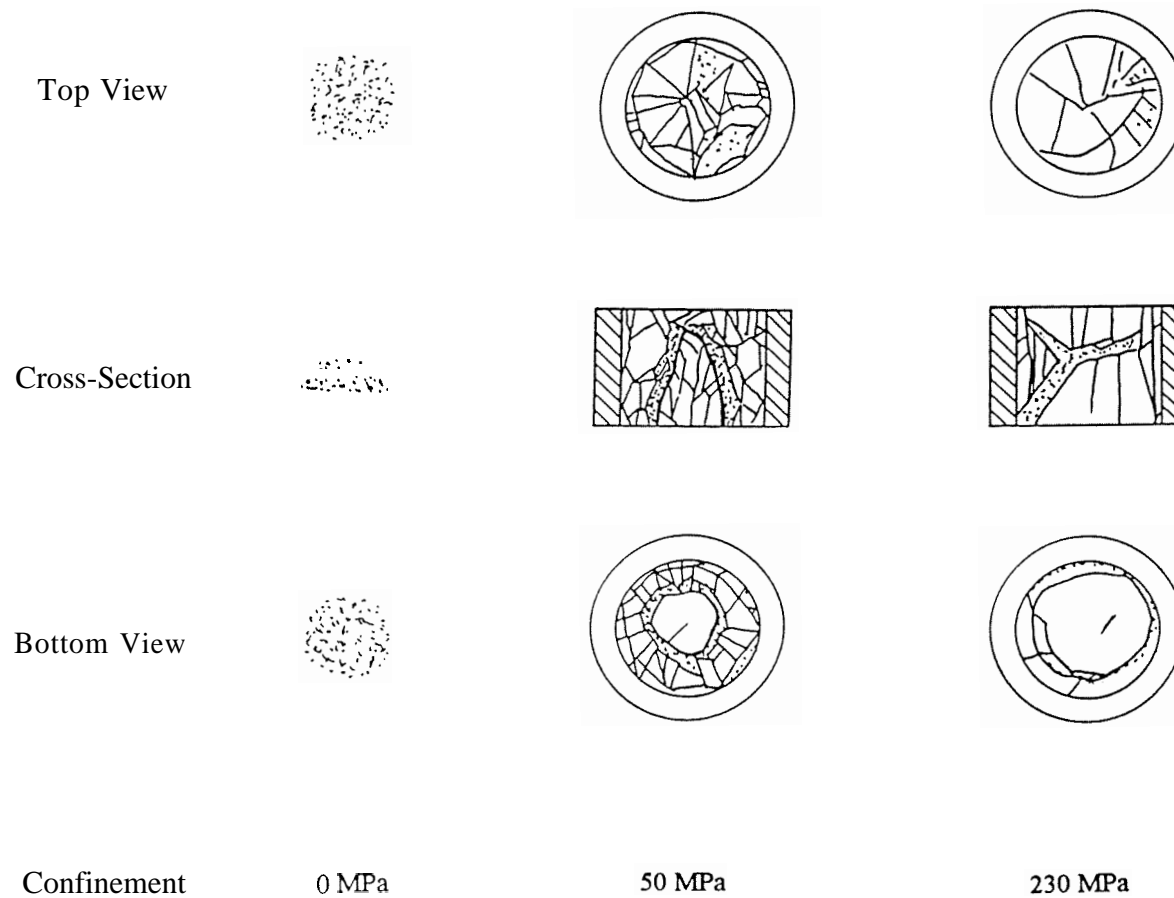
Figure 4.8 Portraits of the recovered AlN specimens from SHPB tests at varying confining pressures.

Chapter 5

Static and Dynamic Compressive Behavior of Ceramics Under Mechanical Confinement

Abstract

Quasi-static and dynamic multiaxial compression experiments have been performed on a machinable glass ceramic, Macor, and a monolithic engineering ceramic, sintered aluminum nitride (AIN). The cylindrical ceramic specimens were confined laterally by shrink-fit sleeves; the amount of confining pressure was varied by using different sleeve materials. The quasi-static axial load was applied by a hydraulic driven Materials Test System (MTS), whereas the dynamic axial load was provided by a split Hopkinson pressure bar (SHPB) modified to load the specimen by a well defined, single loading pulse. For both materials under both quasi-static and dynamic loading conditions, the experimental results showed that the failure mode changed from fragmentation by axial splitting under conditions of uniaxial stress to localized deformation on faults under moderate lateral confinement. The fault initiation process was studied experimentally in detail under moderate confinement. The compressive failure strengths of both materials increased with increasing confinement pressure under both quasi-static and dynamic loading conditions. The effect of strain rate on the failure strength appears to be independent of the confinement pressure. Based on the experimental results, a compressive failure mechanism was proposed for brittle materials under moderate lateral confinement. A transition from brittle to ductile behavior was observed in Macor under high confinement which was achieved using a second sleeve around the inner sleeve.

5.1   Introduction

The dynamic multiaxial compression techniques were introduced in Chapter 4. From the feasibility-proof experiments conducted using these techniques, the mechanical confinement technique, which employs a shrink-fit metal sleeve installed on the lateral surface of a cylindrical specimen was found to be advantageous in applying high pressure and preserving the failure mode for post-test observation. In this chapter, the technique was used to investigate the failure behavior of a machinable glass ceramic, Macor, and a monolithic engineering ceramic, sintered aluminum nitride (AlN) under quasi-static and dynamic multiaxial compressive loading conditions.   The quasi-static axial load was applied by a hydraulic driven Material Test System (MTS), whereas the dynamic axial load was provided by a split Hopkinson pressure bar (SHPB). The SHPB was modified to load the specimen by a well defined, single loading pulse as described in Chapter 2.

In this chapter, the quasi-static and dynamic mechanical behavior and characterization of failure of Macor under moderate confinement are presented in Section 5.2. It was found that a second, concentric shrink-fit sleeve was necessary in order the keep high amplitude confinement pressure on the specimen during axial loading.   The double sleeve concept and the preliminary experimental results using this technique are presented in Section 5.3. In Sections 5.4, the experimental investigation and results of the compressive behavior of a sintered aluminum nitride under quasi-static and dynamic axial loading conditions and mechanical confinement are described. Based on the experimental results, a compressive failure mechanism is proposed for brittle materials under moderate amount of confinement in Section 5.5. Section 5.6 presents a brief summary of the experimental results and observations.

5.2   Failure Behavior of Macor

5.2.1 Specimen

The cylindrical Macor specimens were confined laterally by shrink-fit sleeves. In order to investigate the influence of confining pressure on compressive failure strength and failure mode, 5 different sleeve materials were used to apply varying amounts of confining pressure. The sleeve materials and their quasi-static yield strengths are listed in Table 5.1. The quasi-static yield strengths in Table 5.1 were measured by mechanical tests with the sleeve materials which had been heated and cooled under the same conditions as for the sleeve/specimen assembly process described in Chapter 4.

Table 5.1. Sleeve materials and confinement pressure estimation.

Sleeve Material	Yield Stress, MPa	Confining Pressure, MPa
PMMA	55	10
Al-6061-T6	144	26
Brass*	261	47
Al-2024-T3	277	50
Stainless Steel 303	488	88

*Free cutting brass rod (S.A.E. Standard No. 72)

When the hoop-stress reaches the yield strength of the sleeve material, the lateral confinement pressure applied to the specimen by the thin-walled sleeve is determined by the following expression (see Chapter 4):

$$p = \frac{\sigma_y t}{r} \qquad\qquad (5.1)$$

where p is confining pressure on the lateral surface of the specimen, σ_y is the quasi-static yield stress of the sleeve material, t is the sleeve wall thickness, and r is the specimen radius. As shown in Table 5.1, proper choice of the sleeve material determines the amount of confining pressure. The mismatch between the sleeve inside diameter and the specimen diameter was chosen to be at least 0.025 mm. For this mismatch, the hoop stress in the sleeve always reaches the yield strength of the sleeve material, and Eqn. (5.1) is a good approximation of the lateral confinement.

The Macor specimens used in this investigation were 8.10 mm in diameter and 8.25 mm in average length. The sleeves had the same length as the specimens, with an average wall thickness of 0.73 mm. Thin-walled sleeves were utilized in the investigation of the failure mode transition of Macor since it had been observed that low confinement pressures were sufficient to suppress the uniaxial stress failure mode of axial splitting. The thin-walled sleeve were also able to retain the tested specimen for careful post-test investigation of the failure mode. The exact radial dimensions of the specimens and the sleeves were measured to within ±0.001 mm using an optical microscope. The accuracy of the measurement was critical to appropriately pair the specimens and sleeves for desired amount of mismatch in diameter.

The sleeves were installed on the Macor specimens using the process described in Chapter 4. The end faces of the confined specimens were ground flat and parallel within 0.01 mm, and further polished to a 1 μm finish by using diamond paste to remove any surface damage. On each specimen/sleeve assembly, an axial strain gage was mounted on the outer surface of the sleeve to record the actual strain in the specimen during loading.

5.2.2 Experimental Setup

The experimental setup to perform dynamic experiments was described in detail in Chapter 4. The modified split Hopkinson pressure bar with single loading capability was used to apply dynamic compressive axial loading on the confined specimen. The Macor specimen confined by the shrink fit sleeve was placed between the incident and transmission bars. A test of only the sleeve was performed on the same SHPB facility under the same experimental conditions as described in detail in Chapter 4. The sleeve-only experiments were necessary for determining the axial stress in the specimen using the transmission bar signal and Eqn. (4.4).

A schematic illustration of the quasi-static experimental setup is shown in Fig. 5.1. A hydraulically driven Materials Test System (MTS) was used to apply an axial compressive load on the cylindrical ceramic specimen laterally confined by a shrink-fit sleeve. In experiments involving brittle specimens, the alignment of the loading grip is extremely important if stress concentrations in the specimen caused by uneven loading are to be avoided. These stress concentrations may cause the specimen to fail prematurely by chipping, for example. In order to apply a uniform axial load on the ceramic specimen, a special loading frame was used in the experiments as illustrated in Fig. 5.1. Two 19 mm diameter C-350 maraging steel rods were aligned on the same axis by a pair of linear bearings mounted on an aluminum frame. The end faces of the rods were machined flat and perpendicular to the axis so that the end faces of the rods were parallel to each other. A pair of tungsten carbide (WC) platens were placed between the specimen and the rods to prevent the harder specimen from indenting the end faces of the softer rods. The aluminum frame, which housed the linear bearings, the C-350 rods, the WC platens and the confined specimen, was then placed between the compressive loading platens of the MTS as shown in Fig. 5.1. A ball-bearing joint located in the upper grip of the MTS

ensured the elimination of any bending moment acting on the **C-350** rods. **A** load cell (MTS axial-torsional load transducer, model 662.10A-08) in the crosshead recorded the axial load data. The MTS also was equipped with a linear variable differential transformer **(LVDT)** to monitor the displacement of the hydraulically driven actuator. Since the ceramic specimen length was small and the failure strains were also small, the data collected with the **LVDT** were not considered to be accurate enough to give reliable axial strain information   The axial strain gage mounted on the outer surface of the confining sleeve was used to accurately monitor the axial deformation of the specimen. Furthermore, a high sensitivity **LVDT** was mounted near the ends of the rods across the specimen and the WC platens to continuously monitor the deformation of the specimen as shown in Fig. 5.1 in case the strain gage failed or became unreliable at large strains. The MTS actuator moved at a constant velocity in the displacement control mode during the experiments. Varying strain rates were obtained by varying the actuator velocity through the MTS controller. The load, axial strain signals from the strain gage and the high sensitivity **LVDT** were recorded using a 4-channel digital oscilloscope Nicolet 440.

Since the specimen assembly consisted of the ceramic specimen and the confining sleeve, the total axial loading data measured by the load cell contained the contributions from both components of the confined specimen. In order to obtain the axial stress data from the ceramic specimen, a sleeve-only test was performed immediately after each experiment with identical experimental parameters. The axial stress **a** in the ceramic specimen was computed using the equation:

$$\sigma = \frac{F_T - F_c}{A_s} \tag{5.2}$$

where F_T and F_c are the axial load measured by the load cell in experiments with the confined specimen and with the sleeve only, respectively; and A_s is the cross-sectional area of the ceramic specimen. This is analogous to Eqn. (4.4) of Chapter 4 for the dynamic experiments.

5.2.3 Results

5.2.3.1   Quasi-Static Experimental Results

Macor specimens with various lateral confining pressures were tested quasi-statically on the MTS. Specimens were confined by shrink-fit sleeves of the five different materials listed in Table 5.1. **A** duration of 120 seconds was selected for each experiment. Figures 5.2, 5.3 and 5.4 display the axial load, axial strain from the specimen strain gage and axial displacement from the LVDT as functions of time recorded during the quasi-static experiments conducted on three different specimens. Figure 5.2 shows the profiles recorded in the experiment with an unconfined specimen, which are typical of a uniaxial stress compression experiment with brittle materials. When the specimen was loaded axially starting at t=30 seconds in Fig. 5.2, its axial deformation was detected by both the strain gage and the LVDT. The axial compressive deformation increased with increasing axial load until the uniaxial compressive strength was reached, indicated by the load cell suddenly reading zero at t=58 seconds. At the same time, the axial deformation signals exceeded the detection limits of both the strain gage and the LVDT, which indicates catastrophic failure. The sudden increase in the LVDT signal at failure indicates that the elastic deformation of the loading grips is suddenly relaxed when the specimen collapses. Figure 5.3 shows similar profiles for the specimen confined by a brass sleeve with confinement pressure $\sigma_T = 47\,\mathrm{MPa}$. Comparison of Figs. 5.2 and 5.3 reveals that the

profiles are similar before the peak load was reached. When the peak load was reached at t=67 seconds, the load carrying capability of the specimen also dropped suddenly; whereas the axial compressive strain increased suddenly. Unlike the uniaxial stress case, the specimen did not lose the loading carrying capability completely at its peak strength. Instead, after the discontinuity and as the axial was further increased, the specimen was able to carry a nearly constant axial load. Although the strain gage signal indicates that the strain gage was no longer properly bonded after the discontinuity, the measure in axial compressive strain was realized by the LVDT signal. As the lateral confinement was further increased, the magnitudes of the jumps in axial load and deformation reduced, as shown by the profiles in Fig. 5.4. The specimen in this case was confined by a stainless steel sleeve with an estimated confining pressure of 88 MPa.

5.2.3.1.1   Stress-Strain Behavior

Figure 5.5 shows the stress-strain curves from three experiments on Macor specimens with 0, 47, and 88 MPa lateral confining pressure, respectively. The axial strain was determined from the high sensitivity LVDT output; whereas the axial stress was obtained using Eqn. (5.2). The dash-dot line in Fig. 5.5 is the stress-strain curve from the uniaxial compression (unconfined) experiment. The nearly linear stress-strain behavior prior to failure is typical of brittle materials under quasi-static uniaxial compression. The specimen fails catastrophically at the peak stress, i.e., compressive strength. When lateral confinement was introduced, the change in the stress-strain behavior of the material after peak stress is illustrated clearly in Fig. 5.5. The dotted line represents the stress-strain curve of a specimen with 47 MPa lateral confinement; whereas the solid line is from a specimen with 88 MPa confining pressure. The peak stress, or compressive strength, of the material is seen to increase with lateral confinement. After the peak stress, as the

strain was increased further, as shown by the solid and dotted curves in Fig. 5.5, there was an unstable section in the stress-strain curves for the confined specimens. After the unstable section where load carrying capacity decreased as the strain was increased, the stress-strain curve became nearly horizontal where the load carrying capability was nearly independent of the axial strain. Both the peak strength and the load carrying capacity of the horizontal portion read from the dotted curve are lower than the corresponding values in the solid curve. This is considered to be the effect of confinement pressure.

The apparent tangent modulus of the stable portion of the stress-strain curve also increases with the increase in confinement. However, the change in the modulus is not considered to be a reliable measurement since Eqn. (5.2) was used to obtain the specimen stress: the stress state in the sleeve when tested alone could be different from the stress state when a specimen is contained. If the axial strain is high, the sleeves will deform plastically both with and without the specimen. In this case, the difference in stress states in the sleeve with and without specimen is expected to be small. If the axial strain is low, the sleeve with the specimen may deform plastically since the hoop stress is designed to reach yield strength for the sleeve material near the inside diameter. However, at the same axial strain level, the sleeve in the sleeve-only test may still deform elastically. Therefore, the effect of the stress state difference on the axial stress value is more apparent at small strains where the modulus is determined.

5.2.3.1.2   Effect of Confinement on Compressive Strength

For materials under lateral confinement, the value of axial stress at the peak point on a stress-strain curve is defined as the "compressive strength" of the material. The variation of the compressive strength with the amplitude of lateral confinement is plotted

in Fig. 5.6. The compressive strength increased monotonically from 435 MPa to 485 MPa as the lateral confinement was increased from 0 to 88 MPa.

5.2.3.1.3   Characterization of the Failure Mode

Figure 5.7 shows the top view, the bottom view and the axial cross-sectional view of 4 recovered specimens. The specimens without confinement and with a PMMA confining sleeve fragmented when load reached compressive strength during the experiments. The recovered specimens shown in Fig. 5.7 from left to right, are those confined by a 6061 aluminum sleeve, a brass sleeve, a 2024 aluminum sleeve and a 303 stainless steel sleeve. The advantage of using plastically deformable sleeves to confine the ceramic specimens for failure investigation is clearly illustrated in Fig. 5.7, where the fractured specimens are retained by the sleeves. Inspection of the top and bottom views indicated that the initially circular cross-sections of the specimens became irregular in shape, which implies that the deformation of the specimen was no longer homogeneous after damage initiated. A common feature was observed on all the recovered specimens despite their irregular shapes: in each of the recovered specimens, there was a cone shaped region with its base at one of the flat faces of the specimen. Inside the cone, the crack density was much lower than the crack density outside the cone. The conical surface formed a conically shaped fault. After the fault was formed, further deformation of the specimen was accommodated by relative sliding of the material across the fault. The resistance of the material against the sliding corresponds to the stress level at the nearly horizontal region of the stress-strain curve in Fig. 5.5. Since the resistance to the sliding was much lower than the compressive strength of the material, the fault was expected to form when the compressive strength in the specimen was reached. If the

shape of the conical fault is locally irregular, sliding across the fault could cause the irregular specimen shape.

5.2.3.2   Dynamic Experimental Results

Dynamic experiments were conducted at striker bar velocities of 26 m/s and 37 m/s on the modified split Hopkinson pressure bar. The yield strength and the confinement pressure of each sleeve material are tabulated in Table 5.2. Axial strain gages were mounted on all the specimens to record the axial strain. The strain gage signals from the incident bar, transmission bar, and the specimen were recorded on a high speed Nicolet 440 digital oscilloscope for further data processing. A copper pulse shaper of 3.3 mm in diameter and 0.85 mm thick was placed on the incident bar end facing the striker bar to prevent the specimen from failing before equilibrium was reached in the specimen. The incident, transmitted and specimen strain pulses recorded from a typical experiment are shown in Fig. 5.8. A fixed striker bar length of 100 mm was used, except for the specimen confined by a stainless steel sleeve, for which a 50 mm long striker bar was used.

Table 5.2. Sleeve materials and confinement pressure estimation.

Sleeve Material	Yield Stress, MPa	Confining Pressure, MPa
PMMA	55	10
Nylon	Elastic	15
Copper	122	22
Al-6061-T6	144	26
Brass	261	47
Al-2024-T3	277	50
Stainless Steel 303	488	88

5.2.3.2.1 Stress-Strain Behavior

Figure 5.9 shows typical stress-strain curves for specimens without confinement and with lateral confinement of 47 MPa (brass sleeve in this case). The specimens were tested at a striker bar velocity of 37 m/s. The axial strain was determined from the signal measured by the strain gage on the specimen, whereas the stress was calculated from the transmission bar signals using Eqn (4.4) As shown in Fig. 5.9, the stress-strain relation for the unconfined specimen was nearly linear. The Young's modulus was determined to be 63 GPa which is very close to the value listed in Table 2.1 in Chapter 2. The slope of the stress-strain curve decreased constantly from a stress of $\approx$ 60% of the failure strength until failure. When lateral confinement was applied on the specimen, the stress-strain behavior appeared to be quite different from the behavior in the dynamic, uniaxial stress case. The initial part of the stress-strain curve of the brass sleeved specimen was nearly linear behavior with the modulus being higher than the Young's modulus of the unconfined case as shown in Fig. 5.9. For the reasons discussed in Section 5.2.3.1.1, the value of the modulus at low loading levels is not considered to be a reliable measurement since Eqn. (4.4) was used in the data reduction. After the axial stress reaches about 350 MPa, which corresponds to an axial strain of 0.44%, the tangent modulus decreased to $\approx$ 22 GPa and further decreased as the axial strain increased. Investigation of the strain history shown in Fig 5.10, revealed that after the axial strain reached $\approx$ 0.44%, the strain rate (indicated by the slope of the curve), increased drastically from 200 s^{-1} to 2800 s^{-1}. The shape of the stress-strain curve for the confined specimen appears to be similar to a work-hardening ductile material instead of a brittle ceramic, as illustrated by the stress-strain curve of a confined ceramic specimen under dynamic axial compressive loading shown in Fig. 5.9. With the presence of lateral confinement. the stress-strain behavior of the ceramic material cannot be treated as linear until failure which characterizes most brittle ceramic materials in uniaxial compression experiments. The stress-strain behavior following the peak stress

is not as clear in Fig. 5.9 as compared to the quasi-static behavior due to the failure of the axial strain gage at strains of −3% in the dynamic experiments. The transmission bar signal as shown in Fig 5.8, however, provided information of the variation of the load carrying capacity of the specimen as a function of time. Inspection of the transmitted signal in Fig. 5.8 indicates that the behavior of the confined Macor specimen under dynamic axial loading is similar to the corresponding behavior under quasi-static loading. The peak loading point on the transmitted pulse in Fig. 5.8 corresponds to the stress value at the peak point on the stress-strain curve in Fig. 5.9. After the peak loading, the axial loading carrying capacity of the specimen suddenly drops to a lower stress level, and then remains nearly constant at this level until unloading.

5.2.3.2.2   The Effect of Confinement on Failure Strength

The stress value at the peak point in Fig. 5.9 is defined as the dynamic compressive strength of Macor, σ_F, under given lateral confinement at corresponding strain rate. The variation of compressive strength, σ_F, as a function of lateral confinement, σ_T, is plotted in Fig. 5.11. It is apparent from Fig. 5.11 that the strength increased from 0.45 GPa to approximately 0.73 GPa as the lateral confining pressure was increased from zero to 88 MPa. The effect of striker bar velocity was not apparent, primarily because the velocity difference did not create large enough strain rate differences in the specimens.

5.2.3.2.3   Permanent Axial Strain on the Recovered Specimens

The dimensions of each specimen were measured before and after the dynamic experiment. Table 5.3 lists the permanent axial engineering strain on each recovered

specimen after the experiment. The final length of the nylon sleeved specimen could not be measured accurately after the experiment due to the large elastic recovery of the nylon sleeve. The permanent strain on the stainless steel sleeved specimen was small partly because a 50 mm long striker bar was used in this experiment as mentioned earlier.

Table 5.3 Permanent axial strain (ε^p) on recovered specimens.

Sleeve	V=26 m/s ε^p (%)	V= 37 m/s ε^p (%)
None	Fragmented	Fragmented
PMMA	Fragmented	Fragmented
Nylon	See Text	See Text
Copper	7.08	14.11
Al 6061	7.37	13.12
Brass	5.98	12.80
Al 2024	8.08	14.17
Stainless Steel	N/A	2.10

It is clear that the laterally confined Macor specimen underwent large permanent strain as compared with the failure strain in a uniaxial experiment where Macor would typically fail at axial strains of <1%. In the case of the stainless steel sleeved specimen, there was a cone inside the recovered specimen, but the permanent strain was only 2.1 %, which indicates that the permanent strain was accumulated after the specimen suffered a drop in loading carrying capacity at axial strains of 2-3%. The axial stress remained nearly constant after the drop as the axial strain further increased to accumulate most of the permanent strain. In this region, the specimen behaves similar to a perfectly plastic material. If the axial load was terminated just after the compressive strength was reached in the specimen, the permanent axial strain level would be much lower. This was the case with the stainless steel sleeved specimen listed in Table 5.3, i.e., the majority of the permanent strain was accumulated in the post-failure region.

5.2.3.2.4   Failure Mode Under Dynamic Loading

Figure 5.12 shows the faces of the recovered specimens which were in contact with the incident bar after being loaded dynamically at a striker bar velocity of 37 m/s on the modified SHPB. From left to right, they are the specimens without confinement, with a nylon sleeve, with a copper sleeve, and with a brass sleeve. The specimen from the experiment with no confinement was fragmented completely, even though it was loaded with a single pulse using the modified SHPB under the identical experimental conditions as the confined specimen experiments. With small confinement pressure, as in the case of the nylon sleeve which provided 15 MPa lateral pressure, the specimen was also fragmented, but as shown by the crack density on the surface, the fragment sizes were larger than the fragments in the unconfined specimen. As the confinement pressure was increased to 22 MPa with the copper sleeve, the crack density was reduced further. When the lateral pressure was increased to 47 MPa with the brass sleeve, few cracks could be seen on the surface, even though the permanent axial strain was 12.8% as listed in Table 5.3. Visible crack density on the opposite end face of the specimens (not shown in Fig. 5.12) also decreased as the confinement pressure increased. The propensity for crack growth appeared to be suppressed by the lateral confinement pressure.

On all the recovered specimens, there was a powdered annular region just inside the sleeve where crack density was very high. It was also noticed that the initially circular cross-sections of the specimens became irregularly shaped as shown in Fig. 5.12. As discussed in Section 5.2.3.1.3, this indicates that the deformation of the specimen was not homogeneous after damage initiation. The recovered specimens were cut with a low speed diamond saw to reveal a section parallel to the loading axis. The cone-shaped region was found in each of the recovered specimens, similar to those observed in the

quasi-statically deformed specimens shown in Fig. *5.7*. The cones in the recovered specimens from dynamic experiments were almost right cones: the apex of the cone was located at or very close to the center of the specimen axis. Therefore, the shape of the conical fault in a specimen loaded dynamically was more regular then the cone shape from a quasi-statically loaded specimen. Figure 5.13 is a typical picture of the axial cross section. The specimen from an experiment with no confinement was fragmented completely as shown in Fig. 5.12, even though it was loaded in a manner identical to the confined specimens. In the presence of confinement, the specimens were fragmented with the exception of a conical region with its base at one end of the specimen as shown in Fig. 5.13. Inspection of Fig. 5.13 indicates that the conical surface divides the specimen into two regions: the crack density was very low inside the cone, whereas the material was cracked extensively outside the cone. Typically, the fragment sizes in the region outside the cone were larger than the comminuted fragments of the unconfined specimen. The crack density outside the conical region decreased with increasing confining pressure. Furthermore, a thin annular region of powdered material which was observed on the bottom of the confined specimen where the base of the cone was located indicates a very high local crack density. In fact, the annular region is a cross-section of a layer of ceramic rubble formed on the conical surface, which implies that there was severe sliding motion across the conical fault in the deformation process.

5.2.3.2.5   Formation of the Conical Fault

Conically shaped faults were observed in all the laterally confined specimens recovered from both quasi-static and dynamic experiments. The formation of this fault appears to be the factor which determines the compressive strength and dominates the mechanical behavior of the specimen in the post-failure (i.e., after the compressive

strength is reached) stage of the deformation. Therefore, it is necessary to understand the process of the fault formation along with key parameters associated with the process. The conical fault is believed to form at the peak stress as discussed in Section 5.2.3.1.3. In order to investigate the process of conical fault formation, the axial loading should be terminated at various times just after the peak stress is reached in the specimen. This level of load control cannot be achieved quasi-statically on the MTS since there is elastic strain energy stored in various parts of the load frame. When the specimen exhibits unstable behavior, the stored elastic strain energy in the loading frame is released to the specimen resulting in its fragmentation. Therefore, it is not possible to terminate the experiment at the onset of unstable deformation. However, in the modified split Hopkinson pressure bar, with the single loading feature and the control over the shape, magnitude, and duration of the loading pulse, it is feasible to terminate the axial loading at various stages after the peak, and therefore it is possible to reveal the process of the conical fault formation.

Experiments were conducted on specimens confined by brass and stainless steel sleeves with a 26 mm long striker bar. In order to terminate the axial loading at various stages of the fault formation, it was found that the striker bar velocity should be maintained at approximately 40 m/s for stainless steel sleeved specimens and 36.5 m/s for brass sleeved specimens. An axial strain gage was mounted on the outer surface of the sleeve of each specimen. A copper pulse shaper 3.6 mm in diameter and 0.85 mm in thickness was used in each experiment. Figure 5.14 shows a typical axial strain history in such an experiment, whereas Fig. 5.15 shows the corresponding stress-strain curve. The axial strain began to increase at the arrival of the incident pulse at the specimen. After the peak in the loading pulse, the axial strain in the specimen reduced as the axial load decreased. However, when the specimen was unloaded completely, permanent axial strain remained on the specimen as shown clearly in Fig. 5.15. The recovered specimens were

then cut to reveal a cross-section parallel to the loading axis. Various stages of the conical fault formation process were revealed by inspection of the crack/fault patterns on the cross sections: Fig. 5.16 shows schematic views of three of the cross sections. Since the cracks were very thin just after initiation, it was difficult to identify crack patterns due to the low contrast in the original photographs. Therefore, schematic drawings are presented. The cross section in Fig. 5.16a shows almost no damage in the specimen except two pairs of small cracks initiating from the four corners of the cross section which could be seen clearly under an optical microscope. The cross sectional view in Fig. 5.16b showed that these two pairs of small cracks have propagated from the corners into the specimen, and intersect near the mid-height in the specimen. One pair of the cracks stopped propagating at the intersection, whereas the other pair continued to propagate until intersecting each other to form the conical fault as shown in Fig. 5.16c. No rubble was observed between the just-formed fault surfaces. Inspection of powdered material found in the fault in the specimens recovered from the earlier dynamic experiments (Fig. 5.13) indicated that there was substantial sliding motion across the fault after its formation. The resistance to the sliding motion in the rubble layer apparently does not depend on the relative positions of the opposite sides across the fault. This accounts for the perfectly-plastic-like behavior of the specimen, i.e., constant load carrying capability with increasing deformation.

5.2.3.2.6   Summary of the Dynamic Experimental Results

Under the action of a moderate confining pressure ranging from 0 to 88 MPa, there was an apparent increase in dynamic compressive strength for machinable glass ceramic, Macor. The dynamic compressive strength increased from 0.45 GPa to 0.73 GPa as the lateral confinement was increased from 0 to 88 MPa. The confined specimens demonstrated inelastic (but stable) axial stress-strain behavior at strains of up to 3%.

After the peak stress in the specimen, there was an unstable portion in the stress-strain curve, followed by a nearly horizontal portion where the measured axial stress remained nearly constant as the strain increased further. Careful examination of recovered specimens showed that under confining pressure the failure mode changed considerably from complete fragmentation under the condition of uniaxial stress to localized deformation on faults in specimens under moderate confinement. The conical faults initiated from the corners of the specimens, and penetrated into the specimen. After the formation of the faults, further axial deformation of specimens was accommodated by the sliding motion of the material across the faults.

5.3   Brittle-Ductile Transition Under High Confinement Pressure in Macor

Under axial compressive loading, due to the Poisson's ratio effect, both the ceramic specimen and the metal sleeve expand in the radial direction before the failure of the ceramic specimen. The Poisson's ratios of metals are usually higher than those of ceramic materials. Therefore, the metal sleeve on the specimen will expand more than the specimen in the radial direction. This excessive lateral expansion in sleeve clearly would cause a relaxation in confining pressure. In fact, the lateral confinement is completely released when

$$(\nu_2 - \nu_1)\varepsilon \geq \frac{\sigma_{y2}}{E_2} \tag{5.3}$$

where ν, and ν, are the Poisson's ratios of the sleeve and the specimen materials respectively, ε is the axial strain which is the same for both the specimen and the sleeve during axial loading, and σ_{y2} and E_2 are the yield stress and the Young's modulus of the sleeve material.

In the axial loading process, the lateral confinement provided by the metal sleeve decreases as the axial strain is increased. The axial strain (ε) was found to be approximately 1% for the thin sleeved Macor specimens at the onset of the formation of the conical faults. The fault-onset-strain in the thick sleeved AlN specimens fell in the range of 2 – 3%. The confinement is relaxed most, and Eqn. (5.3) is most likely to be satisfied, when the difference in Poisson's ratio between the sleeve and the specimen materials is the largest, provided the right hand side of Eqn. (5.3) remains relatively constant. The situation will become more serious when the sleeve deforms plastically, and ν_2 approaches 0.5. Since the Poisson's ratios for metals are usually larger than those of ceramics. From Eqn. (5.3), the relaxation in lateral confinement will always be induced by axial compression, which makes it difficult to reach and maintain high confining pressure during the axial loading process. In order to investigate issues such as the brittle/ductile transition in brittle materials, it is desirable to achieve and maintain high confining pressures during the process of axial loading.

A second shrink-fit metal sleeve was introduced to eliminate the confining pressure loss during axial deformation of the confined specimen. As shown in Fig. 5.17, the second sleeve was machined with chamfered ends. Its length was the same as the specimen at its inside diameter and symmetrically decreased radially. The pressure from the shrink fit of the second sleeve maintained the confining pressure on the ceramic specimen generated by the first sleeve. The tapered shape ensured that the second sleeve would not be affected by the axial compression due to the Poisson's ratio effect, at least at small axial strains

such as 1-3 % which are important in the investigation of the transition in failure mode. The axial stress in the ceramic specimen can be estimated by Eqn. (4.4). In this case, the sleeve-only experiments involves the assembled double sleeve without the ceramic specimen in the assembly. The confining pressure on the specimen was estimated using Eqns. (4.2a) and (4.2b). The outer sleeve generated little confinement on the specimen compared to that generated by the inner sleeve, however, it maintained the lateral pressure from the first sleeve during axial loading.

Dynamic experiments were performed on Macor specimens confined by the double sleeves using the modified split Hopkinson pressure bar. The cylindrical Macor specimens were 6.35 mm in diameter and 9.50 mm in average length. The inside diameter of the first sleeve was machined to be 0.025 mm less than the specimen diameter, and the outside diameter was 9.525 mm. The inside diameter of the second sleeve was 9.500 mm with the outside diameter being 15.875 mm. The chamfer on the second sleeve was 30 degrees from the specimen end faces. Two different sleeve materials were used: brass and 303 stainless steel. The two concentric sleeves on one specimen were made of the same material. The specimen preparation procedure was similar to that used for single sleeved specimens described in Chapter 4. Since a tapered second sleeve is used, it was not possible to mount a strain gage on the specimen surface to monitor the axial stain as was done with the single sleeved specimens. If dynamic experiments have to be performed on hard ceramic materials confined by the concentric double sleeves using the SHPB, new techniques must be developed to measure reliably the axial strain during loading. However, Macor is a relatively soft ceramic material as demonstrated by the earlier experimental results, and therefore, it is feasible to use the reflected signal in the incident bar to estimate the axial strain rate in the specimen using Eqn. (2.1).

In the experiments, a 50 mm long maraging steel striker bar of 12.7 mm diameter was used. A copper disc of 3.65 mm diameter and 0.85 mm thickness was used as a pulse shaper to control the rise time of the incident pulse. A striker bar velocity of 40 m/s was used. Figure 5.18 is a plot of the typical incident and transmitted pulses recorded during the experiment. The transmitted signal in the transmission bar was used to estimate the axial stress in the specimen using Eqn. (4.4); and the reflected signal in the incident bar was used to calculate the axial strain rate using Eqn. (2.1). A time integration of the strain rate gave the axial strain.

Figure 5.19 shows two dynamic stress-strain curves for the brass and stainless steel double sleeved specimens. The brass sleeved specimen (σ_T=120 MPa) has similar stress-strain behavior as the specimens confined by the thin-walled sleeves shown in Fig. 5.9. There is a peak in the stress-strain curve, located at an axial strain of 2.5%. Before the peak, the stress-strain behavior was stable, whereas after the peak, the specimen deformed in an unstable manner until the strain reached approximately 6%. As the strain increased further, the axial stress remained nearly constant (– 0.42 GPa) until unloading. The compressive strength obtained from the brass sleeved specimen was approximately 1 GPa. The maximum axial strain reached in the specimen during the experiment was 10 %.

The specimen confined using double stainless steel sleeves (σ_T=230 MPa) behaved differently in comparison to the brass sleeved specimen. During the loading process, the axial strain increased with loading until the strain reached 2%. As the axial strain was increased further from 2%, the axial stress in the specimen remained nearly constant until unloading. There was no apparent unstable portion in the stress-strain curve comparable to that observed in the cases with lower lateral confinement. The specimen exhibited elastic-perfectly plastic like stress-strain behavior when confined by the stainless steel sleeves. The average stress measured from the plateau of the stress-strain curve was

approximately 1.35 GPa. The magnitude of the confining pressure generated by the stainless steel sleeves was 17 % of this plateau stress. The permanent strain measured on the recovered specimen was approximately 2 %.

The recovered specimens were cut to reveal a section parallel to the loading axis. A conical fault was again observed in the brass sleeved specimen, similar to the faults found in the Macor specimens confined by thin-walled sleeves as shown in Figs. 5.7, and 5.13. However, in the cross section of the stainless steel sleeved specimen, no visible cracks were observed under the optical microscope even at the stress concentrated right corners. The observations that the specimen was deformed permanently and no cracks were created during deformation indicate that inelastic deformation must have occurred in the specimen. The occurrence of inelastic behavior was also confirmed by the stress-strain curve shown in Fig. 5.19. Therefore, a brittle-ductile transition occurs in Macor when the lateral confinement is between 120 and 230 MPa. This is the first time a ceramic specimen with permanent deformation and no visible damage has been recovered from a controlled laboratory experiment at room temperature.

The large confinement pressure experiments could also be conducted on the sintered AlN. However, stronger platen material would be needed to keep the specimen end faces flat during the axial loading. Stronger sleeve materials would also be needed to generate enough confinement pressure to investigate the brittle-ductile transition in AlN. Experiments with C350 maraging steel sleeves, with a compressive yield strength of 2.3 GPa, were attempted. However, this material was found to be unacceptable, since the material properties were found to have changed due to annealing during the sleeve/specimen installation process.

5.4   Failure Behavior of Sintered Aluminum Nitride

5.4.1 Specimen

In order to investigate the influence of lateral confining pressure on the quasi-static and dynamic compressive strength and failure mode transition of the sintered aluminum nitride (AlN) specimens, four different sleeve materials were used: copper, brass, high carbon tool steel, and 303 stainless steel. The quasi-static yield strengths of these materials are given in Table 5.4. These values were obtained by performing quasi-static tests on the sleeve materials which had been heated and cooled under the same conditions as in the sleeve/specimen assembly process. Since the strength and stiffness of the AlN are much higher than those of Macor, thick walled sleeves were used in the experiments with AlN specimens to generate moderate confinement with respect to the axial stress. The confining pressure was estimated using Eqns. (4.2a, b). The AlN material used in this investigation was provided by the Dow Chemical Company, Midland, Michigan. The mechanical properties of sintered aluminum nitride as provided by the manufacturer are listed in Table 5.5. The specimens were core-drilled from a quarter inch (6.35 mm) thick AlN plate, and then ground to the specified dimensions and tolerances.

Table 5.4. Sleeve material properties and estimated confinement pressure.

Material	Young's modulus, E_2 (GPa)*	Poisson's ratio, ν_2*	Yield strength, σ_y (MPa)	Confinement pressure (MPa)
Copper	108	0.355	122	55
Brass	110	0.331	261	120
Tool steel	200	0.290	325	153
Stainless steel	190	0.305	488	230

* From ASM (1983) data

Table 5.5. Selected properties of sintered AlN.

Mass Density, ρ	3200 kg/m³
Young's Modulus, E	307-319 GPa
Poisson's Ratio, v	0.237
Quasi-static Unconfined Compressive Strength, σ_c	2.5 GPa**

** From this study

The specimens were typically 4.76 mm in diameter and 5.48 mm in length after grinding. The AlN specimens were ground to be cylindrical within 0.0025 mm on the lateral surface with the two end faces parallel to within 0.0025 mm. The sleeves were the same length as the specimens, with an outer diameter of 8.17 mm. The inner diameter of the sleeves was typically 0.025 mm less than that of the specimen diameter. The copper and brass sleeves were heated to 450 °C, whereas the steel sleeves were heated to 850 °C in a furnace for approximately 40 seconds prior to assembly with the specimens. After the sleeve was installed on the specimen, the end faces of the assembly were polished to a 1 μm finish using diamond paste to remove any surface damage from the grinding and sleeve installation processes. On each specimen/sleeve assembly, an axial strain gage was mounted on the outer surface of the sleeve to measure the strain as a function of time during loading. During quasi-static experiments on the MTS, the load was measured using the MTS load cell, and the axial displacement was measured by the high sensitivity LVDT as shown in Fig. 5.1; both the load and displacement were recorded on a Nicolet 440 digital oscilloscope. In dynamic experiments, the strain gage signals from the incident bar, transmission bar, and the specimen were also recorded using the high speed digital oscilloscope. Confined tungsten carbide platens were placed between the confined specimen and the bars as described in Section 4.3.1.

5.4.2 Results

Two groups of experiments were conducted at different strain rates: the quasi-static experiments were performed on the MTS at a strain rate of 4×10^{-4} s^{-1}, and the dynamic experiments were conducted on the SHPB at a nominal strain rate of 5×10^2 s^{-1}. Specimens were tested at each strain rate with varying amounts of confinement provided by the four different sleeve materials; specimens were also tested without confinement.

5.4.2.1   Constitutive Behavior

Figure 5.20 shows the variation of strain as a function of time for the specimens without confinement and with approximately 150 MPa confining pressure at a strain rate of 4×10^{-4} s^{-1}. The unconfined specimen was powdered at failure at a strain of -1%. It is apparent from Fig. 5.20 that the strain in the confined specimen also increased suddenly at a strain of -1%, but the specimen did not fail catastrophically. Following the finite jump in strain, the strain continued to increase in a stable manner. Similarly, Fig 5.21 shows the variation in strain with time for the specimens without confinement and with a brass sleeve (120 MPa confining pressure) under dynamic axial loading. The strain profiles were recorded by the strain gages mounted on the specimens. The strain in the unconfined specimen increased gradually as a function of time until failure. The average strain rate was computed to be 560 s^{-1}. The confined specimen exhibited two distinct stages of deformation behavior: when the axial strain was below 1%, the specimen deformed at a strain rate of approximately 500 s^{-1}, whereas at strains above 1%, the specimen deformed at a much higher strain rate of approximately 5,500 s^{-1}. The two distinct stages of deformation may be indicative of two independent deformation mechanisms under loading.

Figure 5.22 shows the variation of axial stress as a function of axial strain for the two specimens deformed quasi-statically and whose strain-time curves are shown in Fig. 5.20. The unconfined specimen deformed and failed in a typical brittle manner. The stress-strain curve for the confined specimen may be divided into stable ($\frac{\partial \sigma}{\partial \varepsilon} > 0$) and unstable ($\frac{\partial \sigma}{\partial \varepsilon} < 0$) regions at a transition strain of ⁻ 1% where the stress reached a maximum. After the peak in stress, the material still exhibited appreciable load-carrying capacity. The stable and unstable regions of the stress-strain curve correspond to the deformation before and after the jump shown in Fig. 5.20, respectively. Figure 5.23 shows the stress-strain curves corresponding to the two specimens loaded dynamically using the modified SHPB and whose strain-time curves are shown in Fig. 5.21. The strain values are those from the axial strain gage on the specimen, whereas the stress values were calculated from the transmission bar signals using equation (4.4). As shown in Fig. 5.23, the stress-strain behavior of the unconfined specimen is essentially linear with a Young's modulus of 305 GPa. This value is comparable to the value listed in Table 5.6. The nearly linear constitutive relation is typical for brittle materials under uniaxial compressive stress loading. However, the constitutive behavior of the specimen with lateral confinement was significantly different from that of unconfined specimen. First, similar to the quasi-static experiments, there is a peak on the stress-strain curve defined as the compressive failure strength where the stress value reaches a maximum. At strains below the peak, the stress-strain curve of the brass sleeved specimen was initially linear and the corresponding Young's modulus was slightly higher than that of the unconfined specimen as predicted by the elasticity theory. However, it should be noted that the slope of the initial portion of the stress-strain curve may not be a reliable estimate of the Young's modulus because Eqn. (4.4) was used to obtain axial stress (see Section 5.2.3.1.1). The

slope of the stress-strain curve decreases to zero as the strain approaches the transition strain of 1%   As the stress approaches the peak, the apparent increase in slope (stiffening) after the linear region of the curve may result from the local barreling of the thick walled sleeve.   The apparent axial compressive strain measured with the strain gage on the barreled surface will be less than actual strain corresponding to the change in specimen length.   Therefore, the sudden increase in the slope may not be attributed to the true behavior of the specimen.   After the peak stress, at axial strains exceeding ⁻ 1%, the stress-strain behavior becomes unstable.   The stable and unstable regions of the stress-strain curve correspond to the low and high strain rate deformation behavior discussed previously.

5.4.2.2   Permanent Axial Strain

The dimensions of each specimen were measured before and after the experiment. Table *5.6* lists the permanent axial engineering strain of each recovered specimen tested quasi-statically in the MTS load frame or dynamically in the SHPB.

It is clear from Table *5.6* that the confined ceramic specimens underwent large permanent axial strains, much greater than the failure strains measured in the uniaxial stress experiments.   Sintered AlN typically fails at an axial strain of −1% under uniaxial stress as was demonstrated in the tests on unconfined specimens.   This indicates that the failure mode of the confined specimens may be different from the failure mode observed under uniaxial stress, i.e., fragmentation by axial splitting.

Table 5.6 Permanent axial strain on recovered specimens.

Sleeve Material	Permanent strain, % (from quasi-static tests)	Permanent strain, % (from dynamic tests)
None	Powdered	Powdered
Copper	20.45	19.75
Brass	19.09	8.00
Carbon tool steel	17.29	9.40
Stainless steel 303	15.93	5.70

5.4.2.3   The Effect of Confinement and Strain Rate on Failure Strength

Figure 5.24 is a plot of compressive strength versus confinement pressure at two different strain rates. It is apparent from Fig. 5.24 that the compressive strength increased under both quasi-static and dynamic loading conditions as the lateral confining pressure was increased up to 230 MPa. The quasi-static compressive strength of sintered AlN without confinement was 2.5 GPa, whereas the highest compressive strength obtained with a confinement of 230 MPa was 5.4 GPa. In addition, inspection of Fig. 5.24 indicates that compressive strength increased by approximately 1.5 GPa as the strain rate was increased from 4×10^{-4} to 5×10^{2} s^{-1}. The increase in compressive strength with strain rate appears to be independent of the confining pressure.

Inspection of Fig. 5.24 suggested that the effect of strain rate on failure strength appears to be independent of the confinement pressure. This observation may be rationalized as follows. Under the action of relatively low confining pressure < 230 MPa, the dominant failure mechanism (within the stable region of the stress-strain curve) remains to be the propagation and interaction of microcracks by the action of local tension

since the brittle-ductile transition has not been reached. The propagation of cracks is affected by the strain rate through inertial resistance, the energy release rate, etc. A superposed pressure will elevate the threshold stress level at which cracks start to propagate but is apparently not related to the effects from rate dependent parameters such as inertia and energy release rate. This may explain the apparent independence of confinement pressure and strain rate on failure strength in the relatively low confining pressure region. This may also explain why the failure mode in a dynamically loaded specimen revealed in the next section is similar to the failure mode in a specimen tested quasi-statically. The < 230 MPa pressure corresponds to < 4.3% of failure stress in the case of dynamic loading and < 6.4 % with quasi-static loading, which is below the brittle-ductile transition pressure of 550 MPa for AlN as reported by Heard and Cline (1980) under quasi-static loading

5.4.2.4   Characterization of the Failure Mode

Figure 5.25 shows schematically the views of the end faces and axial cross-sections of the recovered specimens after dynamic testing using the SHPB. Since AlN material is gray in color, it difficult to delineate the details of the damage due to the low contrast of the photographs. Therefore, schematic drawings are presented. From left to right are shown the specimens (a) without confinement, (b) with a copper sleeve ($\sigma_1 = 55\,\text{MPa}$), (c) with a brass sleeve ($\sigma_1 = 120\,\text{MPa}$), (d) with a high carbon tool steel sleeve ($\sigma_1 = 153\,\text{MPa}$) and (e) with a 303 stainless steel sleeve ($\sigma_1 = 230\,\text{MPa}$). Even though it was loaded only once in a manner identical to the confined specimens, the specimen from the experiment with no confinement was comminuted (powdered) completely as shown in Fig. 5.25. In the presence of confinement, the specimens were fragmented with the exception of a small conical region whose base formed on one end of the specimen. The

conical feature is apparent in the cross-sectional views shown in Fig. 5.25. Inspection of Fig. 5.25 indicates that the conical surface divides the specimen into two regions: the crack density is very low inside the cone, whereas the material is cracked extensively outside the cone. Typically, the fragment sizes in the region outside the cone were larger than the comminuted fragments of the unconfined specimen. The crack density outside the conical region decreased and the volume of the cone increased with increasing confining pressure. Furthermore, inspection of the bottom view of the confined specimen (Fig. 5.25) where the base of the cone was located, reveals a thin annular region of powdered material similar to the annular region observed on the recovered Macor specimens. The powdered or comminuted region indicates a very high local crack density. The recovered specimens tested quasi-statically were similar in appearance to those shown in Fig. 5.25. This similarity is analogous to the corresponding results in the experiments with Macor discussed in Sections 5.2.3.1.3 and 5.2.3.2.4.

Figure 5.26(b-d) shows the scanning electron micrographs from the polished axial cross-section of a recovered specimen tested with a 150 MPa confining pressure in the SHPB. The locations of the micrographs are indicated schematically in Fig. 5.26a. Fig. 5.26b shows a micrograph taken inside the conical region; microcracks can be seen along grain boundaries, but the crack density is low. The visible microcrack size varies from 2 μ m to 10 pm. Figure 5.26c is a micrograph from the lower right corner of the specimen. It shows the local crack pattern near where the conical surface may have initiated. The cone shaped fault is clearly visible as an inclined line in the micrograph. A detailed view of the fault at higher magnification is shown in Fig. 5.26d: the thick dark line is the fault. Near the fault, the density of microcracks is very high. The interaction of microcracks formed larger cracks which break the material into fragments much larger than the grain size. Some grains near the cracks were pulled out from the bulk of the material. The sliding and rotation of the fragments and grains along the larger cracks and faults can

accommodate the large deformation of the specimen, as well as absorb substantial energy from the impact loading.

5.4.2.5   Summary of AlN Results

Experiments on sintered aluminum nitride show that for a moderate confining pressure (50-230 MPa), the compressive strength increased with confinement pressure under both quasi-static and dynamic loading conditions. The highest compressive strength of a confined specimen measured in the experiments was 5.4 GPa. Recovered samples show that under confining pressure, the failure mode changes considerably, from complete fragmentation by axial splitting under uniaxial stress, to localized deformation on faults in the presence of lateral confinement. There exists a bifurcation point on the stress-strain curve of the confined specimen which separates the stable, low strain rate, and unstable, high strain rate regions of the stress-strain curve.

5.5   Characterization of the Failure Process

The experimental results obtained on Macor and sintered AlN specimens gave a detailed understanding of the failure behavior of these materials in terms of the strain history, stress-strain behavior and failure modes. This may give considerable insight into the quasi-static and dynamic failure process of engineering ceramics. At the onset of loading, the local tensile stresses were not sufficient to cause the pre-existing microcracks to propagate or nucleate new microcracks, implying that the crack density remains constant. Thus, the stress-strain behavior was essentially linear during the initial stage as shown in Fig. 5.27a. After the load was sufficiently large to cause the initial flaws to

propagate under the action of local tensile stresses, the crack density increased continuously as loading and deformation progressed. This would account for the decrease in the slope of the stress-strain curve until the compressive strength was reached as shown in Fig. 5.27b. Even though the applied principal stresses of different magnitudes were compressive, local tensile stresses developed near inhomogeneties and crack tips within the specimen (Ashby and Sammis, 1990). As the axial stress approached the compressive strength, the crack density in the specimen reached a critical value, where the cracks begin to interact at or near stress concentrations. In the case of the sleeved cylindrical specimen, the highest stress concentrations occurred at the right corners. Therefore, the crack interaction will initiate at the comers to form macroscopic cracks which then penetrate into the specimen as shown in Fig. 5.27c. One pair of the cracks will prevail to form a conical fault within the specimen. The onset of fault formation presumably corresponds to the bifurcation or peak point on the stress-strain curve. After the formation of the fault, the stress-strain behavior became unstable, and the specimen began to deform at a very high strain rate; the sliding of the fragments across the faults became the dominant deformation mechanism in the post failure stage as shown in Fig. 5.27d. In the sliding process, grains located on the opposite surfaces of the fault were deformed and/or pulled out from the bulk material. It is expected that a substantial amount of energy from impact loading will be dissipated during this process.

During the quasi-static loading process, the peak stress in the confined specimen was reached at the time when a discontinuity in displacement occurred. The displacement jump may indicate the fault nucleation within the specimen, after which the specimen becomes unstable as indicated by the stress-strain curve. As in the dynamic case, the sliding among the fragments across the faults also became the dominant deformation mechanism in the post failure stage. In fact, the amount of permanent deformation of the tested specimen was determined primarily by the duration of the loading pulse in the

dynamic case, and by the amount of the MTS load frame cross-head displacement in the quasi-static case.

5.6 Summary of the Experimental Results

Experiments have been conducted on a machinable glass ceramic, Macor, under various lateral confinement pressures and under both quasi-static and dynamic axial loading conditions. The experimental results showed that the compressive strength of Macor increased with the increase in lateral confinement under both quasi-static and dynamic axial loading conditions. When the confining pressure was in the range of 10 to 120 MPa, the confined specimen deformed in a stable manner until the axial stress reached its peak value defined as compressive strength. There was an unstable portion in the stress-strain curve just after achieving the peak stress. The unstable portion was continued by a nearly horizontal region where the stress remained essentially constant as the strain was increased further. Inspection of the recovered specimens showed that under confining pressure in this range, the failure mode changed from complete fragmentation under uniaxial stress to localized deformation on faults. The conical fault initiated from the corners of the specimen, then penetrated into the specimen. After the formation of the fault, further axial deformation of the specimen was accommodated by the sliding motion of the material across the fault. The fault formed at the peak point on the stress-strain curve As the lateral confinement was increased further to 230 MPa, the stress-strain curve of the specimen became similar to that of an elastic-perfectly plastic material No cracks or faults were observed in the recovered specimen despite significant permanent deformation. This behavior indicates that a brittle-ductile transition was observed in Macor at this confinement pressure. The highest dynamic compressive strength of Macor

measured in the experiments was 1.35 GPa, whereas its unconfined dynamic compressive strength was measured to be 0.54 GPa.

Experiments on sintered aluminum nitride showed that for a moderate confining pressure (50-230 MPa), the compressive strength increased with confinement pressure. The highest compressive strength of a confined specimen measured in the experiments was 5.4 GPa. Recovered specimens showed that under confining pressure, the failure mode also changed considerably as in the Macor experiments, from complete fragmentation by axial splitting under uniaxial stress loading to localized deformation on faults. There exists a bifurcation point on the stress-strain curve of the confined specimen which separates the stable, low strain rate, and unstable, high strain rate regions of the curve.

A detailed compressive failure mechanism for brittle materials under moderate confinement has been suggested based on the behavior of Macor and sintered AlN in terms of stress-strain curve, the strain history and the observed failure modes.

5.7 References

American Society for Metals, (1983), <u>ASM Metals Reference Book</u>, 2nd edition, Metals Park, Ohio.

Ashby, M. F. and Sammis, C. G., (1990), "The Damage Mechanics of Brittle Solids in Compression," PAGEOPH, **133**, (3), pp. 489-521.

Heard, H. C. and Cline, C. F., (1980), "Mechanical Behavior of Polycrystalline BeO, Al_2O_3 and AlN at High Pressure," Journal of Materials Science, **15**, pp. 1889-1897.

MTS Frame

Upper Grip

C-350 Rod

Linear Bearing

Wheatstone Bridge — Strain Signal

Oscilloscope

Confined Specimen

WC Platen

LVDT

LVDT Circuitry

LVDT Signal

Lower Grip

MTS Actuator

Load Signal

MTS Controller
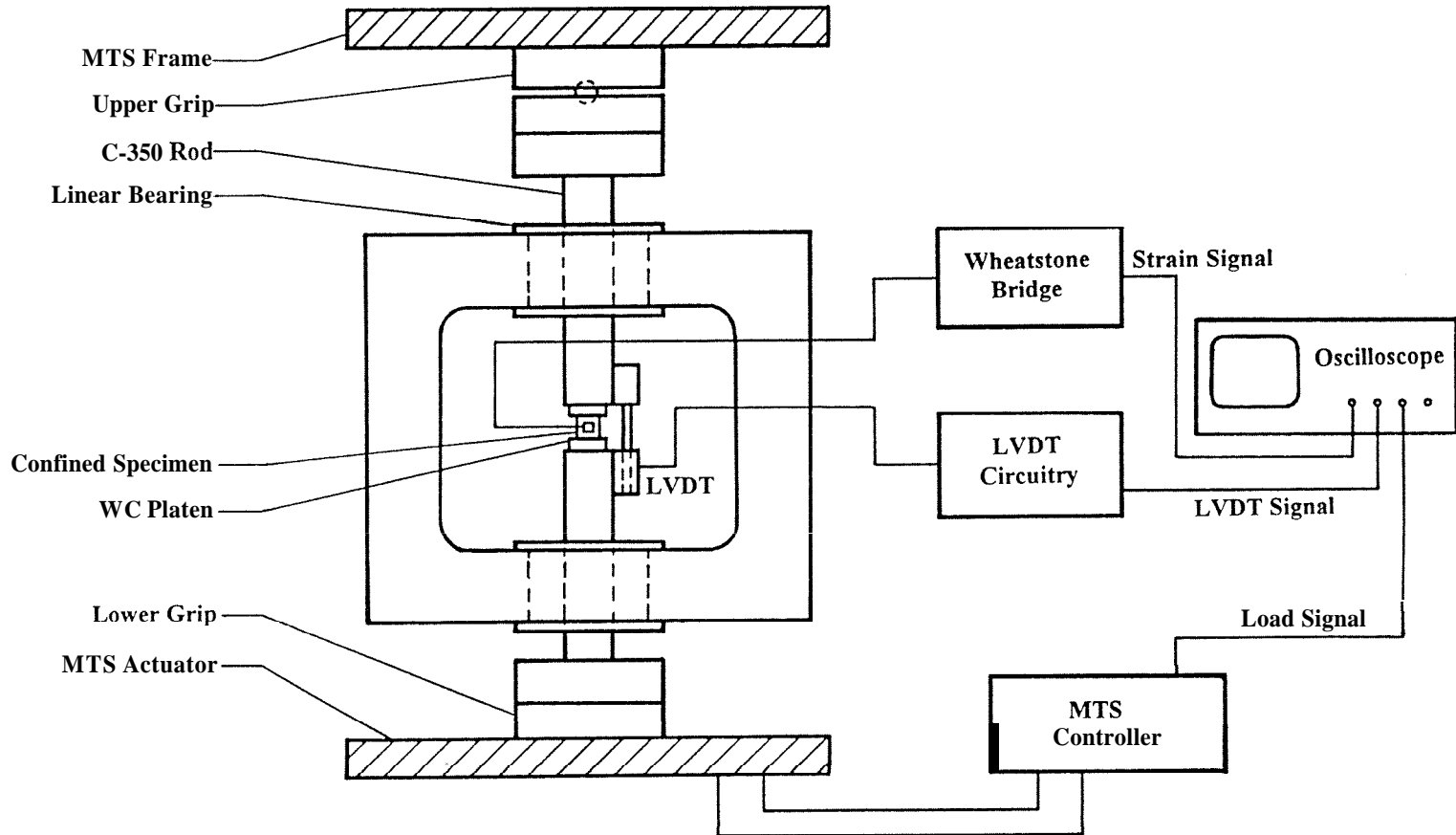
Figure 5.1 A schematic illustration of the experimental setup for quasi-static multiaxial compression.
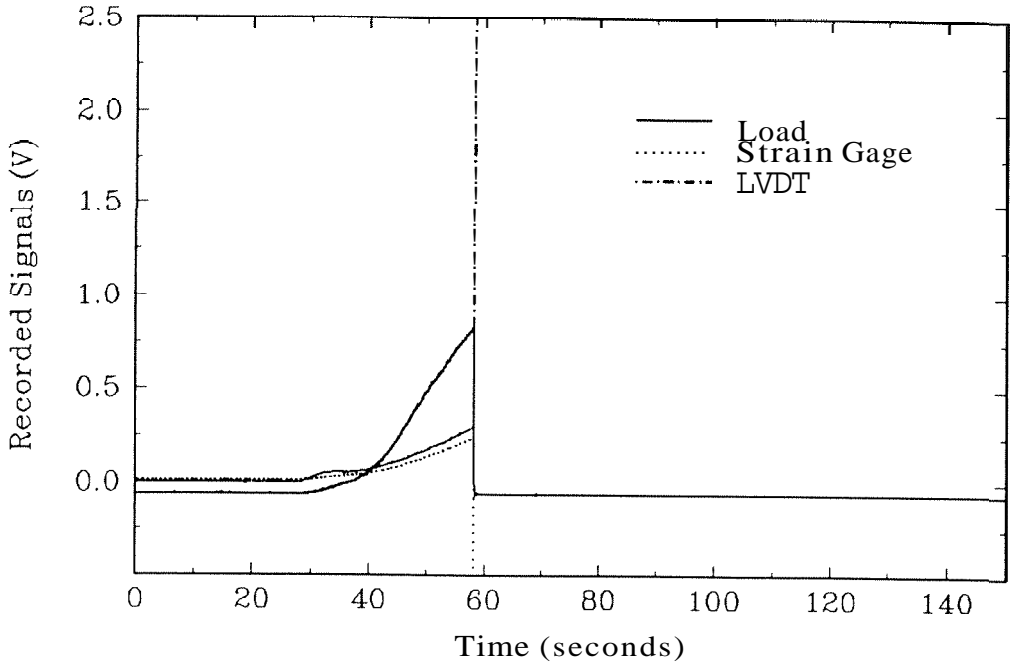
Figure 5.2 Axial load, strain and LVDT signals in a quasi-static experiment on Macor without confinement.
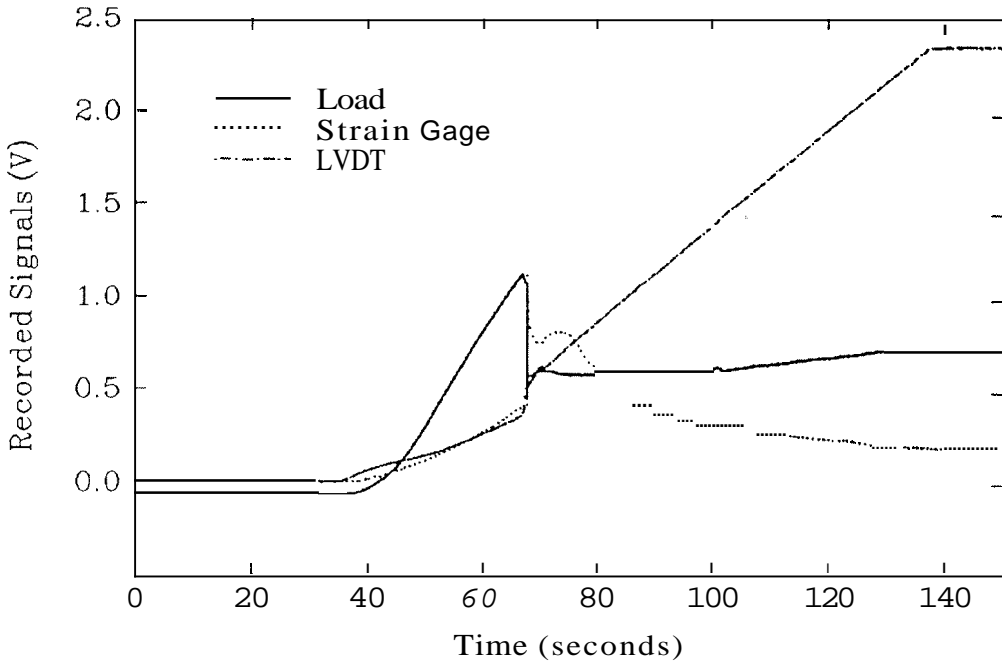
Figure 5.3 Axial load, strain and LVDT signals in a quasi-static experiment on Macor with 47 MPa confinement.
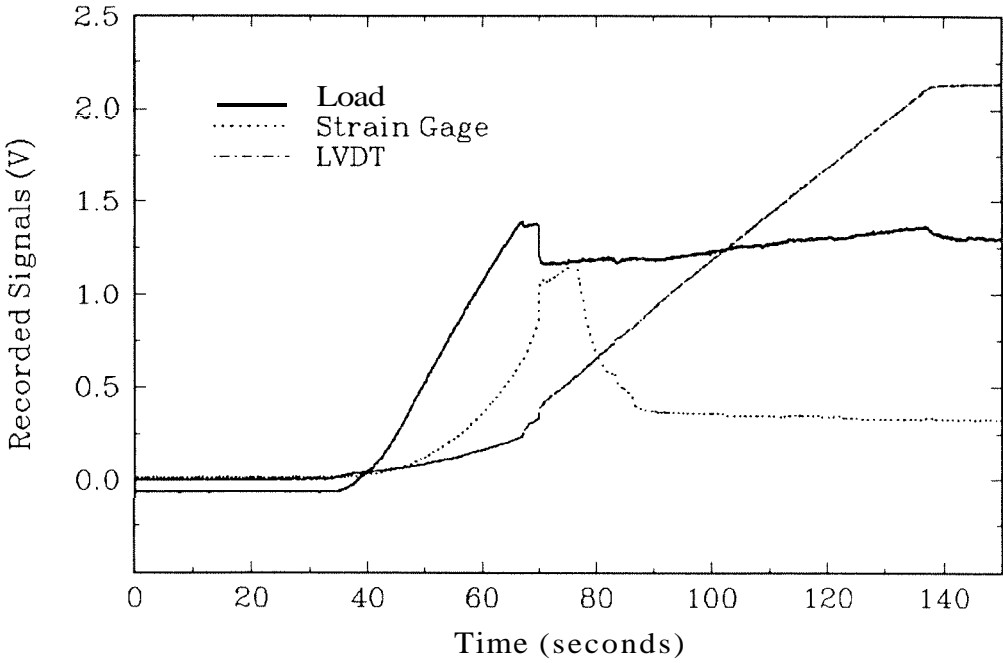
Figure 5.4 Axial load, strain and LVDT signals in a quasi-static experiment on Macor with 88 MPa confinement.
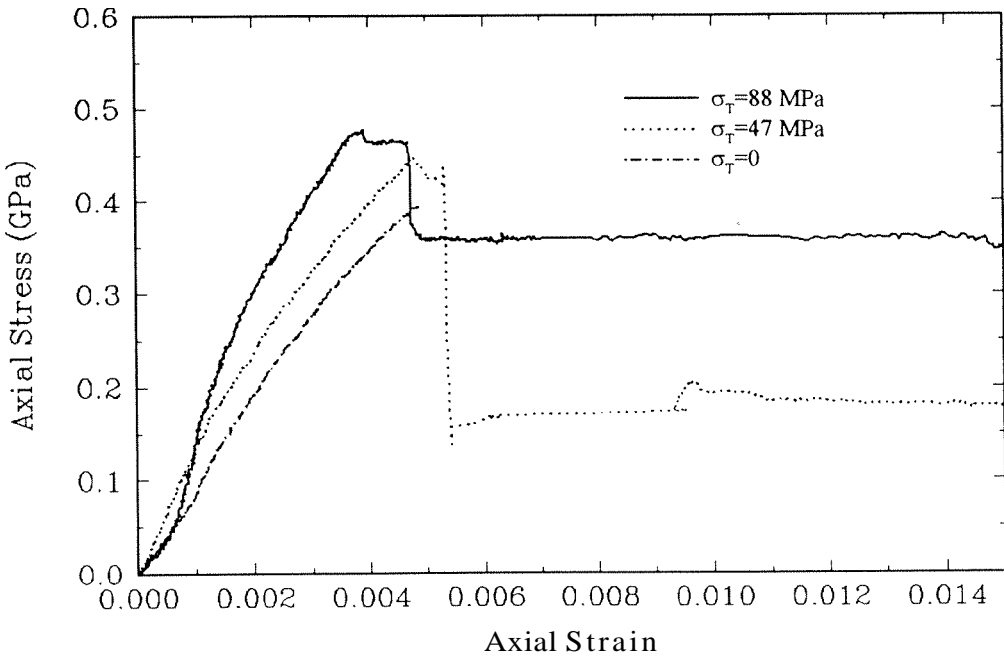
Figure 5.5 Quasi-static stress-strain curves of Macor under various confinement.
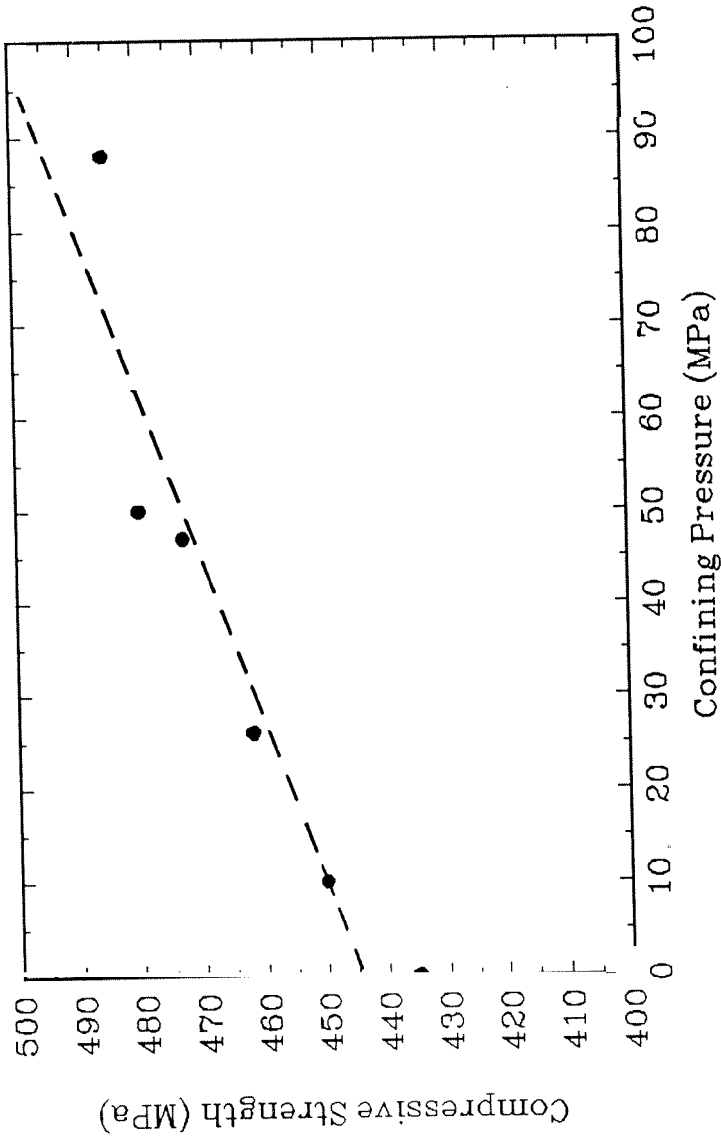
Figure 5.6 Variation of quasi-static compressive strength of Macor with confinement.
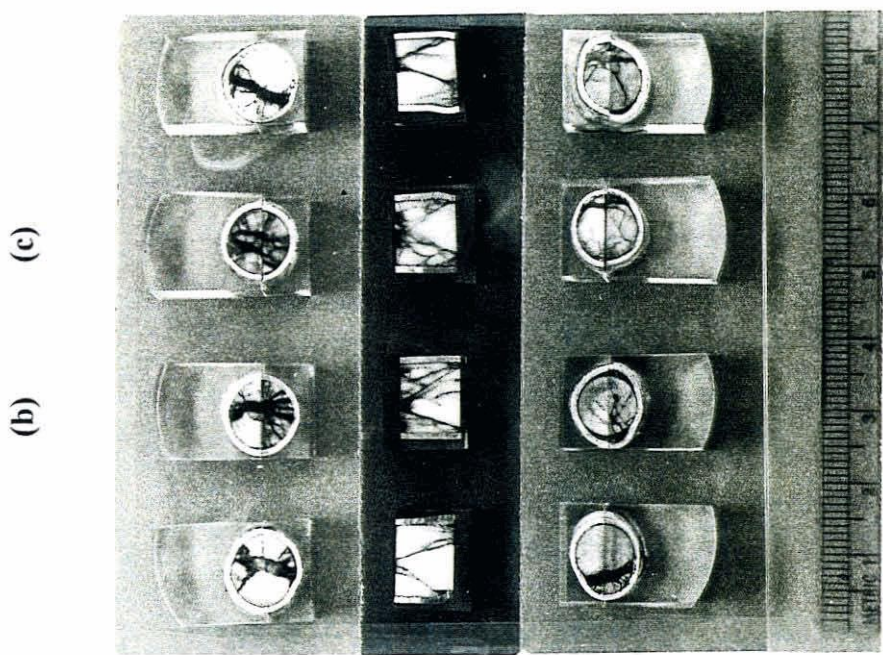
Figure 5.7 Recovered Macor specimens from quasi-static experiments.

Sleeves: (a) 6061 Al (σ_T=26 MPa), (b) brass (σ_T=47 MPa),

(c) 2024 Al (σ_T=50 MPa) and (d) 303 stainless steel(σ_T=88 MPa).
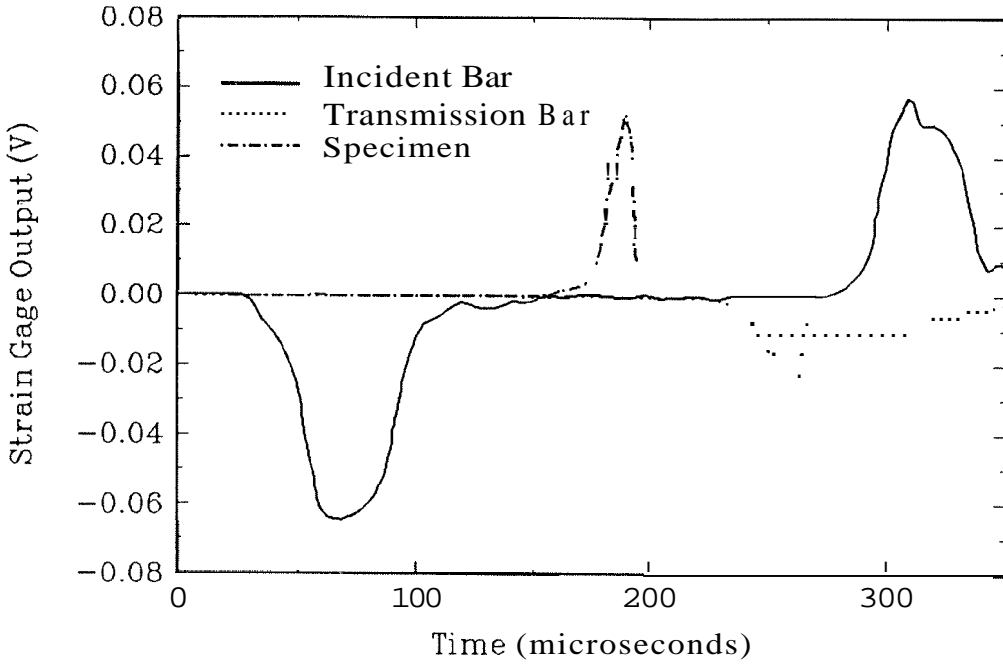
Figure 5.8 Strain gage signals from the incident bar, transmission bar and the specimen recorded from a dynamic experiment on Macor using the modified SHPB.
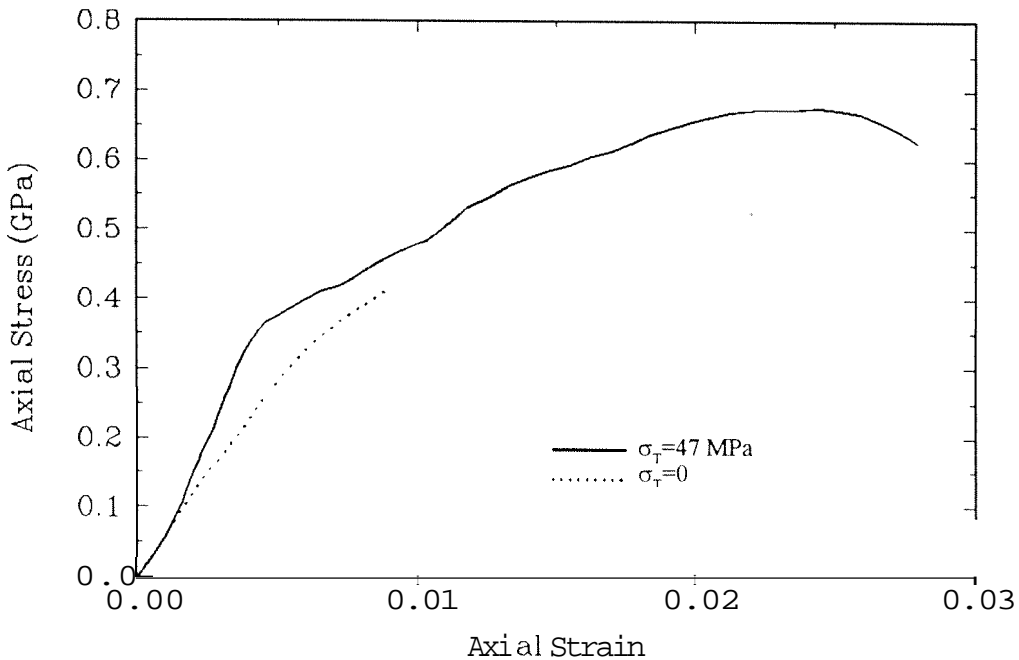
Figure 5.9 Dynamic stress-strain curves of Macor specimens with and without lateral confinement.

$\sigma_T = 47$ MPa
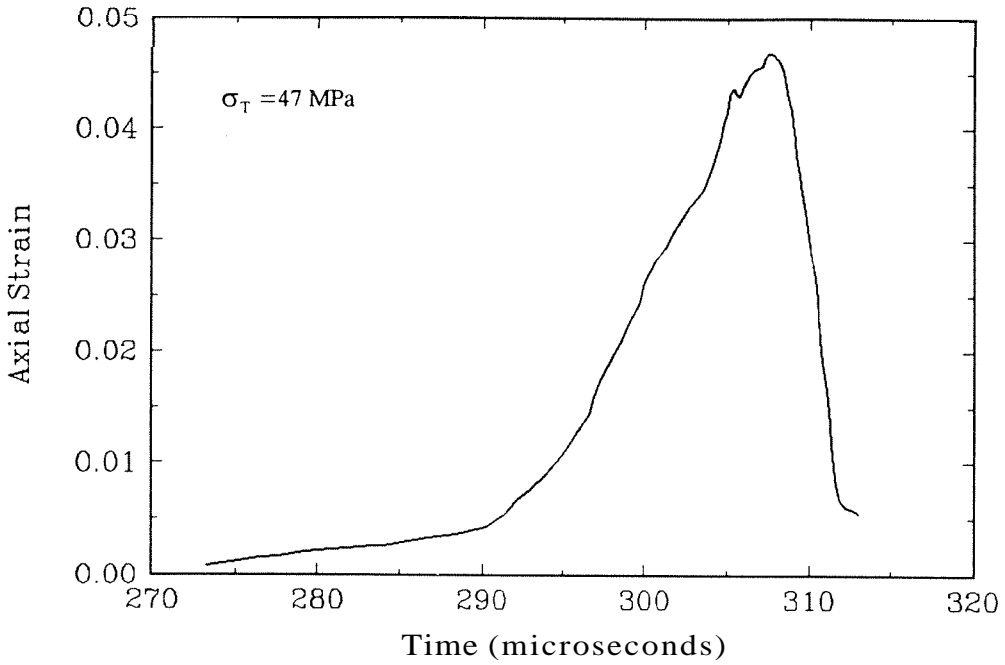
Figure 5.10 Macor specimen strain profile during a dynamic experiment.
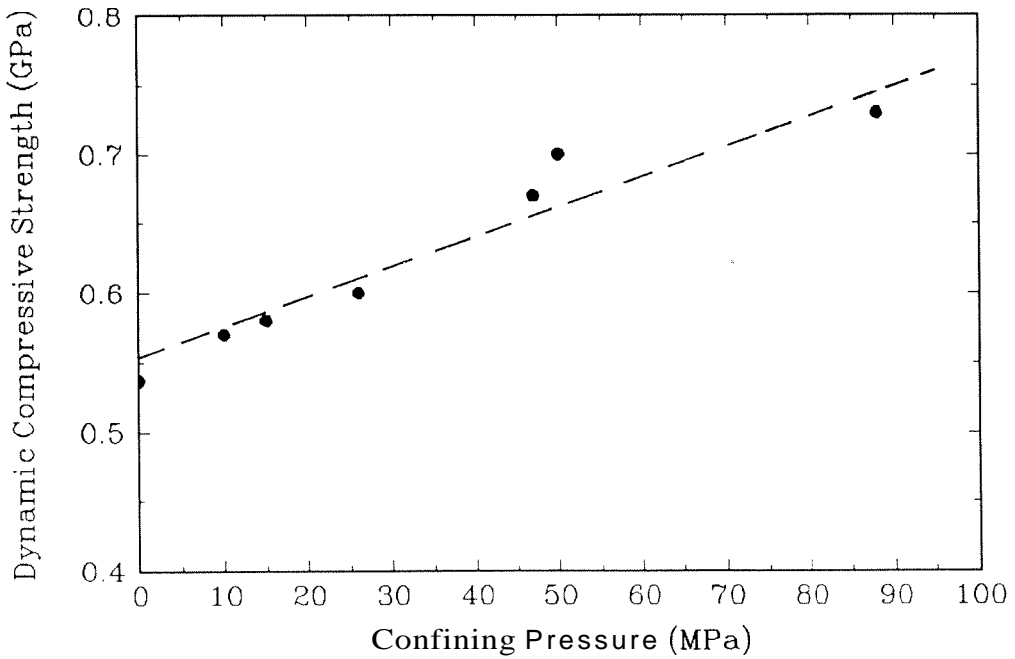
Figure 5.11 Variation of dynamic compressive strength of Macor as a function of lateral confinement.
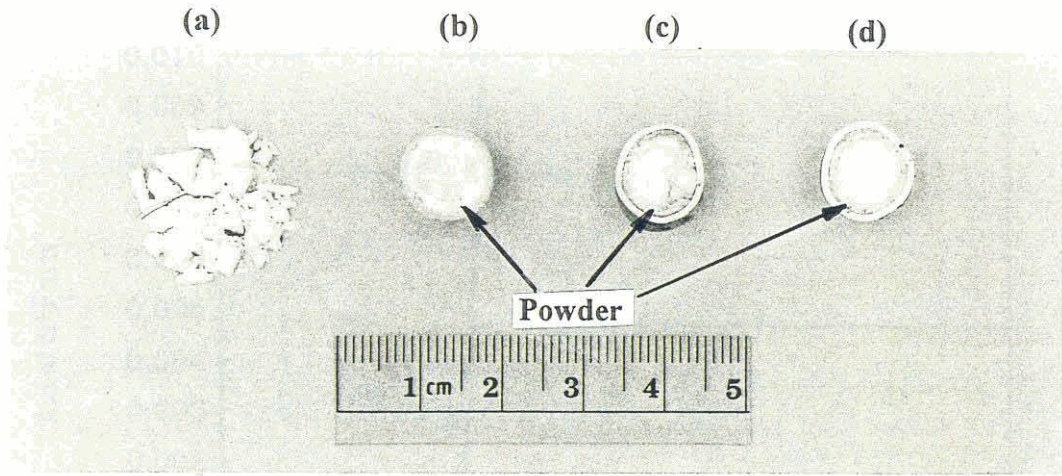
Figure 5.12 Recovered Macor specimens from dynamic experiments.
Sleeves: (a) unconfined ($\sigma_T=0$), (b) nylon ($\sigma_T=15$ MPa),
(c) copper ($\sigma_T=22$ MPa) and (d) brass ($\sigma_T=47$ MPa).
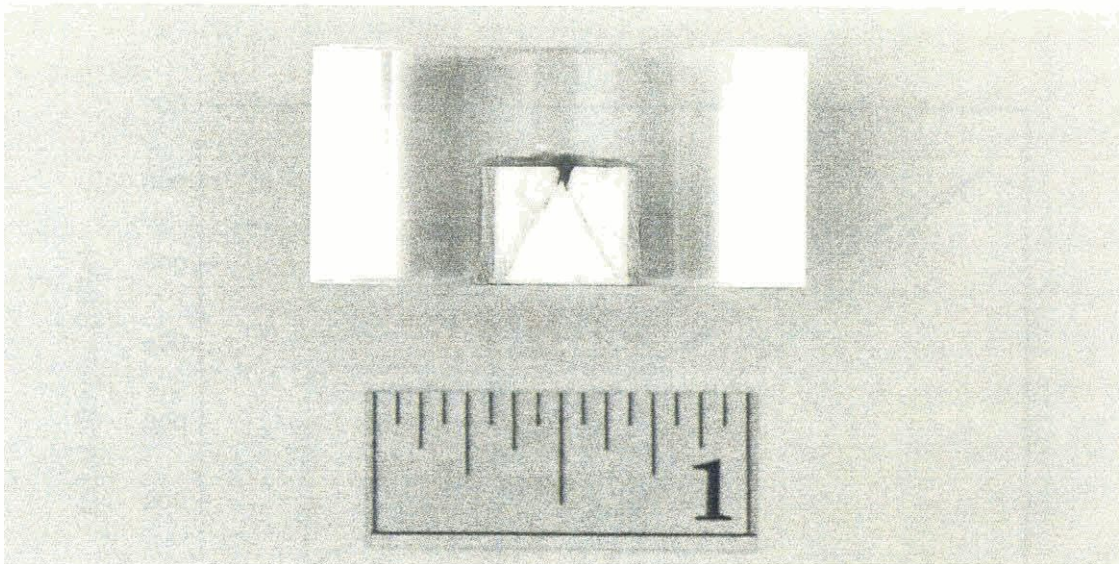
Figure 5.13 Axial cross section of a recovered Macor specimen with confinement
pressure of $\sigma_T=47$ MPa.
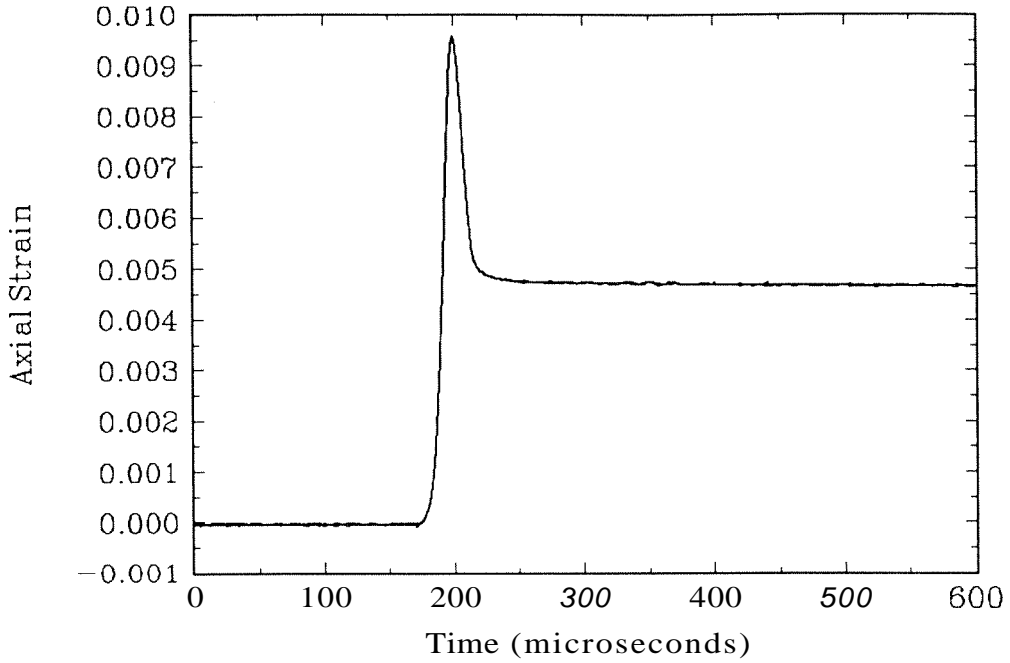
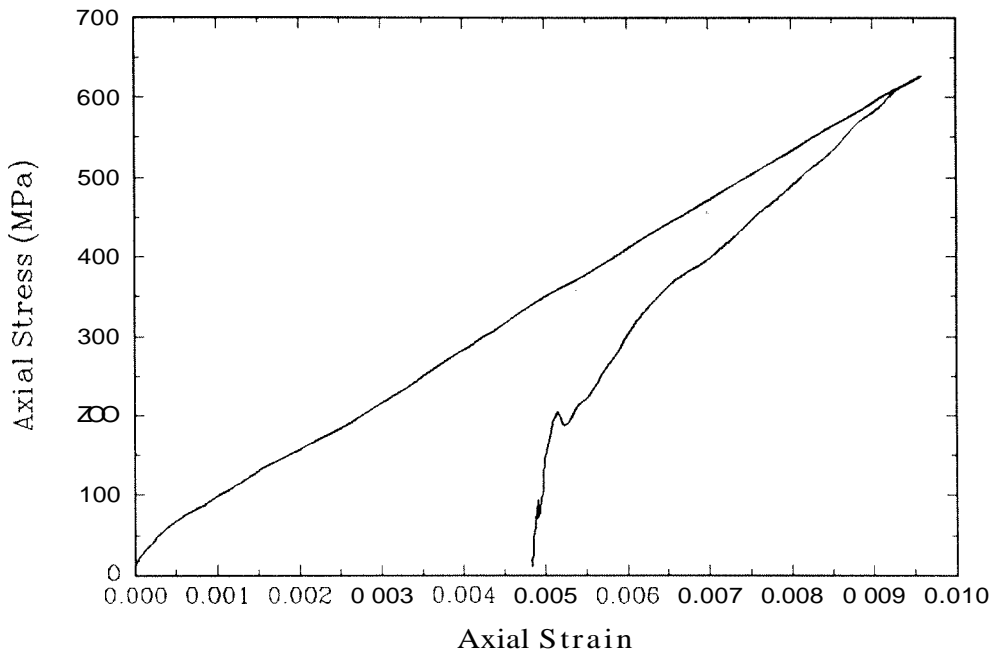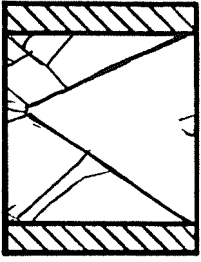**Figure 5.14 Typical specimen strain signal in the fault initiation experiments on Macor.**
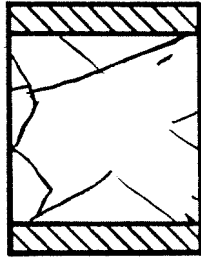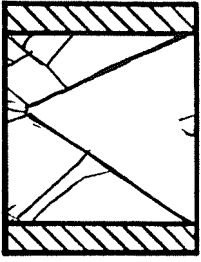

Figure 5.15 Typical stress-strain curve in the fault initiation experiment on Macor.

(a)

(b)

(c)

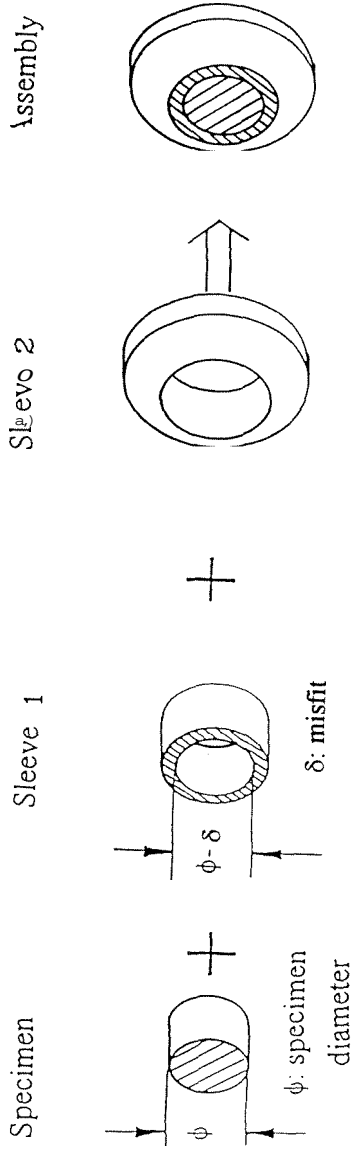**Figure 5.16 The process of the fault formation in the confined Macor specimen.**

Figure 5.17 A schematic illustration of specimen confined by two concentric shrink fit sleeves.
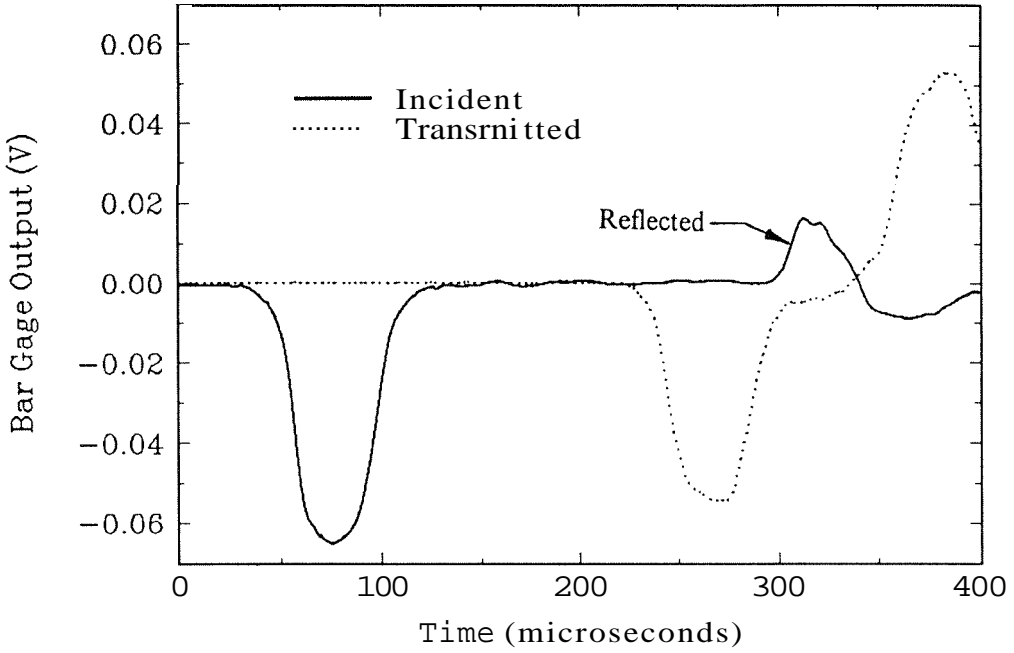
Figure 5.18 Typical incident and transmitted signals from an SHPB experiment with double sleeved Macor specimen (σ_T=230 MPa).
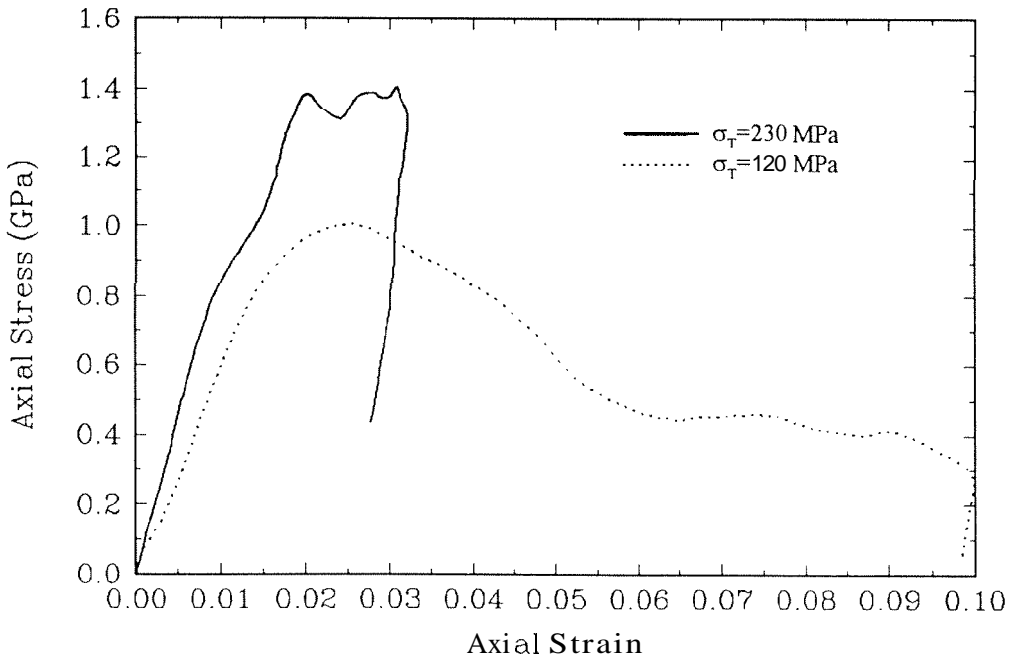
Figure 5.19 Dynamic stress strain curves of double sleeved Macor specimens.
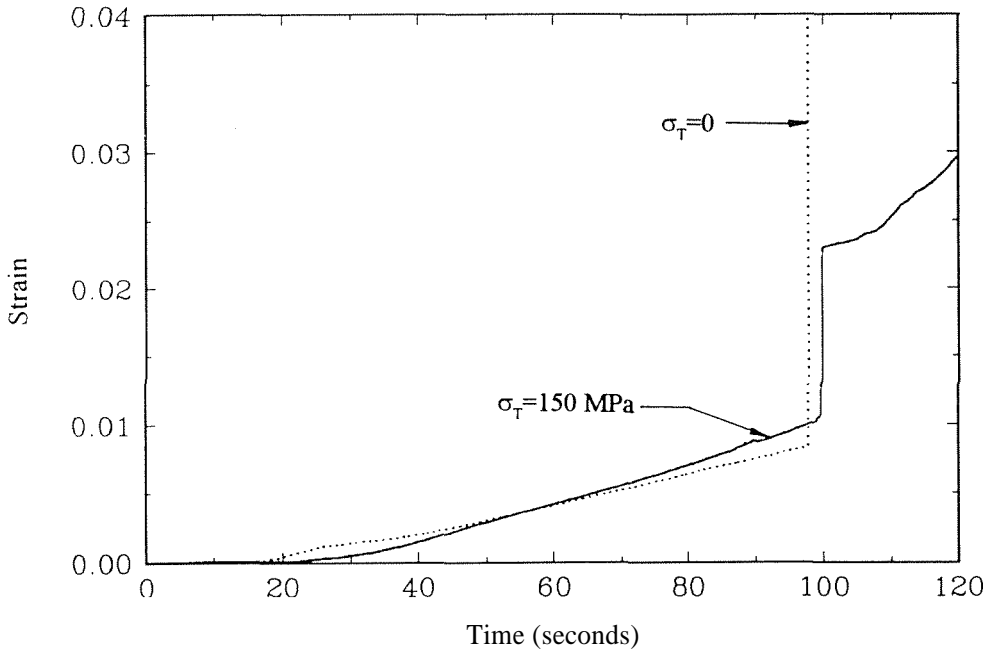
Figure 5.20 **The variation of strain as a function of time for AIN under quasi-static**

loading with no confinement (dotted line) and a confining pressure of

150 MPa (solid line).
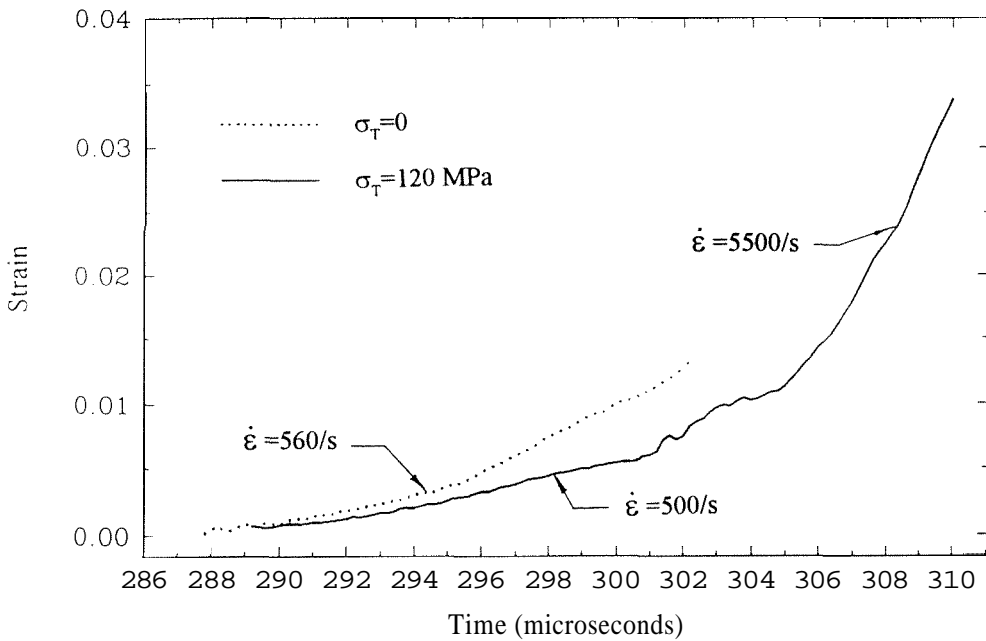
Figure 5.21 **The variation of strain as a function of time for AIN under dynamic**

loading with no confinement (dotted line) and a confining pressure of

120 MPa (solid line).
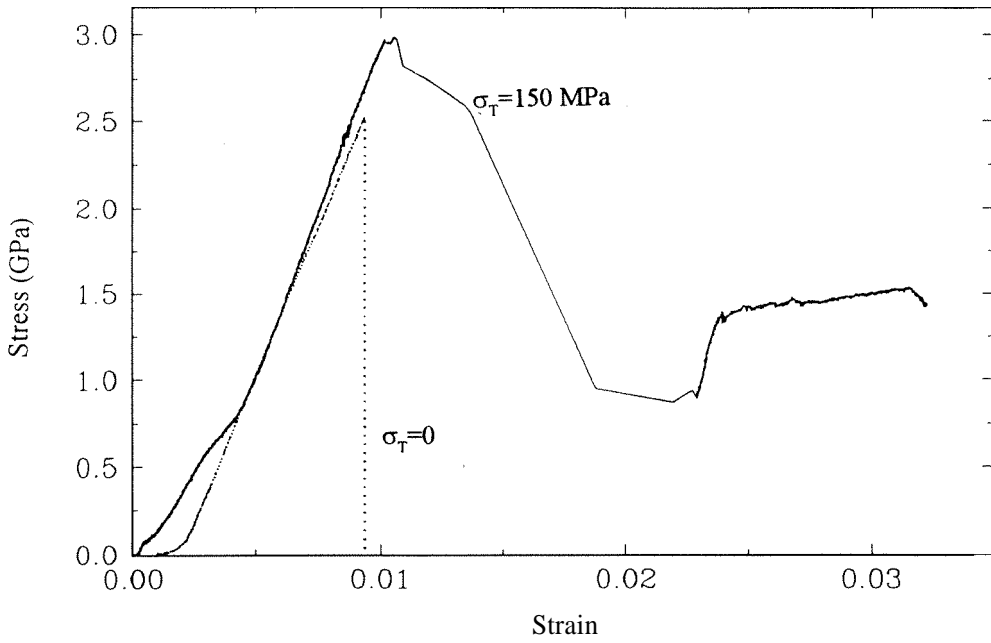
Figure 5.22 Axial stress verses strain for unconfined (dotted line) and confined (solid   line) sintered AlN specimens under quasi-static loading.
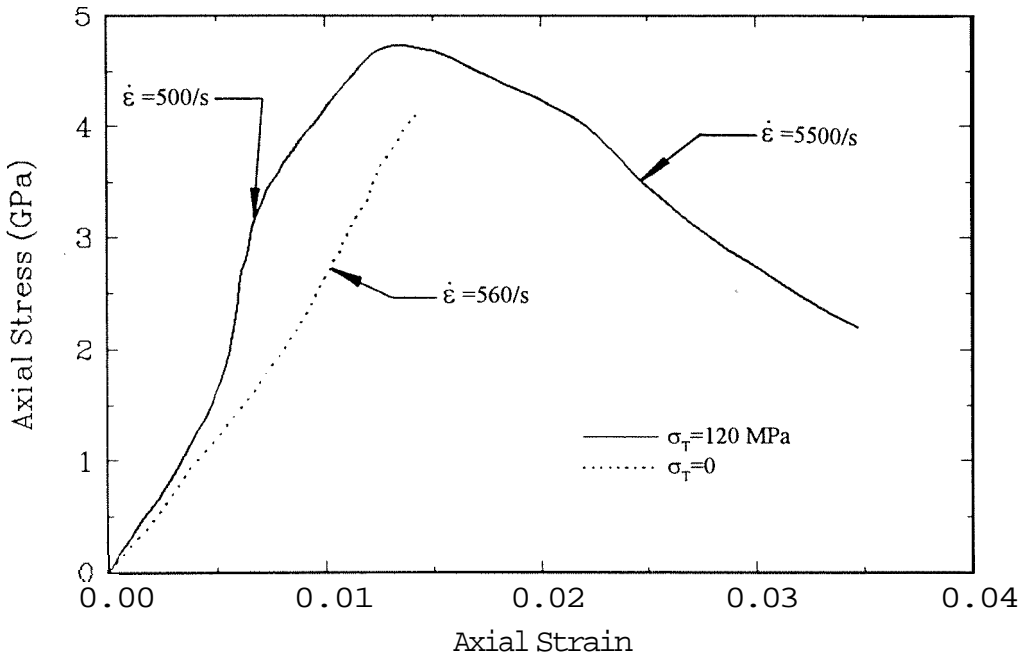
Figure 5.23 Axial stress verses strain for unconfined (dotted line) and confined (solid line)sintered AlN specimens under dynamic axial loading.
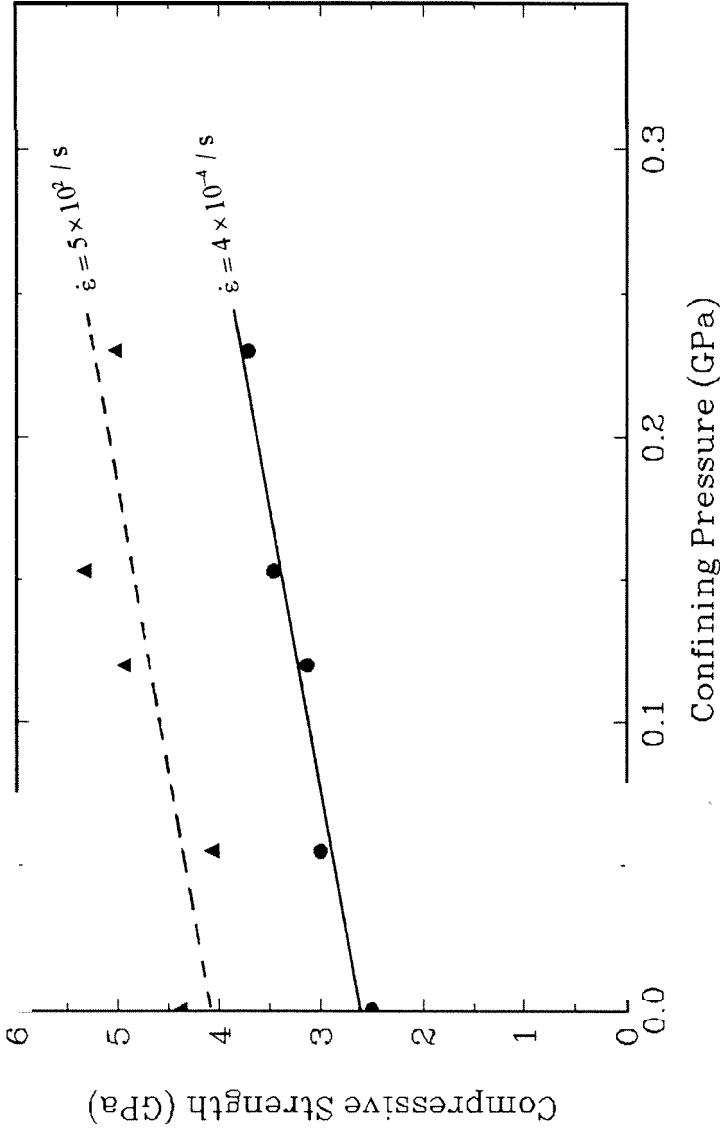
Figure 5.24 The variation of compressive strength of AlN as a function of confining pressure for dynamic and quasi-static loading.
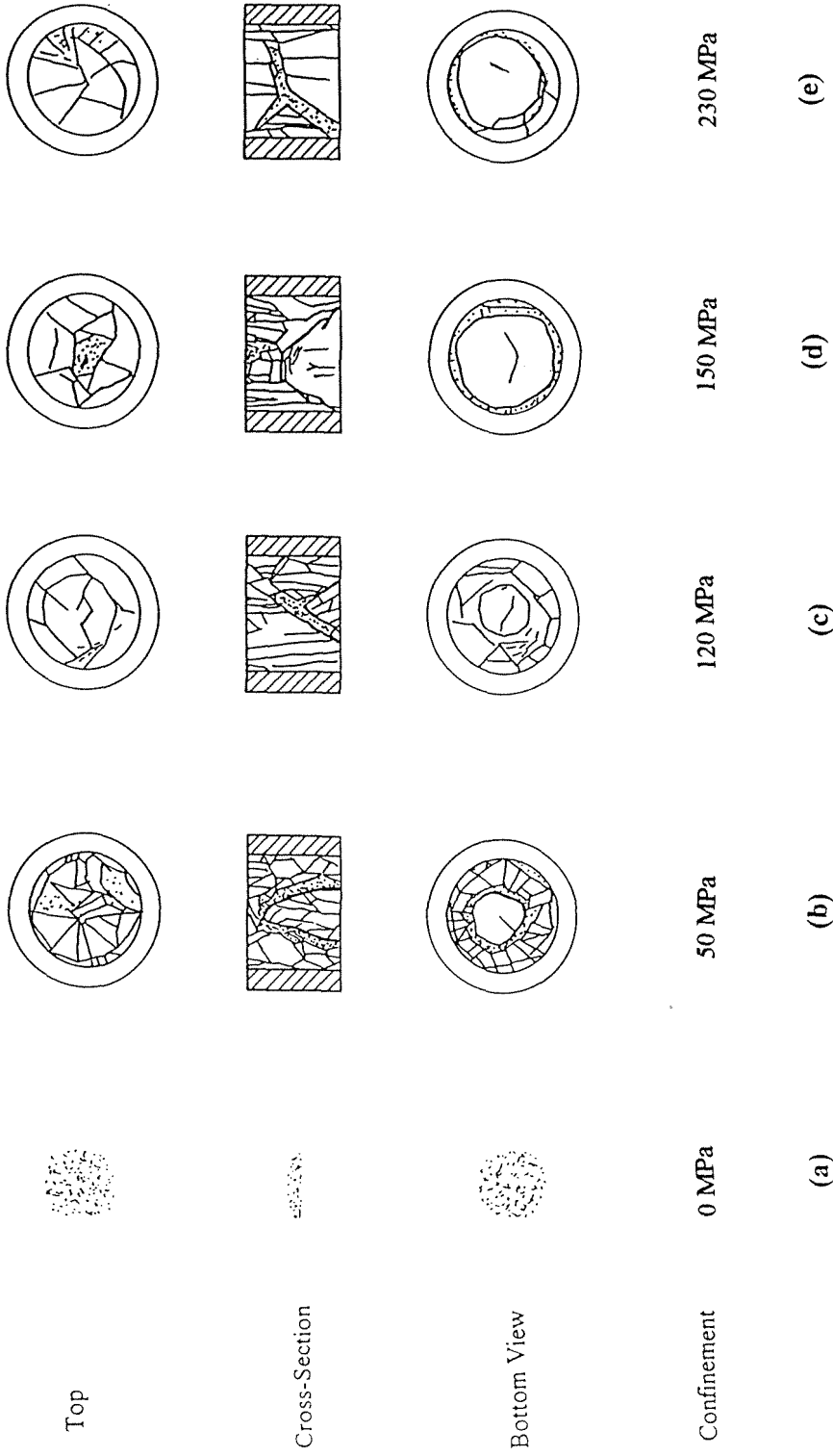
Figure 5.25 Portraits of the recovered AlN specimen from SHPB experiments.
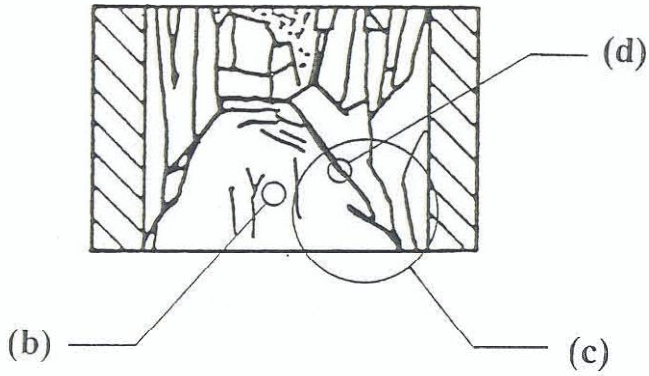
(a) Locations of micrographs in the specimen.
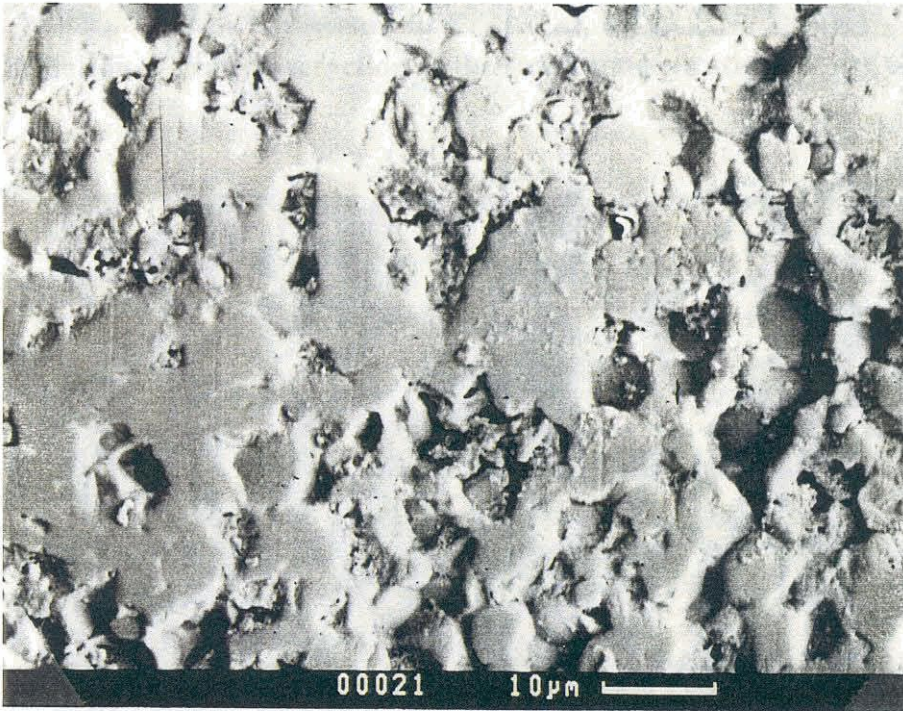
(b) Illustration of low crack density inside the cone.

Figure 5.26 Scanning electron micrographs of the axial cross-section of a recovered
sintered AlN specimen.
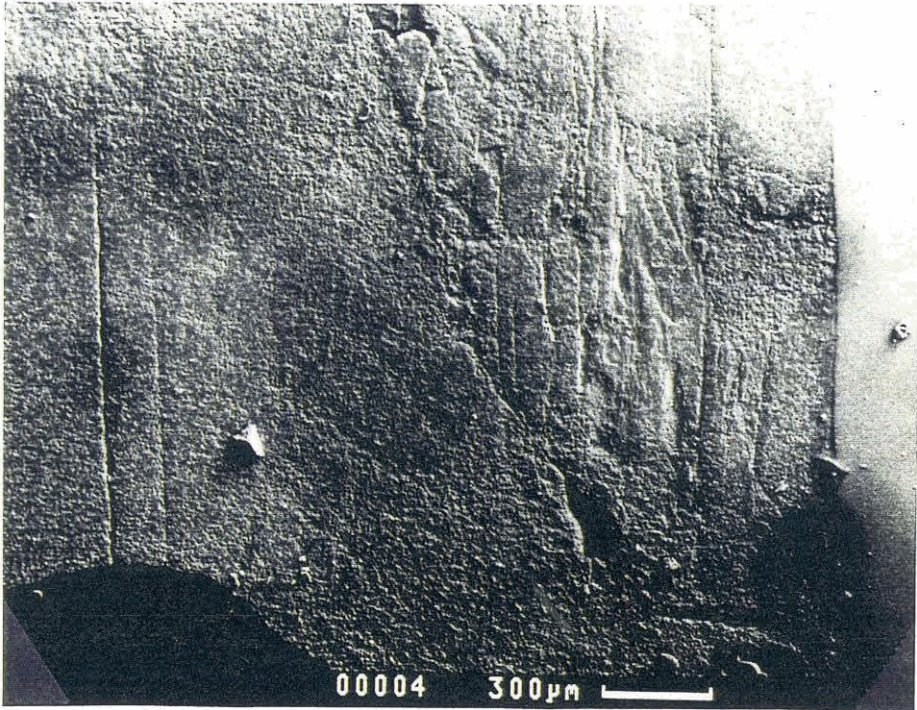
(c) Initiation of crack interaction at the stress concentrations at the corner.
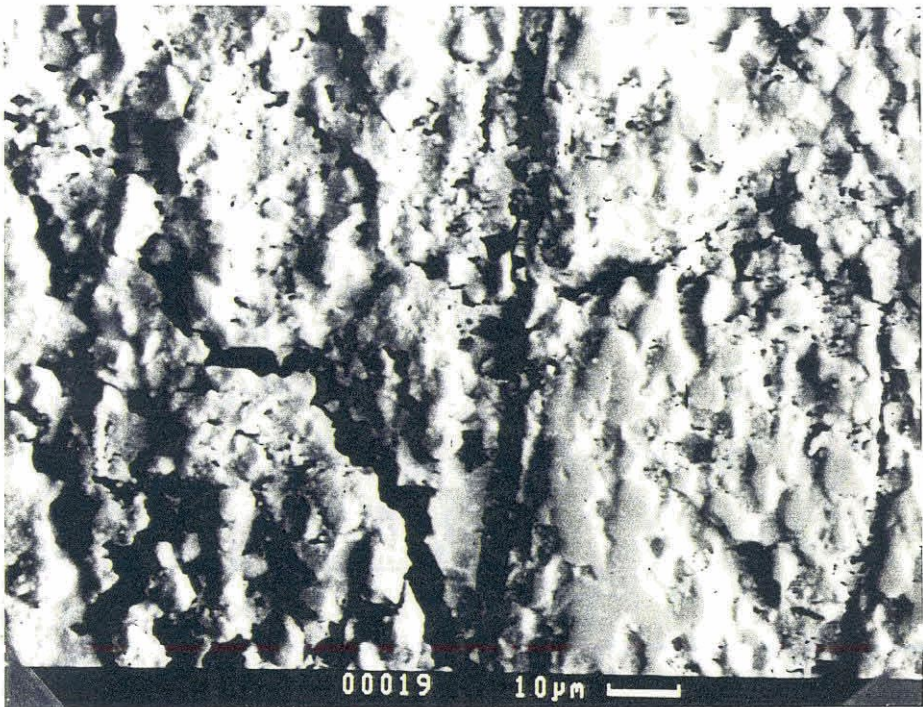
(d) High crack density on the fault.
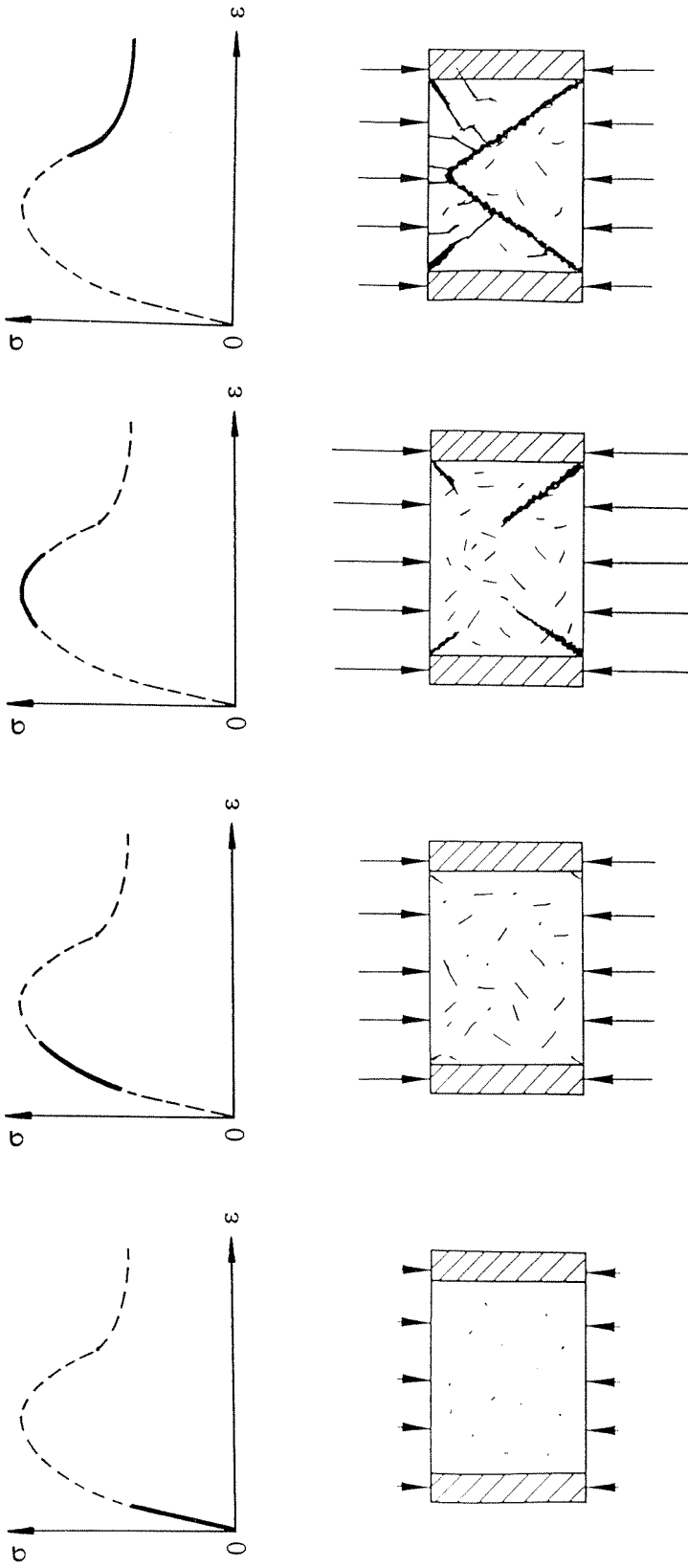
Figure 5.27 A schematic illustration of a proposed failure mechanism in ceramic specimens under moderate confinement.

Chapter 6

A Failure Criterion for Brittle Ceramics

Abstract

Based on the experimental results on AlN together with data available in the literature, a failure/flow criterion for ceramics is presented. A Mohr-Coulomb criterion and an improved Johnson-Holmquist model were found to fit the experimental data for brittle failure, whereas the ceramic materials under investigation exhibited pressure insensitive plastic flow at high pressures. Experimental observations made in other types of dynamic experiments (e.g., shock wave loading) were rationalized based on the failure mechanisms and the possibility of plastic flow beyond the Hugoniot elastic limit (HEL). The effect of various material properties on the failure behavior was investigated based on the failure criterion. It appears that the Poisson's ratio plays an important role in underlying explanations of observed behavior, and it influences the material behavior subsequent to HEL. A lower value of the Poisson's ratio indicates that it is more difficult to activate plastic deformation even under uniaxial strain loading, and hence the materials fail in a brittle manner. Materials with higher Poisson's ratios are expected to deform plastically under high amplitude impact loading. The effect of increasing levels of damage and its implications on failure is discussed. The effect of strain rate on the failure criterion is discussed and is quantified based on an activation process. The applicability of the present model to a range of ceramics is also explored and the limitations of the model are outlined.

6.1 Introduction

A failure criterion is needed for ceramic materials in order to use these materials properly and efficiently in various engineering applications. In order to establish the existence of a failure criterion, the failure behavior of the material must be understood under various loading conditions. Experimental investigations into the failure behavior of ceramic materials have been conducted under quasi-static multiaxial loading conditions. For example, Heard and Cline (1980) studied the mechanical behavior of various types of polycrystalline BeO, Al_2O_3, and AIN ceramics under quasi-static loading at confining pressures up to 1.25 GPa. Dynamic experimental data currently available in the literature essentially are limited to the results from two specific loading paths: uniaxial stress and uniaxial strain. Typically, the uniaxial stress experiments are performed using the split Hopkinson (Kolsky) pressure bar, whereas the uniaxial strain experiments are conducted using plate impact. Plate impact experiments have produced a considerable amount of data on the HEL and spall strength of ceramics.

A number of models have been proposed to explain the observed failure behavior of ceramic materials. However, there has been little success in explaining the trends associated with the behavior of these materials. These models have primarily been based upon Griffith's failure criterion to quantify the dependence of the ratios of spall strength to HEL on parameters such as the Poisson's ratio. For example, Grady (1995) used the variation of the ratio of spall strength over Hugoniot elastic limit (HEL) as a function of the Poisson's ratio for various ceramics obtained from plate impact experiments to fit the failure models proposed by Murrel (1963) and Rosenberg (1993). However, the discrepancy between the experimental data and the prediction of the models is apparent as shown in Fig. 5.1 of Grady's report (1995).

The compressive strength data obtained under dynamic multiaxial compression loading conditions presented in Chapter 5 provides extensive experimental data on ceramics for varying loading paths and for the corresponding failure modes. This data provides a more complete background from which a more realistic failure criterion for ceramics could be established. In this chapter, a failure criterion for ceramic materials is proposed based on theoretical arguments and experimental evidence. The possible mechanisms for plastic flow beyond HEL in materials with high Poisson's ratio are outlined and are examined in the light of available experimental data. The models investigated are used to explain the earlier experimental observations. The proposed failure criterion also provides clues toward resolving some existing controversies about performance of ceramic materials under impacting loading. In particular, the applicability of the failure model is illustrated for the characterization of failure waves (Brar *et al.,* 1991, Kanel' *et al.,* 1992) in brittle materials created by uniaxial strain shock wave loading. The limitations of the model are also discussed.

6.2   The Failure Criterion

6.2.1 Rationale for the Failure Criterion

When a brittle solid is loaded either quasi-statically or dynamically to failure by axial compression, crack initiation, propagation, and interaction are considered to be the dominating failure mechanism if the lateral confinement is low. This was demonstrated by the experimental results presented in Chapters 2 and 5. The brittle compressive failure mode was observed to be either axial splitting under uniaxial stress or faulting under moderate confinement pressure. The sources of crack initiation in brittle materials have been simplified to two fundamental types: a spherical cavity and a sharp microcrack.

Theoretical investigations based on fracture mechanics have been performed on these two simplified cases (e.g., Horii and Nemat-Nessar, 1986, Ashby and Sammis, 1990). A typical picture of a microscopic sliding crack is shown in Fig. 6.1. New cracks initiate from the two ends of an existing crack when the opposite crack surfaces slide against each other under loading. The analytical results showed that a brittle material will fail under multiaxial compression when

$$\sigma_1 = c\sigma_3 - \sigma_c \tag{6.1}$$

where σ_1 is the axial stress, c is a material constant, σ_3 is the transverse stress, and σ_c is the unconfined compressive strength. This failure criterion has been validated by experiments conducted under quasi-static loading conditions on brittle materials (Ashby and Sammis, 1990).

Equation (6.1) is equivalent to the following form in terms of mean pressure and shear strength of the material (assuming $\sigma_2 = \sigma_3$):

$$|\tau| + \alpha p = \tau_0 \tag{6.2}$$

where

$$p = -\frac{1}{3}\sigma_{kk} = -\frac{1}{3}(\sigma_1 + 2\sigma_3)$$

$$|\tau| = \frac{1}{2}|\sigma_1 - \sigma_3|$$

$$\alpha = \frac{3(1-c)}{2(2+c)}$$

$$\tau_0 = -\frac{3\sigma_c}{2(2+c)}$$

where $|\tau|$ is the absolute value of shear strength, p is the hydrostatic or the hydrodynamic pressure, τ_0 is the shear strength of the material without any pressure (pure shear), and a, referred to as the internal friction coefficient, is the proportionality coefficient between $|\tau|$ and p. Equation (6.2) is recognized as the Mohr-Coulomb failure criterion in rock mechanics (e.g., Jaeger and Cook, 1979). A generalized form of the Mohr-Coulomb failure criterion is known as the Drucker-Prager criterion (Drucker and Prager, 1952).

The physical significance of Eqn. (6.2) may be described as follows. In the brittle failure process, the inelastic deformation of the specimen is accommodated by the crack propagation and interaction with crack surfaces sliding against each other. Friction exists on the sliding surfaces which resists the sliding motion. The magnitude of the friction depends on the pressure acting on the surfaces. The bulk material behavior is expected to reflect the averaged microscopic behavior. Therefore, the shear bearing capability of the bulk material is expected to increase with increasing pressure acting on the specimen. The higher the pressure, the higher the frictional resistance, hence the higher the shear strength of the material. Equation (6.2) is the simplest phenomenological expression describing this physical picture. At the same time, Eqn. (6.2) is consistent with the failure criterion derived from fracture mechanics as shown above by the equivalence of Eqn. (6.1) to Eqn. (6.2).

6.2.2 Failure Criterion for AlN

Recently extensive research into the strengths of ceramic materials has been carried out by researchers using various types of experiments to simulate a variety of loading conditions. For example, Heard and Cline (1980) investigated the mechanical behavior of various types of polycrystalline BeO, Al_2O_3, and AlN ceramics under quasi-static loading

with lateral confinement. Rosenberg *et al.* (1991) explored the dynamic high-pressure properties of AlN by flyer plate impact experiments. Chapters 2 and 5 of this dissertation presented the strength data obtained from the quasi-static and dynamic experiments on Macor and a sintered AlN under multiaxial compression. The axial compressive strength data obtained from these experiments varied with the amount of the confinement and with the strain rates. As will be demonstrated in the following sections, the simple failure criterion expressed in Eqn (6.2) provides a possible unified approach under which the various experimental results can be properly interpreted.

6.2.2.1   The Mohr-Coulomb Failure Surface

The failure strength data of AlN under various confining pressures and at two strain rates (presented in Fig. 5.24 of Chapter 5) are plotted in the p-z plane as shown in Fig. 6.2. The data points can be connected approximately by two straight lines. The solid and dashed lines in Fig. 6.2 represent the failure surfaces of the sintered AlN in the p-z plane at strain rates of 5×10^2 s^{-1} and 4×10^{-4} s^{-1}, respectively. Inspection of Fig. 6.2 reveals two distinct features: (1) all the data points at a single strain rate fall on a reasonably straight line as predicted by Eqn. (6.2); (2) the quasi-static and dynamic failure surfaces for AlN appeared to be parallel. The value of slope a was determined to be approximately 1.0 for both quasi-static and high strain rates, and τ_0 was 0.3 GPa under quasi-static loading and 0.7 GPa under dynamic loading. The increased shear strength under dynamic loading from that under quasi-static loading appears to be independent of pressure in this brittle failure region. Therefore, when the Mohr-Coulomb failure criterion is used to describe the failure behavior of AlN, the value of a appears to be independent of the strain rate. The strain rate thus affects only the pure shear strength, $z_,$. Therefore, the failure surface on the p-z plane at any strain rate may be determined from this value of a and a

single data point at the strain rate of interest. It should be noted that the data in Fig. 6.2 are relevant only to the discussions of brittle failure. However, the experimental data presented in Chapter 5 indicate that, within the brittle failure range, the failure behavior of the material did follow the failure criterion predicated by Eqn. (6.2). Although the data presented in Fig. 6.2 are the results from sintered AlN, other ceramics behave similarly as will be shown later. The failure criterion expressed by Eqn. (6.2) may not be applicable to ceramic materials with high spall strengths as will also be shown later.

Only limited experimental data is available for the dependence of shear strength on strain rate. Experiments conducted by Gilat *et al.* (1992) on Al_2O_3 using a torsional Kolsky bar showed that shear strength had no strain rate dependence. However, a stress state of pure shear without any pressure can be treated as a uniaxial compression stress state superposed with hydrostatic tension. Brittle materials under pure shear are thus expected to fail by brittle cracking. Crack initiation and propagation were also recognized to dominate the spall strength (Grady, 1995). Due to the similarity in the failure mechanism, the strain rate dependence of τ_0 is expected to be similar to the dependence of spall strength on the strain rate which was given by Grady (1995). Therefore, the dependence of τ_0 on strain rate is postulated as:

$$\tau_0 \propto (\rho^2 c^3 \Gamma \dot{\gamma})^{\frac{1}{3}} \tag{6.3}$$

where ρ is the mass density of the material, c is the elastic wave velocity, Γ is the energy release rate (surface energy), and $\dot{\gamma}$ is the shear strain rate.

6.2.2.2   Johnson-Holmquist Model

Another failure criterion for brittle materials is the improved Johnson-Holmquist model (referred as the JH-2 model, see Johnson and Holmquist, 1994 and Holmquist *et al.*, 1995) where the normalized strength is expressed as

$$\sigma^* = \sigma_i^* - D(\sigma_i^* - \sigma_f^*) \tag{6.4}$$

where σ_i^* is the normalized strength of the intact material, σ_f^* is the normalized strength of the fractured material, and D is the damage $(0 \leq D \leq 1)$. The equivalent stresses $(\sigma, \sigma_i, \sigma_f)$ have been normalized by σ_{HEL}, the equivalent stress at the HEL. The equivalent stress is defined in terms of principal stresses as

$$\sigma = \sqrt{\frac{1}{2}[(\sigma_1 - \sigma_2)^2 + (\sigma_2 - \sigma_3)^2 + (\sigma_3 - \sigma_1)^2]}$$

In the case of a cylinder subjected to axial and transverse loading, $\sigma_1 = \sigma_A$, and $\sigma_2 = \sigma_3 = \sigma_T$. Hence,

$$\sigma = \sqrt{\frac{3}{2}}(\sigma_A - \sigma_T) \tag{6.5}$$

where σ_A and σ_T are the axial and transverse stresses respectively. The normalized strength of the intact material in the JH-2 model is given by

$$\sigma_i^* = A(P^* + T^*)^N (1 + C \ln \dot{\varepsilon}^*) \tag{6.6}$$

where A, C, N are material constants to be determined by experiments. The normalized pressure is $P^* = P / P_{HEL}$, where P is the actual pressure and P_{HEL} is the pressure at HEL. The normalized tensile hydrostatic pressure is $T^* = T / P_{HEL}$, where T is the maximum tensile hydrostatic pressure the material can withstand. The actual strain rate $\dot{\varepsilon}$ is normalized by the reference strain rate of $\dot{\varepsilon}_0 = 1.0\,s^{-1}$ as $\dot{\varepsilon}^* = \dot{\varepsilon} / \dot{\varepsilon}_0$.

The experimental data shown in Fig. 6.2 were used to determine the material constants in order to compare this model to the Mohr-Coulomb criterion. The data presented in Fig. 6.2 were obtained from intact AlN specimens as described in Chapter 5, Fig. 5.24. Therefore, D=0 in the JH-2 model. Only three material constants need to be determined: A, N, and C. Using the data points in Fig. 4.2 and taking P_{HEL}=4.35 GPa, and σ_{HEL}=6.70 GPa (Grady, 1995), the constants were found to be A=1.10, N=0.987, and C=0.0546. Thus,

$$\sigma_i^* = 1.10(P^* + 0.169)^{0.987}(1 + 0.0546\ln\dot{\varepsilon}^*) \qquad (6.7)$$

If the value of N is approximated as 1.0, the above equation for $\dot{\varepsilon} = 500\,s^{-1}$ can be simplified in terms of the terms used in Eqn. (6.2) to

$$\tau = 0.93p + 0.62 \qquad (6.8)$$

Comparison of Eqns. (6.2) and (6.8) reveals that they have exactly the same form, with only slight differences in the constants. A plot of the JH-2 model prediction for AlN under dynamic loading is shown in Fig. 6.2. It appears that the failure behavior of AlN can be described by both the Mohr-Coulomb criterion and the improved Johnson-Holmquist model when the material fails in a brittle manner.

6.2.3 Brittle-Ductile Transition in AlN

As the pressure further increases beyond the range of Fig. 6.2, the brittle failure mode may be expected to change gradually to ductile failure. Heard and Cline (1980) found in their quasi-static tri-axial experiments that there was a brittle-ductile transition in hot-pressed AlN when confining pressure reached 0.55 GPa. As indicated by the brittle-ductile transition observed in Macor (Section 5.3), under dynamic loading conditions, a similar trend in the failure surface shape change could reasonably be expected for ceramic materials. Although a similar transition could not be observed in the present dynamic multiaxial experiments on AlN due to the limitations in confinement pressure, the failure surface shown in Fig. 6.2 may be extended using data from other types of experiments in literature.

The dynamic experimental data in Fig. 6.2 are plotted again in Fig. 6.3, together with the spall strength and Hugoniot elastic limit (HEL) data for AlN reported by Grady (1995). In addition, Rosenberg *et al.* (1991) also tested AlN at pressure values beyond HEL by using the plate impact technique. These results are also plotted in Fig. 6.3. The embedded manganin gage technique they used in their experiments enabled the measurement of both axial and lateral stress components in the specimen. Inspection of the results indicates that the shear strength of AlN remains nearly constant at 3.5 GPa after HEL. Grady's experimental results reported by Dandekar *et al.* (1994) on the shear strength of AlN in the wurtzite phase also indicated that the shear strength remained nearly a constant of approximately 2.8 GPa at pressure values beyond HEL and up to 18 GPa. At low confining pressure, the failure surface of AlN appeared as a straight line in the p-τ plane, which agrees with the prediction of brittle failure mechanism expressed by Eqns. (6.2) and (6.8). The inclined straight line was connected by a short convex line whose slope decreases continuously as the pressure is increased. This convex line

represents the transition region between brittle and ductile behavior. The shear strength is essentially constant as the pressure increases from 5 GPa to 11 GPa as shown in Fig. 6.3. The Hugoniot elastic limit is located at the end of the brittle-ductile transition region. It should be noted that a straight line parallel to the p-axis in the p-z plane represents the failure surface of a material which fits a von Mises or Tresca type of failure criterion where the dominant mechanism is the pressure insensitive plastic flow. A different interpretation of the data obtained by Rosenberg et *al.* has been presented by Dandekar *et al.* (1994). The data points at pressures above 11 GPa in Fig. 6.3 indicates that there was an increase in shear strength. This increase was considered by Rosenberg *et al.* (1991) to be the result of a phase transformation in the material due to the high pressure. High pressure phase transformation in AlN under shock wave loading has been investigated by Kipp and Grady (1994).

The failure surface of AlN in the p-z plane may be roughly divided into two linear portions connected by a region associated with the brittle-ductile transition. When the pressure is below the transition region, the shear strength of the material is linearly proportional to the pressure on the specimen through the slope a, and the material fails in a brittle manner. The brittle failure modes have been characterized as either cracking or faulting. After the brittle-ductile transition, the shear strength is independent of pressure in the absence of a phase transformation. Plastic flow is expected during the horizontal portion of the failure surface since the failure behavior agrees with the predictions of theories based on incompressible plastic flow such as the von Mises or Tresca failure criterion.

Based on the currently available experimental results, the failure mode of the material depends on the location of the final stress state on the failure surface. Figure 6.4 illustrates schematically change in the failure mode along the failure surface. When brittle

materials are tested under tensile loading, the strength is determined by the unstable propagation of a single crack inside the material. The resistance of the material to crack propagation, namely, fracture toughness K_{IC} and flaw size, determines the tensile strength of the material. Typically, the tensile strength or spall strength of brittle materials is small compared to the compressive strength. Therefore, the data point for spall strength of brittle materials on a p-z plane is very close to the origin. When a ceramic specimen is under axial compression loading with little or no lateral confinement, it is well established that the specimen fails by axial splitting as a result of crack nucleation and propagation. When moderate lateral pressure is introduced, the failure mode appears to be the localized deformation on faults as described in Chapter 5. Brittle-ductile transition then occurs as the confining pressure is increased further. In this transition region, plastic strain localization is expected to be responsible for the failure. Under high pressure, microcrack initiation and propagation may be suppressed completely, and dislocations or twins could be expected to propagate from stress concentrations such as the tips of the closed, sliding microcracks in the specimen. In this case, a plasticity failure criterion such as the von Mises or the Tresca criterion provides a more appropriate description of the flow behavior. However, the mechanisms for the plastic deformation in brittle materials under high pressures are not well understood at the present time due to the paucity of experimental data. In addition, phase transformation may be induced at very high pressure as discussed earlier in this section.

Although the above discussion focused specifically on the failure surface of AlN in the p-z plane, the failure criterion may be applicable to other brittle materials. Figure 6.5 shows the failure surfaces in the p-z plane of some other ceramic and geological materials up to HEL. The data points shown in Fig. 6.5 were obtained under quasi-static tri-axial loading conditions (Heard and Cline, 1980) except the points at the lowest and highest pressure on each curve, which were spall strength and HEL, respectively, obtained under

shock wave loading (Grady, 1995). It is clear from Fig. 6.5 that the failure behavior of Al$_2$O$_3$, BeO (Heard and Cline, 1980) and granite (Ashby and Sammis, 1990) is very similar to the behavior of aluminum nitride shown in Fig. 6.3. The brittle-ductile transition under quasi-static loading has been postulated and analyzed by Horii and Nemat-Nasser (1986).

6.2.4 Effect of Friction Coefficient

In the brittle failure region, a simplified physical picture of microcrack initiation and propagation was shown in Fig. 6.1. In this model, the shear strength of the material depends on the pressure through friction between the crack surfaces (Coulomb law, Jaeger and Cook, 1979) as discussed earlier. Therefore, the slope of the failure surface line in the brittle failure region depends intrinsically on the friction coefficient of the fractured surfaces. Based on the fracture mechanics analysis of the model shown in Fig. 6.1 performed by Horii and Nemat-Nasser (1986), and Ashby and Hallam (1986), it was found that cracks would start to propagate when (Ashby and Sammis, 1990)

$$\sigma_1 = \frac{(1+\mu^2)^{\frac{1}{2}}+\mu}{(1+\mu^2)^{\frac{1}{2}}-\mu}\sigma_3 - \frac{\sqrt{3}}{(1+\mu^2)^{\frac{1}{2}}-\mu}\frac{K_{1c}}{\sqrt{\pi a}} \qquad (6.9)$$

where μ is the coefficient of friction acting across the crack surfaces, K_{1c} is the fracture toughness of the material, and 2a is the length of the original inclined crack. If the stress state at failure of the material is proportional to the stress state at which cracks start to propagate, then the coefficient a in Mohr-Coulomb criterion (Eqn. (6.2)) is related to the coefficient of friction μ by

$$\alpha = \frac{3\mu}{3(1+\mu^2)^{\frac{1}{2}} - \mu} \qquad (6.10)$$

The coefficient, α, is a fbnction of only the friction coefficient, μ. Figure 6.6 is a plot of the variation of failure surface slope **a** as a fbnction of the friction coefficient μ. The value of **a** increases almost linearly as μ increases until μ reaches a value of 0.8 when the slope of the α-μ curve begins to decrease. For all practical situations, μ must have a value between 0 and ∞, and, therefore

$$0 \le \alpha < 1.5. \qquad (6.11)$$

When α=0, and sliding is frictionless, and deformation will be purely pressure insensitive plastic flow as observed in ductile materials where shear strength is independent of applied pressure. The case of α=1.5 corresponds to the failure under uniaxial stress without any lateral confinement in which $p = \frac{1}{3}\sigma_A$ and $|\tau| = \frac{1}{2}\sigma_A$, where σ_A is the applied axial stress. For AlN, **a** = 1.0 as shown in Fig. 4.2; the corresponding friction coefficient μ was calculated using Eqn. (6.10) to be 1.13. Eqn. (6.10) may explain the reason for the slope of the failure surface under both quasi-static and dynamic loading conditions to be the same, since the friction coefficient μ is not expected to vary with the strain rate. This value is higher than the typical value of the friction coefficient for engineering ceramics which is approximately 0.6. There are two possible reasons for this discrepancy. First, the model shown in Fig. 6.1 may be an over simplification of actual microcracking process, and second, the frictional behavior on the microscale may be different from that measured using two large macroscopically flat surfaces.

6.2.5 Effect of the Loading Path on Failure

The area under the failure surface on the p-z plane can be referred to as the operational region of the material for loading. In the operational region, the loading path can be varied arbitrarily without the occurrence of failure. Each of the loading paths will terminate on the failure surface when failure occurs. Figure 6.7 illustrates various loading paths approaching the failure surface. When the specimen is loaded under uniaxial stress, the loading path is a straight line passing through the origin with a slope of 1.5 (indicated as path (1) in Fig. 6.7); failure will occur when the line intersects the failure surface. It should be noted that a straight line intersecting the origin of the p-z plane is a proportional loading path on which all the principal stress components increase or decrease proportionally. The loading path of uniaxial strain can be illustrated as another example. Initially, the loading path is also a straight line passing through the origin with a slope of $\frac{3}{2}\frac{(1-2\nu)}{(1+\nu)}$, where ν is the Poisson's ratio of the material. If the material fails before the HEL is reached, there will be a discontinuous jump in shear stress from the original loading path to the failure surface (indicated as path (2) in Fig. 6.7). In this case, the proportionality among the stress components cannot be maintained; the magnitude of the jump in shear stress depends on the axial loading level as discussed below.

In uniaxial strain loading, the pressure and the shear in the specimen material can be calculated using

$$p = \frac{1}{3}(1 + 2\frac{v}{1-v})\sigma_A = \frac{1+v}{3(1-v)}\sigma_A$$

$$\tau = \frac{1}{2}(1 - \frac{v}{1-v})\sigma_A = \frac{1-2v}{2(1-v)}\sigma_A$$

(6.12a, b)

where σ_A is the axial stress. The jump in shear $\Delta\tau$ from the original loading path to the failure surface can be determined using Eqns. (6.2) and (6.12):

$$\Delta\tau = \alpha\frac{1+v}{3(1-v)}\sigma_A + \tau_0 - \frac{1-2v}{2(1-v)}\sigma_A$$
$$= \frac{(2\alpha-3)(1+v)+3v}{6(1-v)}\sigma_A + \tau_0.$$

(6.13)

When failure occurs, the axial stress cannot increase instantaneously. Therefore, the lateral stress components have to drop abruptly to facilitate the jump in shear stress. This sudden drop in confining pressure may indicate that extensive cracking has occurred, breaking the specimen into smaller fragments with little lateral contact. If this was true, a measurable amount of dilatancy would be evident near failure. Clearly, this phenomena could not occur in ductile materials. Figure 6.8 shows the expected variations with time of the axial, lateral stress components and the pressure during a uniaxial strain experiment. When failure occurs before HEL, there will be a sudden decrease in lateral stress σ_T. As a result, the mean pressure will also drop suddenly as indicated by the arrows in Fig. 6.8. If the specimen does not fail before HEL as indicated by the dashed lines in Fig. 6.8, the loading path has to turn at the HEL from the proportional path to the horizontal line along the failure surface as shown in Fig. 6.7. This transition also terminates the proportionality in the loading. In this case, the lateral confinement will increase at the same rate as the

axial stress so that there will be net increase only in pressure and not in shear. This is schematically illustrated by the three dashed lines after HEL in Fig. 6.8. Therefore, there is a sudden increase in lateral confinement at the HEL from $\frac{v}{1-v}\sigma_A$ to σ_A, which implies that the Poisson's ratio of the material jumps to a value infinitesimally close to 0.5 at HEL.

6.2.6 Effect of Damage on Failure Surface

When undamaged or intact brittle materials are loaded to failure using various experimental techniques, the failure strength data should fall on a failure surface of the type discussed above. When previously damaged materials are loaded to failure, the operational region under the failure surface is expected to decrease as the extent of the pre-damage is increased. As shown in Fig. 6.9, the pre-damage is characterized by the damage parameter, D. The reduction of the operational region has a lower bound set by the complete comminution of the brittle material where no more damage can be introduced, and D assumes its maximum value D_{MAX}. It should be mentioned that the damage parameter cannot be isotropic even though the brittle material is isotropic before damage occurs. Typically, there are measurable differences in the elastic properties of a recovered brittle specimen along different axes following axial loading by a dynamic pulse of significant enough amplitude to initiate damage (Subhash *et al.* 1993). The measured directional dependence of elastic properties of the damaged specimen indicates that the damage parameter D depends heavily on the form of the prior loading and will not be isotropic. Therefore, care must be taken in the definition of the damage parameter for brittle materials. There are several models for brittle failure which use a scalar damage parameter, for example, the JH-2 model discussed above and the Rajendran and Grove model, Rajendran (1992).

If the failure surface has been reached during the loading process, the material will be damaged, if not failed catastrophically upon unloading, and the degree of damage will depend on the loading history. The damage parameter can be used to characterize the difference in the failure surfaces of intact and damaged materials. The failure surface for the damaged material will be located below the failure surface for the intact material as shown schematically in Fig. 6.9. Therefore, if the material is reloaded after partial or complete unloading during which failure initiated, the further failure behavior of the damaged material will follow the failure surface for damaged material with the corresponding value of D. The shear strength of the damaged material will be lower than that of the intact material under the same pressure as shown in Fig. 6.9. This may be illustrated by the example of loading path (2) in Fig. 6.7. If failure occurs under uniaxial strain condition before HEL (as shown by path (2) in Fig. 6.7), there will be a jump in the shear stress as predicted by Eqn. (6.13). After the initial failure, the cracked material will be subsequently compacted by the axial load, and significant damage would have been accumulated. The process of compaction may be unstable in a manner similar to the results obtained on confined AlN as shown in Figs. 5.22 and 5.23. The unstable compaction behavior will cause partial unloading as shown in each figure. The failure surface of this damaged material will be located below the one for the intact material. Therefore, there will be a corresponding drop in shear stress immediately after the sudden increase in shear stress expressed by Eqn. (6.13). The magnitude of the drop will depend on the extent of the damage. There must be an abrupt increase in transverse stress to facilitate the drop in shear stress. The material will be compacted during this stage immediately after the dilatation, evidenced by a sudden increase in shear stress, which occurs when failure initiates.

The completely comminuted state of a ceramic can be treated as powder. The high strain rate behavior under confining pressure of granulated ceramics have been investigated by Klopp and Shockey (1991) and Sairam and Clifton (1994) using the pressure-shear plate impact technique. Their results show that in the limiting state, the powder behave like a Mohr-Coulomb material with a slope (a in Eqn. (6.2)) of approximately 0.2.

6.3   The Effect of Poisson's Ratio on Failure Behavior

The behavior of ceramics and other brittle materials under high pressures have been investigated extensively using shock wave techniques (e.g., Ahrens *et al.*, 1968, Kipp and Grady, 1989, Rosenberg *et* al. 1992, Dandekar, 1994a). These experiments have produced considerable data on the **HEL** and spall strength of a variety of ceramics. There have been also a number of key observations concerning the behavior of ceramics under shock wave loading beyond **HEL** (Longy and Cagnoux, 1989, Rosenberg, 1993, Dandekar, 1994, Tranchet, 1994, Grady, 1995). The shear strength of ceramics beyond their **HEL** is of considerable interest (Rosenberg *et al.*, 1991 and 1992, Dandekar, 1994b, Grady, 1995). In this section, the experimental observations made during the shock wave loading experiments will be rationalized based on the failure behavior discussed above and the possibility of plastic flow beyond HEL. **A** simplified version of the failure criterion proposed in the last section indicates that, the Poisson's ratio plays an important role in the underlying explanations of observed behavior. Also, the Poisson's ratio influences the material behavior subsequent to the **HEL.** It is shown that materials with low Poisson's ratio would tend to fail by brittle cracking which leads to fragmentation, whereas the materials with a high Poisson's ratio would have the ability to flow (microplasticity) under high pressures beyond **HEL.** It is interesting to note that most ceramics have a Poisson's

ratio greater than 0 and less than 0.25 and most metals have a Poisson's ratio higher than 0.25 and less than 0.5. This implies that the value of the Poisson's ratio of a material may indicate the degree of the brittleness of the material.

6.3.1 Effect of State of Stress in Uniaxial Strain on Failure

In a low Poisson's ratio material such as titanium diboride (TiB_2), Poisson's ratio 0.05, the following observations have been made based on shock wave experiments: (Dandekar and Benfanti, 1993, Dandekar, 1994b, Ewart and Dandekar, 1994) (i) the shock wave exhibits two wave structures, a small cusp at 5-6 GPa and a prominent cusp at 12-13 GPa (which is assumed to be the HEL), (ii) the spall strength increases slightly up to 5-6 GPa, begins decreasing rapidly thereafter, and looses the spall strength entirely beyond the HEL, (iii) even beyond the HEL, the material continues to exhibit the shear strength which is a measure of its load carrying capability. It has been observed in TiB_2, that the microcracks do nucleate and grow below the HEL (Ewart and Dandekar, 1994). On the other hand, in high Poisson's ratio material such as alumina (AD995), the spall strength is independent of the peak amplitude of the shock wave and is nearly a constant for a given impulse. This is true even for shock amplitudes beyond the HEL (Dandekar, 1994a).

In this section, the state of stress in uniaxial strain conditions achieved by shock wave loading will be considered. The transverse stress is a function solely of the Poisson's ratio under uniaxial strain loading. It is shown through the analysis of the failure process that the transverse stress has considerable influence on the observed failure/flow phenomena in ceramics. In spite of the numerous experimental observations, the effect of the state of stress on failure under shock wave loading has not been investigated. A

simplified version of the failure criterion which was presented in the previous section provides a realistic failure criteria below HEL, and it provides the range of Poisson's ratios for which brittle failure is dominant. The possible mechanisms for plastic flow beyond HEL in materials with high Poisson's ratio are outlined and examined in the light of available experimental data. The models investigated were used to explain the experimental observations outlined earlier.

6.3.1.1 Lower Bound Failure Surface

A failure surface was constructed for AlN based on the strength data from various types of experiments as shown in Fig. 6.3. Such failure surfaces can be constructed only for a very limited number of brittle materials due to the lack of experimental data. However, considerable amount of HEL and spall strength data for ceramics are available in literature from shock wave experiments (Grady, 1995). The strength data reported by Grady (1995) were obtained under uniaxial strain conditions. Inspection of Fig. 6.7 reveals that these data may be utilized to reveal the failure behavior of ceramics under uniaxial strain shock wave loading. The spall strength and the HEL appear as two points on the p-z plane. A straight line connecting these two points represents the lower bound of the failure surface between the spall strength and the HEL. The section of the actual failure surface between the spall strength and the HEL will be located above the lower bound which is verified using the data available for a few brittle materials as shown in Fig. 6.5. The spall strength of most brittle materials is very low compared to corresponding values of the HEL. Therefore, the point representing the spall strength on the failure surface is relatively close to the origin in the p-z plane. Thus, the uniaxial strain loading path from the origin to the HEL is approximately equivalent to the lower bound of the

failure surface from the spall strength to the HEL. The slope of the uniaxial strain loading path, tan$, is determined by the Poisson's ratio of the material v:

$$\beta = \tan\phi = \frac{3}{2}\frac{1-2v}{1+v} \tag{6.14}$$

where ϕ is angle from p-axis to the uniaxial strain loading path. This slope β will hereafter be referred to as the slope of the lower bound of the failure surface. The variation of β with the Poisson's ratio v is plotted in Fig. 6.10.

Grady (1995) reported the spall strength and the HEL for a variety of engineering ceramic materials. Table 6.1 lists the Young's Modulus, the Poisson's ratio, the pressure at spall p_s, the shear strength at spall τ_s, the pressure at the HEL p_h, and the shear strength at the HEL τ_h for TiB_2, SiO_2, SiC, B_4C, WC, AlN, Al_2O_3 and ZrO_2. The averaged pressure and shear values were converted from the data reported by Grady (1995) based on the assumptions that the material is under a one-dimensional strain state both at the spall strength and the HEL and remains linearly elastic up to HEL. Figure 6.11 shows the straight lines connecting the spall strength and the HEL, representing the lower bound of the failure surfaces for the materials listed in Table 6.1. Inspection of Figs. 6.10 and 6.11 indicates that the slope of the lower bound line increases as the Poisson's ratio of material decreases as expected from Eqn. (6.14). WC and ZrO_2, which possess relatively high spall strengths, are the exceptions to this trend. An increase in slope indicates that a higher shear stress is required to cause failure of the ceramic material at a given pressure. In other words, it is more difficult to activate plastic deformation in a material with lower Poisson's ratio. For comparison, two additional lines are also plotted in Fig. 6.11 for the extreme cases where Poisson's ratio is either $v\to0.5$ or $v=0$. When $v\to0.5$, $\phi\to0$, resulting in a line parallel to the p-axis in the p-z plane. Thus, the shear strength of the

material is independent of the value of pressure. Therefore, the lines parallel to the p-axis are actually the failure surfaces in the incompressible plasticity theory in which plastic flow is the dominant mechanism. Also, it should be noted that the lateral confining stress induced by the axial loading in a uniaxial strain experiment is the same as the axial stress when $\nu \rightarrow 0.5$. At the other extreme, when $\nu=0$, $\phi=56.3°$, and $|\tau|=1.5p+\tau_0$, corresponding to a value of $\alpha=1.5$ with the friction coefficient $\mu \rightarrow \infty$ as discussed in the last section. In this situation, higher shear stress is required to fail the specimen in the presence of pressure. Also, there is no lateral stress induced by axial loading even in uniaxial strain experiments. The conditions of uniaxial stress and uniaxial strain are exactly the same in this case where transverse stress is zero for both. Since brittle materials will fail by axial splitting under uniaxial stress condition, it is expected that a ceramic material with very low Poisson's ratio will fail in a brittle manner even under uniaxial strain loading. Also, the initial failure mode is expected to be similar to that observed under uniaxial stress, i.e., axial splitting.

Table 6.1. Elastic and strength properties of ceramics.

Material	E (GPa)*	ν*	p_s (GPa)	τ_s (GPa)	p_h (GPa)	τ_h (GPa)
TiB$_2$	523	.05	0.17	0.21	5.71	7.34
SiO$_2$	90	.08	0.037	0.043	3.13	3.65
SiC	434	.16	0.16	0.14	7.13	6.27
B$_4$C	462	.17	0.21	0.18	8.45	7.16
WC	627	.21	1.40	1.01	2.55	1.84
AlN	321	.24	0.30	0.19	4.35	2.74
Al$_2$O$_3$	401	.24	0.35	0.22	6.25	3.93
ZrO$_2$	218	.31	1.08	0.44	9.18	3.99

* After Grady (1995).

6.3.1.2 Brittle versus Ductile Response at High Pressures

It is interesting to note that elasticity theory also predicts the increase in theoretical yield strength with the decrease in Poisson's ratio. The shear modulus G can be expressed in terms of Young's modulus E and Poisson's ratio v in elasticity:

$$G = \frac{E}{2(1 + v)} \qquad (6.15)$$

The shear strength τ_y of a material is a fraction of the shear modulus G, i.e.,

$$\tau_y = \frac{G}{M} = \frac{E}{2M(1 + v)} \qquad (6.16)$$

where M is a large scalar whose value is in the order of 100-1,000. It is clear from the inspection of Eqn. (6.16) that the materials with higher Poisson's ratio values will have lower shear strengths, indicating that plastic deformation may be activated if Schmid's law (Schmid and Boas, 1935) for flow on favorably oriented slip systems is obtained. On the other hand, if the Poisson's ratio of a material is low, the shear strength will be relatively high. In this case, the material will fail by cracking before the shear strength is reached even under uniaxial strain condition in experiments such as plate impact loading.

The Poisson's ratio of engineering ceramic materials with low spall strength lies between extreme values of v (0 and 0.5). In fact, the Poisson's ratio for most ceramics is less than 0.25 as mentioned earlier. The lateral confinement induced during the axial loading through Poisson's ratio during a uniaxial strain experiment increases with the increase in Poisson's ratio. Thus, the associated failure mode is expected to change from

complete brittle failure with $v=0$, to pressure insensitive plastic flow with large values of v which induces high confining pressure. A small spall strength is an indication that the material is very brittle in tension, and the tensile strength is dominated by the propagation of a single dominant flaw in the material. On the other hand, a large spall strength, which implies a high fracture toughness (Grady, 1995), indicates that the propagation of the crack may not be brittle even though the material itself maybe categorized as brittle such as WC and ZrO_2 (Rowcliffe *et al.*, 1988 and Cutler *et al.*, 1992). For the materials with large spall strengths, the failure process during a uniaxial strain experiment is expected to deviate from the brittle behavior proposed above, as indicated by the anomalous behavior of WC and ZrO_2 illustrated in Fig. 6.11.

Another parameter referred to as ductility, A, was proposed by Horii and Nemat-Nasser (1986) as an indication of material failure behavior in terms of the degree of brittleness under quasi-static loading conditions. The ductility was defined as

$$\Delta = \frac{K_c}{\tau_y (\pi a)^{1/2}} \tag{6.17}$$

where K_c is the fracture toughness and τ_y is the shear strength of the material, and a is the half length of the pre-existing crack shown in Fig. 6.1. When a microcrack starts to grow under local tensile stress, $K_I = K_{Ic} = K_c$ (Horii and Nemat-Nasser, 1986). The higher the value of A, the more ductile the material.

Under dynamic loading conditions, the fracture toughness can be calculated from the surface energy Γ which is measured in the spall experiments. The shear stress at HEL, τ_{HEL} can be used as yield strength. From fracture mechanics, the fracture toughness is converted from surface energy using the formula

$$K_{Ic} = \begin{cases} \sqrt{2E\Gamma} & \text{for } 1-D \text{ stress} \\ \\ \sqrt{\dfrac{2E\Gamma}{1-v^2}} & \text{for } 1-D \text{ strain} \end{cases} \tag{6.18}$$

where E is the Young's modulus and v is the Poisson's ration of the material. Since v^2 is a small value compared to 1.0 for most ceramic materials, only $K_{Ic} = \sqrt{2E\Gamma}$ will be used in the calculations. Grady (1995) reported Γ and HEL data for a variety of ceramic materials. Table 6.2 lists the values of the "ductility" for ceramics calculated from Grady's data. The flow size is taken to be a=3 μm in the calculations, which is a typical average grain size of engineering ceramics.

Since $K_{Ic} \propto \sigma_c \sqrt{\pi a}$ as indicated by Eqn. (6.9) where σ_c is the uniaxial compressive failure strength of the material, the parameter defined by

$$\Lambda = \frac{\sigma_c}{\tau_{HEL}} \tag{6.19}$$

appears to be equivalent to the ductility parameter A defined in Eqn. (6.17). However, the parameter A is much easier to be measured experimentally, since σ_c is much easier to measure than K_{Ic}, and flaw size "a" is not involved in Eqn. (6.19). The values of A for various ceramics are also listed in Table 6.2.

Table 6.2. Ductility of ceramics.

Material	E*, GPa	Γ*, J/m²	K_{Ic}, MPa·m$^{1/2}$	τ_{HEL}*, GPa	A	σ_c, GPa	A
TiB$_2$	523	27	5.3	7.34	0.23	4.97[a]	0.67
SiO$_2$	90	9.5	1.3	3.65	0.12	2.0[b]	0.54
SiC	434	12	3.2	6.27	0.17	2.75[b]	0.42
B$_4$C	462	31.5	5.4	7.16	0.24	2.4[b]	0.32
WC	627	667.5	28.9	1.84	5.11	5.3[b]	1.91
AlN	321	38	4.9	2.74	0.58	3.8[c]	1.25
Al$_2$O$_3$	401	38	5.5	3.93	0.46	2.07[d]	0.47
ZrO$_2$	218	970	20.6	3.99	1.68	2.84[e]	0.57

[*] Grady, 1995.

[a] Hoke, 1995.

[b] Goodfellow Ceramic Data Table, 1992.

[c] Dow Chemical Company Data Sheet, 1993.

[d] Coors Ceramics Company Data Sheet, 1991

[e] Richerson, 1992.

Since the values of σ_c listed in Table 6.2 are collected from a variety of sources, they may not exactly correspond to the materials used by Grady (1995). Therefore, the values of A listed in Table 6.2 should not be considered reliable. However, as listed in Table 6.2, both ductility parameters **A** and A show that WC and ZrO$_2$ are the most "ductile" ceramics listed in the table, followed by AlN and Al$_2$O$_3$. The rest of the ceramics listed are more brittle than the above four materials

6.3.1.3   Failure Mode

From the discussion above, it is clear that a low Poisson's ratio is an indication that plastic deformation in the material is difficult to activate over the entire range of stress states from one-dimensional stress to one-dimensional strain, provided the spall strength of the material is small compared to its HEL. The slope of the loading path will be close to the higher limit of 1.5 regardless of the stress state if the Poisson's ratio is very low. Figure 6.12 illustrates the effect of Poisson's ratio on the failure behavior of a brittle material under uniaxial strain loading. The uniaxial strain loading path of a material with a low Poisson's ratio will reach the failure surface of the intact material at a relatively low pressure as shown schematically in Fig. 6.12, which corresponds to the brittle failure of the material by axial splitting.

In impact related applications, the performance of the target material depends on the amount of energy it can absorb from the impactor. Complete brittle failure should thus be avoided. Based on the Poisson's ratio effect discussed earlier, it can be concluded that there are two approaches to avoid complete brittle failure upon impact. One approach is to use materials with high Poisson's ratio, and the other is to apply pressure on the brittle solids before or at the arrival of the axial loading, thereby providing artificial lateral confinement to suppress the tendency of crack nucleation and propagation. On the p-τ plane, this pressure can shift the loading path in the direction of higher pressure as shown in Fig. 6.12. Under the action of even moderate lateral confinement in AlN, the failure mode was observed to change from fragmentation by axial splitting to localized brittle faulting which absorbs a substantially larger amount of energy, as discussed in Chapter 5. A brittle-ductile transition was also observed on Macor under relatively high confinement as presented in Chapter 5.

If the stress state is uniaxial strain in an experiment below the HEL, the lateral stress σ_T induced by axial stress σ_A is proportional to the axial stress through the Poisson's ratio v before the HEL

$$\frac{\sigma_T}{\sigma_A} = \frac{v}{1-v}. \tag{6.20}$$

The variation of the ratio σ_T/σ_A as a function of v is plotted in Fig. 6.13 with v ranging from 0 to 0.5. It is clear that for small values of v, the values of σ_T/σ_A are also very small, such that the lateral stress induced by a given axial load is relatively small. For example, when $v < 0.1$, the ratio $\sigma_T / \sigma_A < 0.11$. In this situation, the lateral confinement induced by a compressive axial loading is less than 11% of the axial stress. In an experiment of dynamic uniaxial strain stress state, e.g., a plate impact experiment, the material with low Poisson's ratio is expected to initiate the failure process by axial cracking because the lateral confining pressure is not sufficient to completely suppress the tendency for crack initiation and propagation. The specimen is thus cracked into slender columns of irregular shapes, which are aligned roughly with the axial loading direction. The thin columns will collapse (buckle) when the axial loading is increased further. However, the collapse of the columns is restricted by the surrounding columns, and the columns cannot move freely in the lateral direction due to the inertial effects in a dynamic experiment. Thus, the failed columns are compacted in such a way that the broken pieces squeeze into each other in the lateral direction while axial dimension of the specimen continuously shortens. The compaction process therefore introduces lateral confinement of the broken pieces by the contact of the fracture surfaces inclined to the axial loading direction. The compaction may result in an unstable behavior of the material similar to the formation of faults observed in the confined AlN as shown in Figs. 5.22 and 5.23.

The mechanism of the generation of the confinement in the compacted material is completely different from the Poisson's ratio effect since the material has been damaged significantly. Due to the contact-induced confinement, the compacted specimen can still carry axial load. The load carrying capacity will depend on the amount of confinement. The strain rate is an important factor in determining the magnitude of the confinement since the lateral movement of the broken specimen is restricted by the inertial resistance. Another important factor affecting the lateral confinement is the amount of damage. As discussed earlier, the loading path will jump from the failure surface of the intact material to the damaged material failure surface corresponding to the appropriate value of the damage parameter. The amount of the jump in shear, and hence in transverse stress, depends on the damage as shown in Fig. 6.9. The value of the transverse stress is expected to be much larger than that in the intact material before failure and compaction if the damage is very high. At this deformation stage, the specimen consists of the broken chunks of material laterally confined by each other. If there is an unloading of the specimen at this stage of deformation, the specimen will fall apart completely due to the extensive damage. Therefore, following failure, a specimen under uniaxial strain deformation may be able to take further dynamic compressive loading, but the spall strength will be essentially zero.

The failure process described above may explain the anomalous behavior of TiB_2. The Poisson's ratio is 0.05 as listed in Table 6.1. The failure of the intact material and the post-failure load carrying capacity are considered to be responsible for the observed two wave structure in the shock wave of a uniaxial strain experiment evidenced as a small cusp at 5-6 GPa and a prominent cusp at 3-7 GPa which was assumed to be the HEL, Ewart and Dandekar, 1994. The material has no spall strength beyond the HEL because the intact specimen has been fragmented. The contact-induced confinement allows the material to continue to exhibit the shear strength beyond HEL. The brittle failure process

for low Poisson's ratio materials and the expected corresponding axial stress-strain relation are plotted in Fig. 6.14a. On the other hand, if the Poisson's ratio of the brittle material is relatively high, e.g., ν=0.25, the lateral confinement will be 33% of the axial loading under uniaxial strain deformation as shown in Fig. 6.13. Figure 6.14b shows the possible failure process without cracking and the expected corresponding stress-strain curve. The large lateral confining pressure induced by the axial loading thus could be large enough to suppress the crack initiation and propagation in the material. The specimen may deform plastically at sufficiently high loading levels.

A brittle-ductile transition under quasi-static loading conditions has been identified using hydraulic lateral confining pressure on engineering ceramics by Heard and Cline (1980). A brittle-ductile transition under dynamic loading conditions has also been identified on Macor confined by double concentric sleeves as stated in Chapter 5. In the shock wave loaded experiments on alumina (AD995) whose Poisson's ratio is 0.24, the spall strength is independent of the peak amplitude of the shock wave and is nearly a constant for a given impulse (Dandekar, 1994a) which indicates behavior similar to plastic flow. This also holds in shock amplitudes beyond HEL.

It is anticipated that a target made of high Poisson's ratio material will absorb larger amounts of energy from the impactor due to the plastic deformation. Low Poisson's ratio materials are also expected to be able to deform plastically provided the lateral confinement pressure is high enough. Since the amount of confinement pressure induced by the axial loading is small in materials with low Poisson's ratios, other forms of lateral confinement must be applied if plastic deformation is desired.

6.3.2 Failure Waves

The effect of Poisson's ratio discussed above may also be relevant in assessing the detectabilty of the failure wave in brittle material under shock wave loading. If the applied stress level is less than the Hugoniot elastic limit, it is expected that an elastic wave of finite amplitude will propagate in the brittle material. The recent experimental shock wave studies on K-2 glass by Kanel' et *al.* (1992) provided evidence for the propagation of a delayed front of fracture following the initial elastic compression wave. This new, and not yet well understood, phenomenon has been identified as a failure wave, and it is presumed to be a shear fracture process which is driven by the large shear strain energy in the body behind the large-amplitude elastic uniaxial strain compression wave, see Grady (1995). Brar *et al.* (1991) embedded transverse stress gages in a soda-lime glass which recorded definitive evidence of a substantial increase in the transverse stress component upon passage of the failure wave front, thus significantly reducing the shear stress $\tau = \frac{1}{2}(\sigma_A - \sigma_T)$. Brar *et al.* also tested the tensile strength of the glass behind the initial elastic shock wave both in front and behind the failure wave through appropriate design of the spall experiments. These tests indicated a tensile strength in excess of **3 GPa** for glass in front of the failure wave and nearly zero strength behind it, suggesting a transition to fully comminuted material following passage of the failure wave. The characteristics of the failure wave described here coincides with the phenomenological description of the failure mechanism for brittle materials with low Poisson's ratio discussed earlier in this section. However, in the description above, the transverse stress was predicted to drop at failure followed immediately by a sudden rise, whereas only the sudden rise was detected in the experiments performed by Brar *et al.* (1991). Therefore, the failure wave may represent the failure process associated with a brittle material loaded by a shock wave

whose magnitude is below HEL but high enough to cause damage to initiate and propagate.

There inevitably exist various types of defects in the bulk of a brittle ceramic such as microcracks and grain boundaries. These pre-existing defects will create stress concentrations when loaded. Upon the passage of the loading shock wave front, the deviatoric component of the dynamic stress will cause damage to initiate and propagate. A finite period of time is necessary for these micro-defects to grow to a significant size sufficient to be detected by experimental instruments. Therefore, the detectable failure front is expected to travel at the same speed as the shock wave but a finite distance behind the loading shock wave. Kanel' *et al.* (1992) suggested that the failure wave may be a propagating fracture front trailing the initial elastic shock wave at a velocity substantially less than the shock velocity. Raiser *et al.* (1995) proposed a failure wave velocity closer to the Rayleigh wave speed, although evidence for this prediction is not convincing. Based on the failure mechanism for brittle materials described earlier in this section, it can be expected that failure wave front will travel at shock wave speed and at a finite distance or finite time behind the shock wave front. Also, it is expected that the failure wave is more likely to be detected in a brittle ceramic with a low Poisson's ratio, because failure waves may not occur at all in a high Poisson's ratio material in a uniaxial strain shock wave loading since the material will deform in a manner similar to plastic flow instead of comminuting. Recently, Bourne *et al.* (1994) have presented a systematic study of failure waves in glasses through high speed photography. Their study confirmed the existence of a failure wave in soda-lime glass (Brar *et al.*, 1991), but the failure waves are absent in pyrex glass.

6.4   The Limitations of the Model

The validity of the failure/flow criterion proposed in this section has been demonstrated in its ability to explain some current and previous experimental observations concerning the behavior of ceramics. This model provides a possible unified framework under which the experimental results on ceramic materials obtained using various experimental techniques may be properly interpreted. However, the limitations on the applicability of the model should be thoroughly understood. Careful inspection of the construction of the failure criterion indicates that attention should be paid to the following aspects when applying the failure criterion.

(1) Existence of the Failure Surface.

Stable crack propagation under quasi-static compressive loading may ensure the existence of a compressive failure criterion, since a population of small cracks extends stably under compression. Each of the cracks grows longer as the stress is raised, until they interact in some cooperative way to give final failure (Ashby and Sammis, 1990). In the case of dynamic loading conditions, the stability of dynamic crack propagation under overall compressive loading needs to be studied. The stability could be affected by the inertia, the boundary conditions, the reflected and unloading waves, the geometry, etc. The failure surface can exist only when the dynamic microcrack propagation under compressive loading can be proved to be stable, such that the cracks will stop propagating when the load level is not increasing.

(2) Appropriate Choice of the Failure Surface.

It was pointed out earlier that the failure surface constructed from the available experimental data is applicable only for undamaged or intact materials because the strength data were obtained for the intact materials. For damaged materials, a damage parameter, which cannot be isotropic as described earlier in this chapter, should be properly defined. A series of failure surfaces characterized by the damage parameter can then be constructed based on the degree of damage. These additional failure surfaces are important in governing the post-failure behavior of the material. It is interesting to note that after sufficiently high loads, ceramics will be comminuted upon load reversal which alters dramatically the material properties, whereas the flow behavior of ductile materials will be affected by reversal loading only by the Bauschinger effect.

(3) Effect of Spall Strength.

As mentioned earlier in this chapter, the failure criterion and its dependence on Poisson's ratio are only suitable for brittle materials with low spall strength. If the spall strength of a material is high such as WC and ZrO_2, the failure mechanism will differ from that discussed in this chapter.

6.5   Conclusions

Based on the experimental results on AlN together with available data in the literature, a failure/flow criterion is provided for ceramics under high pressure loading. This model provides a possible unified framework under which the experimental results on ceramic materials from various experimental techniques may be properly interpreted. Mohr-Coulomb criterion and Johnson-Holmquist model were found to fit the experimental data for brittle failure at low pressures, whereas the materials deformed in a manner similar to pressure insensitive plastic flow at high pressures. The failure/flow criterion, together with the failure mechanisms for brittle materials, was used to rationalize the experimental observations made in the shock wave loading and other types of experiments. The effect of various material properties on the failure behavior was investigated based on the failure criterion. It was shown that the Poisson's ratio plays an important role in the underlying explanations of observed behavior. A lower value of Poisson's ratio may indicate that plastic flow is difficult to activate even under uniaxial strain loading, and hence failure could occur in a brittle manner. Materials with higher Poisson's ratio are expected to deform plastically under impact loading of high amplitude (above HEL). The operational region enveloped by the failure surface decreases as the damage in the material increases. The present model may be applicable only to ceramic materials with low spall strengths.

6.6 References

Ahrens, T. J., Gust, W. H. and Royce, E. B., (1968), "Material Strength Effect in the Shock Compression of Alumina," Journal of Applied Physics, 39, pp. 4610-4616.

Ashby, M. F. and Hallam, S. D., (1986), "The Failure of Brittle Solids Containing Small Cracks under Compressive Stress States," *Acta Metall*. 34, pp. 497-510.

Ashby, M. F. and Sammis, C. G., (1990), "The Damage Mechanics of Brittle Solids in Compression," *PAGEOPH*, 133, (3), pp. 489-521.

Bourne, N. K., Rosenberg, Z., Mebar, Y., Obara, T. and Field, J. E., (1994), "A High-Speed Photographic Study of Fracture Wave Propagation in Glass," Journal de Physique, IV, Colloque C8, pp. 635-640.

Brar, N. S., Bless, S. J. and Rosenberg, Z., (1991), "Impact-Induced Failure Waves in Glass Bars and Plates," Applied Physics Letters, 59, pp. 3396-3398.

Cutler, R. A., Reynolds, J. R. and Jones, A., (1992), "Sintering and Characterization of Polycrystalline Monoclinic, Tetragonal, and Cubic Zeconia," Journal of the American Ceramic Society, 75, pp. 2173-2183.

Dandekar, D. P. and Benfanti, D. C., (1993), "Strength of Titanium Diboride Under Shock-Wave Loading," Journal *of Applied* Physics, 73, pp. 673-679.

Dandekar, D. P., Abbate, A. and Frankel, J., (1994), "Equation of State of Aluminum Nitride and Its Shock Response," *Journal of* Applied Physics, 76 (7), pp. 4077-4085.

Dandekar, D. P., (1994a), "Response of Ceramics Under Shock Wave Loading," in High Pressure Science and *Technology-1993*, edited by Schmidt, S. C., Shaner, J. W., Samara, G. A. and Ross, M., American Institute of Physics, pp. 729-732.

Dandekar, D. P., (1994b), "Shear Strengths of Aluminum Nitride and Titanium Diboride Under Plane Shock Wave Compression," Journal de Physique, IV, Colloque C8, pp. 379-384.

Drucker, D. C. and Prager, W., (1952), "Soil Mechanics and Plastic Analysis or Limit Design," Quarterly of Applied Mathematics, 10, pp. 157-165.

Ewart, L. and Dandekar, D. P., (1994), "Relationship Between the Shock Response and Microstructural Features of Titanium Diboride (TiB$_2$)," in High Pressure Science and *Technology-1993*, edited by Schmidt, S. C., Shaner, J. W., Samara, G. A. and Ross, M., American Institute of Physics, pp. 1201-1204.

Gilat, A. and Chengalva, M. K., "High-Strain-Rate Characterization of Ceramics in Shear," (1992), in Shock-Wave and High-Strain-Rate Phenomena in Materials, edited by Meyers, M. A., Murr, L. E. and Staudhammer, K. P., Marcel Dekker, Inc., pp. 1069-1073.

Grady, D. E., (1995), "Dynamic Properties of Ceramic Materials," Sandia Report SAND94-3266, Sandia National Laboratories, Albuquerque, NM.

Heard, H. C. and Cline, C. F., (1980), "Mechanical Behavior of Polycrystalline BeO, Al_2O_3 and AlN at High Pressure," *Journal of Materials Science, 15,* pp. 1889-1897.

Hoke, D. A., (1995), "Reaction Synthesis, Densification, and Mechanical Behavior of Titanium Diboride," Ph.D. Thesis, University of California, San Diego.

Holmquist, T. J., Johnson, G. R., Grady, D. E., Lopatin, C. M., and Hertel, Jr., E. S., (1995), "High Strain Rate Properties and Constitutive Modeling of Glass," in *Proceedings of the 15th International Symposium on Ballistics,* Jerusalem, Israel, May 21-24, in press.

Horii, H. and Nemat-Nessar, S., (1986), "Brittle Failure in Compression: Splitting, Faulting and Brittle-Ductile Transition," *Phil. Trans. Roy. Soc. London,* **A319**, pp. 337-374.

Jaeger, J. C. and Cook, N. G. W., (1979), <u>Fundamentals of Rock Mechanics</u>, Chapman and Hall, p. 95.

Johnson, G. R. and Holmquist, T., J., (1994), "An Improved Computational Model for Brittle Materials," in *High Pressure Science and Technology*-1993, edited by Schmidt, S. C., Shaner, J. W., Samara, G. A. and Ross, M., American Institute of Physics, pp. 981-984.

Kanel', G. I., Rosorenov, S. V. and Fortov, V. E., (1992), "The Failure Waves and Spallations in Homogeneous Brittle Materials," in *Shock Compression of*

Condensed Matter-1991, edited by Schmidt, S. C., Dick, R. D., Forbes, J. W., and Tasker, D. G., Elsevier Science Publishing, pp. 451-454.

Kipp, M. E. and Grady, D. E., (1989), "Shock Compression and Release in High-Strength Ceramics," Sandia Report SAND89-1461, Sandia National Laboratories, Albuquerque, NM.

Kipp, M. E. and Grady, D. E., (1994), "Shock Phase Transformation and Release Properties of Aluminum Nitride," Journal de Physique, IV, Colloque C8, pp. 249-256.

Klopp, R. W. and Shockey, D. A., (1991), "The Strength Behavior of Granulated Silicon Carbide at High Strain Rate and Confining Pressure", Journal of *Applied* Physics, 70, pp. 7318-7326.

Longy, F. and Cagnoux, J., (1989), "Plasticity and Microcracking in Shock-Loaded Alumina," Journal of the American Ceramic Society, 72, pp. 971-979.

Murrel, S. A. F., (1963), "A Criterion for Brittle Fracture of Rocks and Concrete under Tri-axial Stress and the Effect of Pore Pressure on the Criterion," in Rock Mechanics, Edited by Fairhurst, C., Oxford, Pergaman, pp. 563-577.

Raiser, G. V., Wise, J. L., Clifton, R. J., Grady, D. E., and Cox, D. E., (1995), "Plate Impact Response of Ceramics and Glasses," *Journal of Applied* Physics, in press.

Rajendran, A. M., (1992), "High Strain Rate Behavior of Metals, Ceramics and Concrete," WL-TR-92-4006, Wright-Patterson Air Force Base, Dayton, OH.

Richerson, D. A., (1992), <u>Modem Ceramic Engineering</u>, 2nd edition, Marcel Dekker, Inc., New York.

Rosenberg, Z., Brar, N. S. and Bless, S. J., (1991), "Dynamic High-pressure Properties of AlN Ceramic as Determined by Flyer Plate Impact," Journal of Applied Physics, **70,** pp. 167-169.

Rosenberg, Z., Brar, N. S. and Bless, S. J., (1992), "Shear Strength of Titanium Diboride Under Shock Loading Measured by Transverse Manganin Gages," in Shock *Condensed Matter-1991*, edited by Schmidt, S. C., Dick, R. D., Forbes, J. W. and Tasker, D. G., Elsevier, Amsterdam, pp. 471-473.

Rosenberg, Z., (1993), "On the Relation Between the Hugoniot Elastic Limit and the Yield Strength of Brittle Materials," Journal of Applied Physics, **74,** pp. 752-753.

Rowcliffe, D. J., Jayaram, V., Hibbs, M. K. and Sinclair, R. (1988), "Compressive Deformation and Fracture in WC Materials," Materials *Science* and Engineering, **106,** pp. 299-303.

Sairam, S. and Clifton, R. J., (1994), "Pressure-Shear Impact Investigation of Dynamic Fragmentation and Flow of Ceramics," in Mechanical Testing of Ceramics *and* Ceramic Composites, AMD<u>197</u>, ASME, edited by Gilat, A, pp. 23-40.

Schmid, E. and Boas, W., (1935), <u>Kristallplastizitat</u>, Springer-Verlag, Berlin.

Subhash, G. and Nemat-Nasser, S., (1993), "Dynamic Stress Induced Transformation and Fracture Formation of Zirconia Ceramics," *Journal of* the *American Ceramic Society*, **76,** pp. 153-165.

Tranchet, J.-Y., (1994), "**A** Plasticity Model for the Shock-Wave Behavior of Pure Aluminas," *Journal de* Physique, IV, Colloque C8, pp. 289-294.
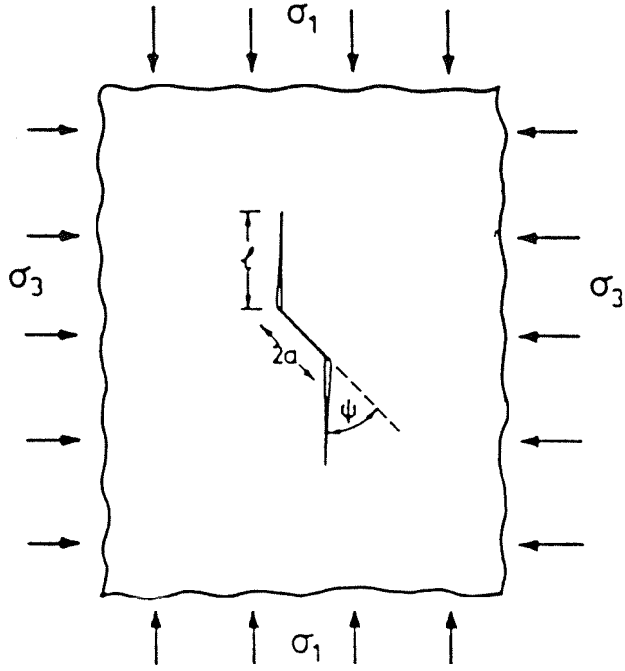
Figure 6.1 A schematic illustration of a sliding crack model.
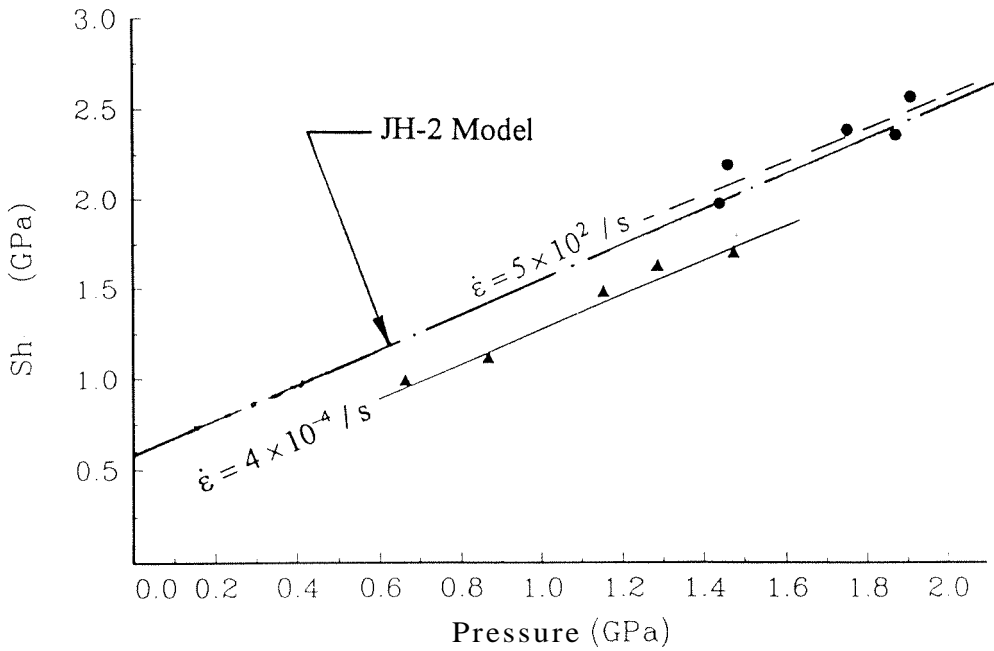
Figure 6.2 Variation of maximum shear strength of AIN with pressure under quasi-static and dynamic loading conditions.
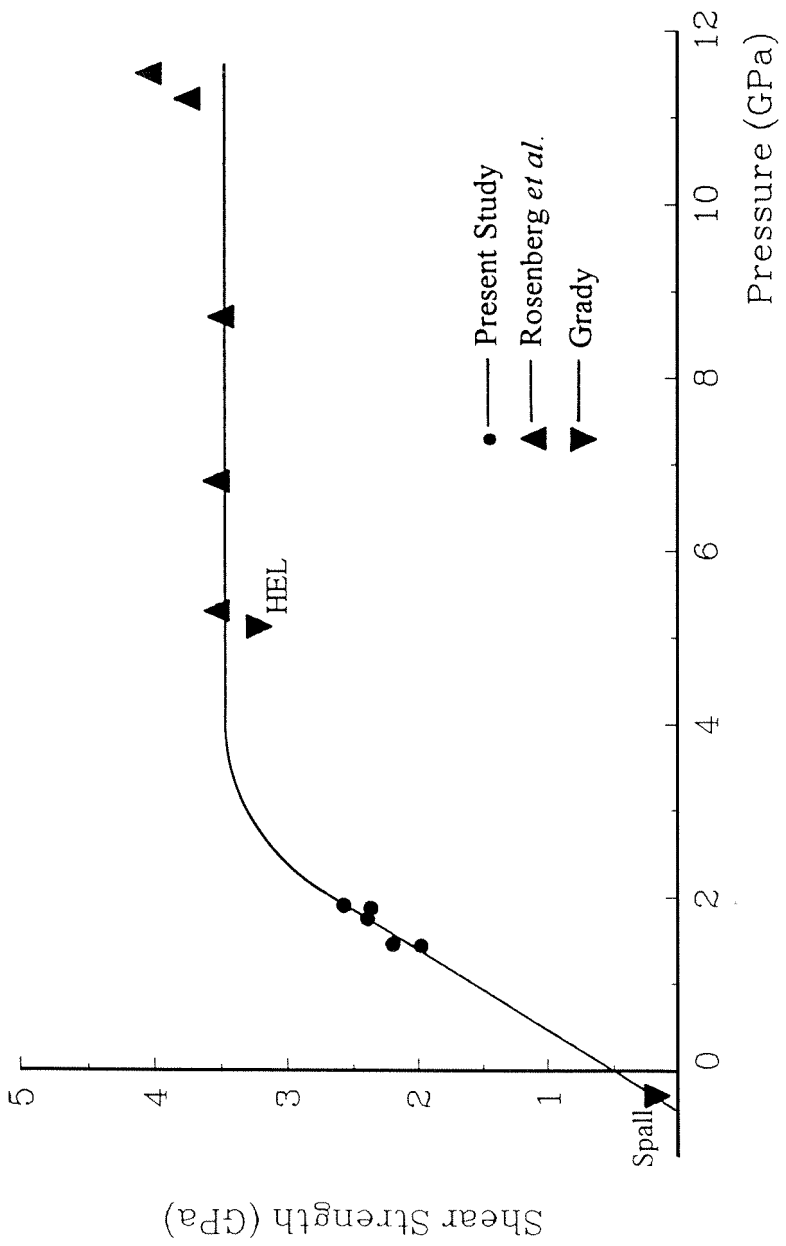
Figure 6.3 The failure surface of AlN under dynamic loading.
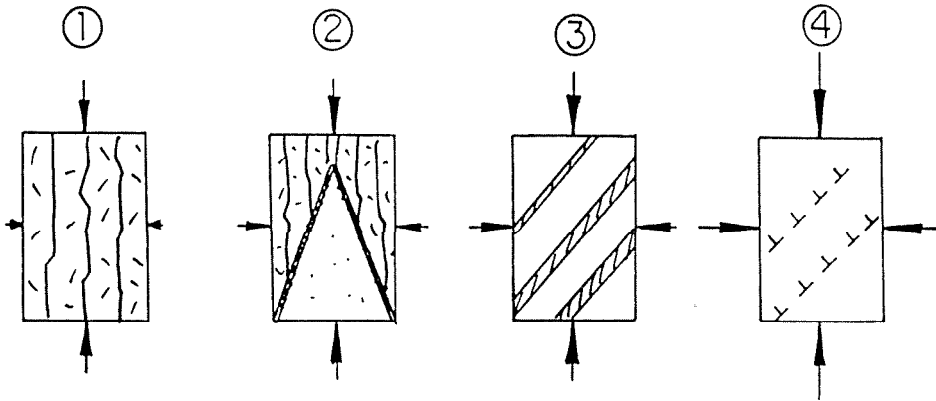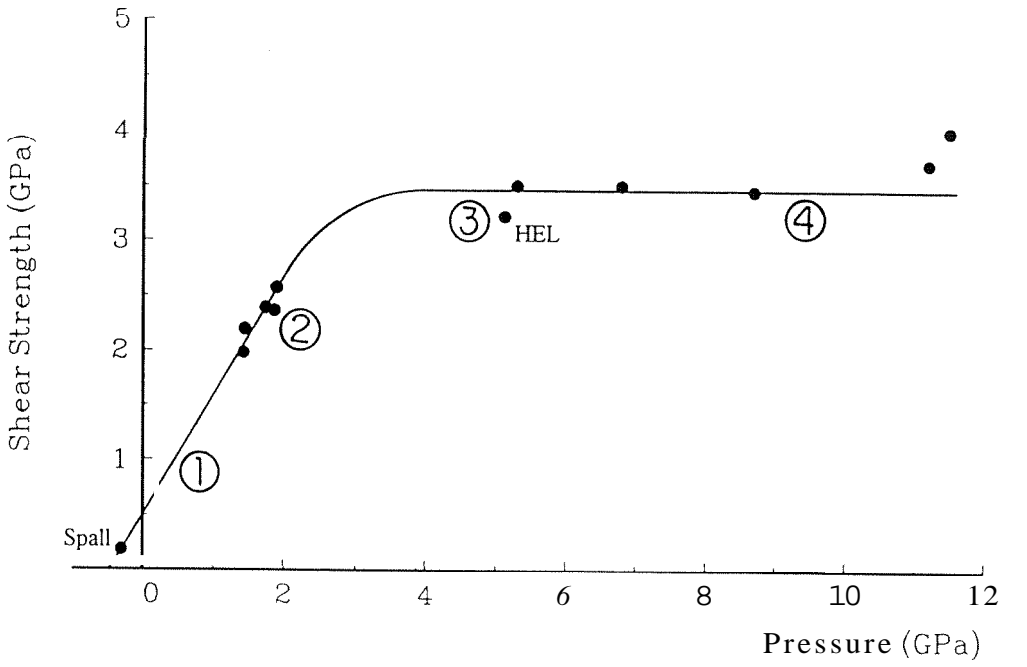
Figure 6.4 Variation of failure mode with the stress state at failure.
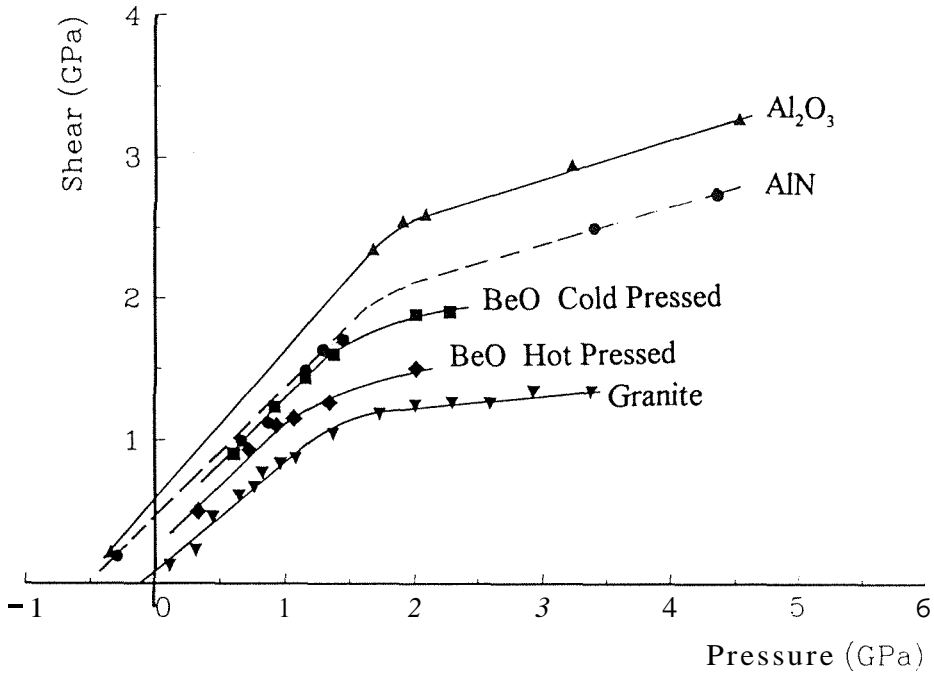
Figure 6.5 The failure surfaces of some brittle materials on the p-τ plane.
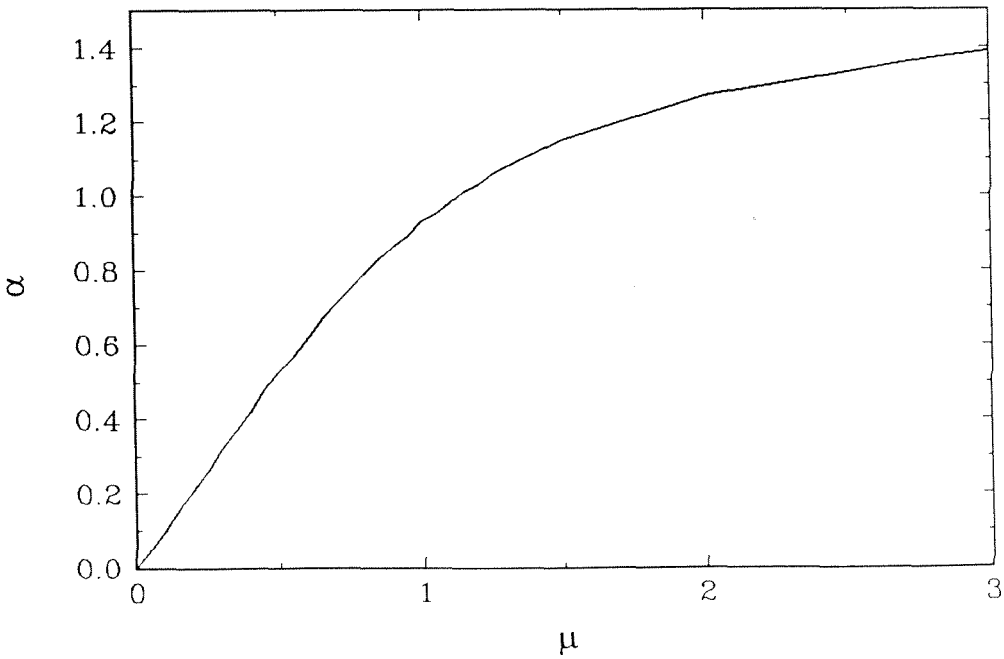
Figure 6.6 Variation of slope a with friction coefficient μ.
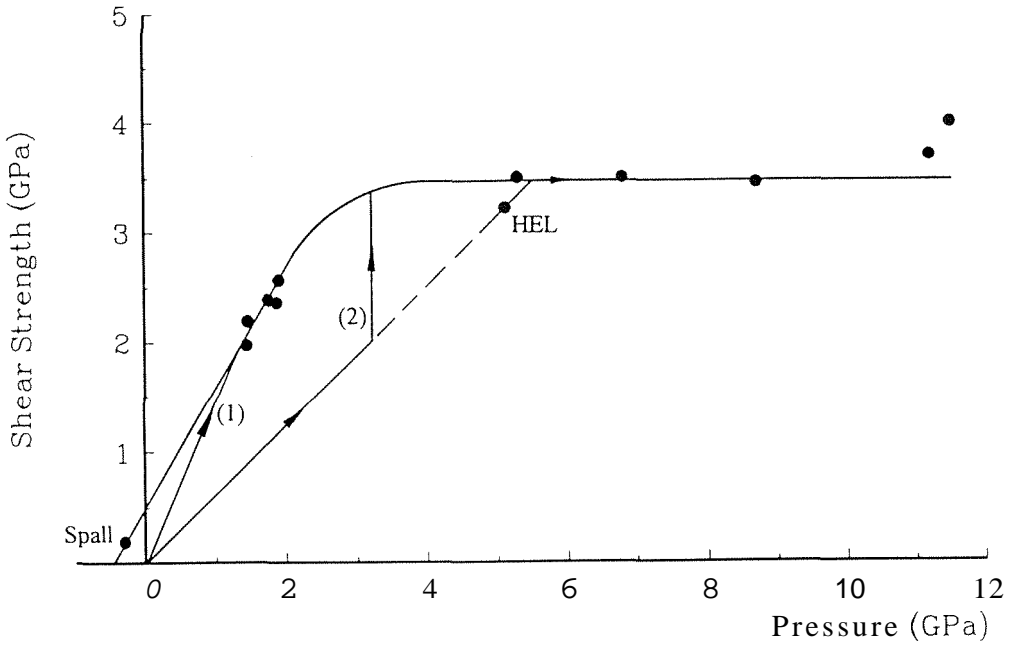
Figure 6.7 Loading path and operational region under the failure surface.
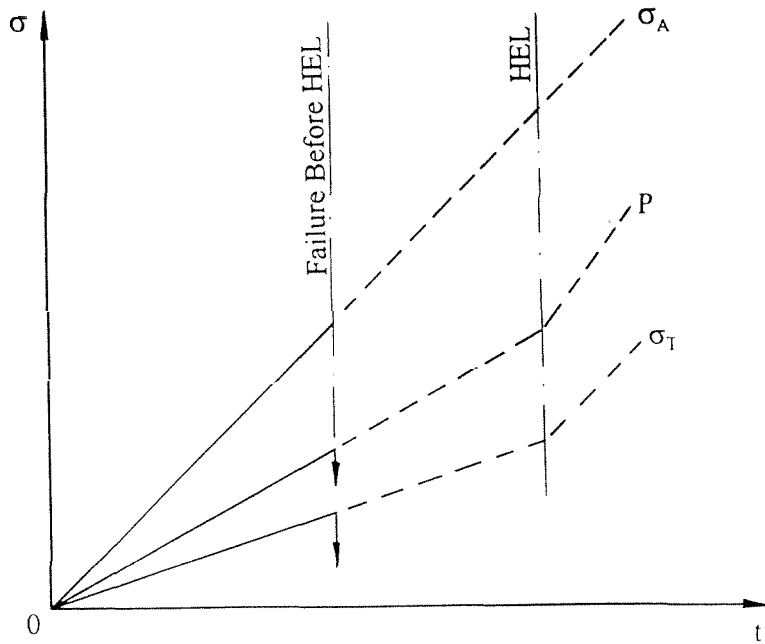
Figure 6.8 Expected stress variation with time in a uniaxial experiment.
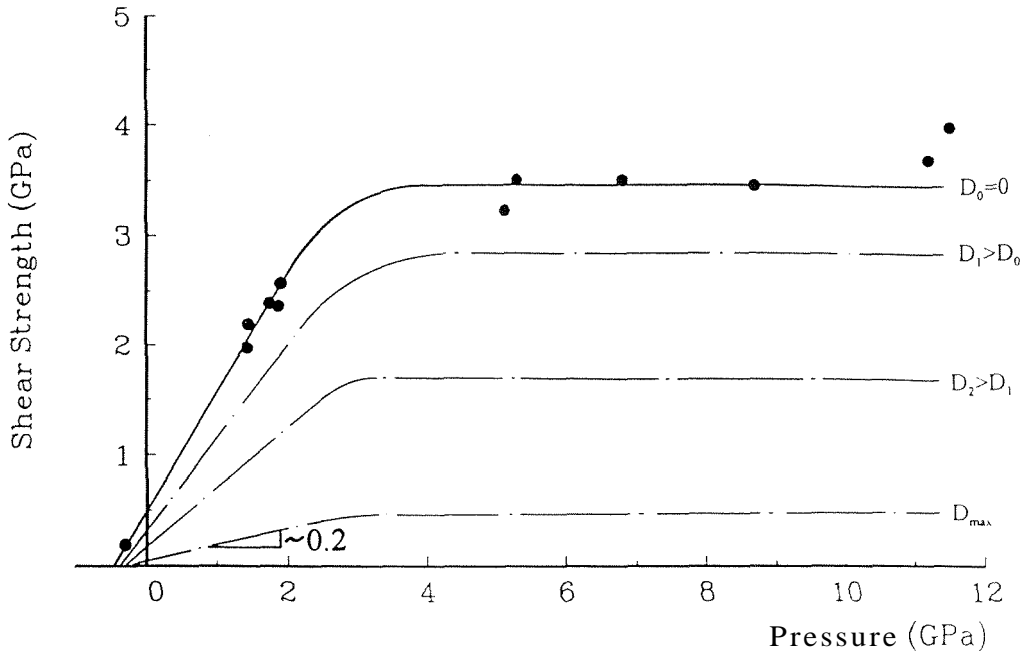
Figure 6.9 Effect of damage on the failure surface for brittle materials.
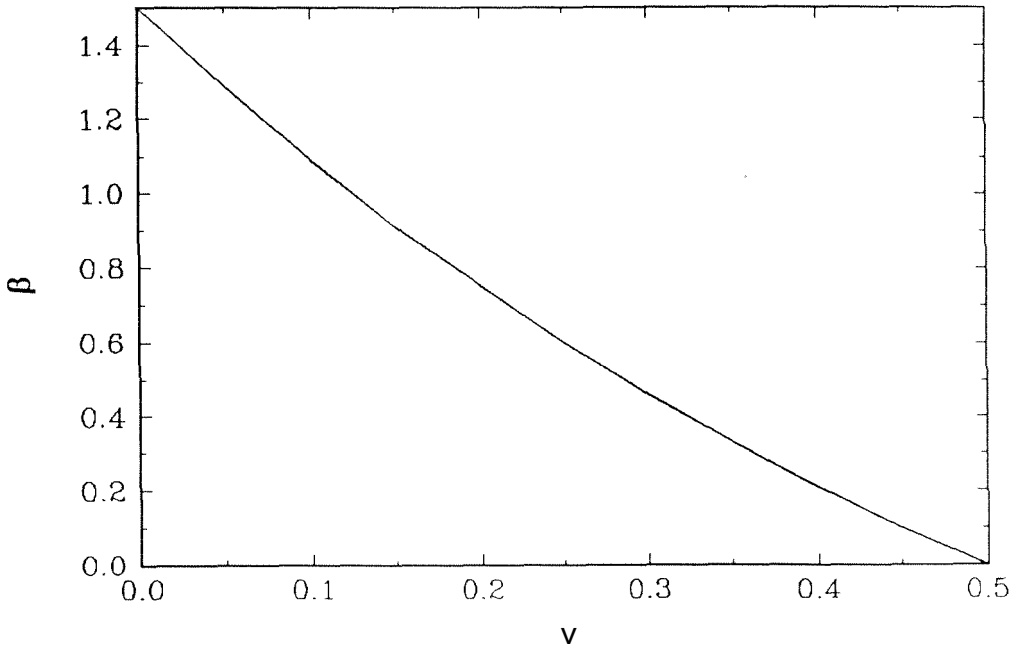
Figure 6.10 Variation of the lower bound failure surface slope with Poisson's ratio.
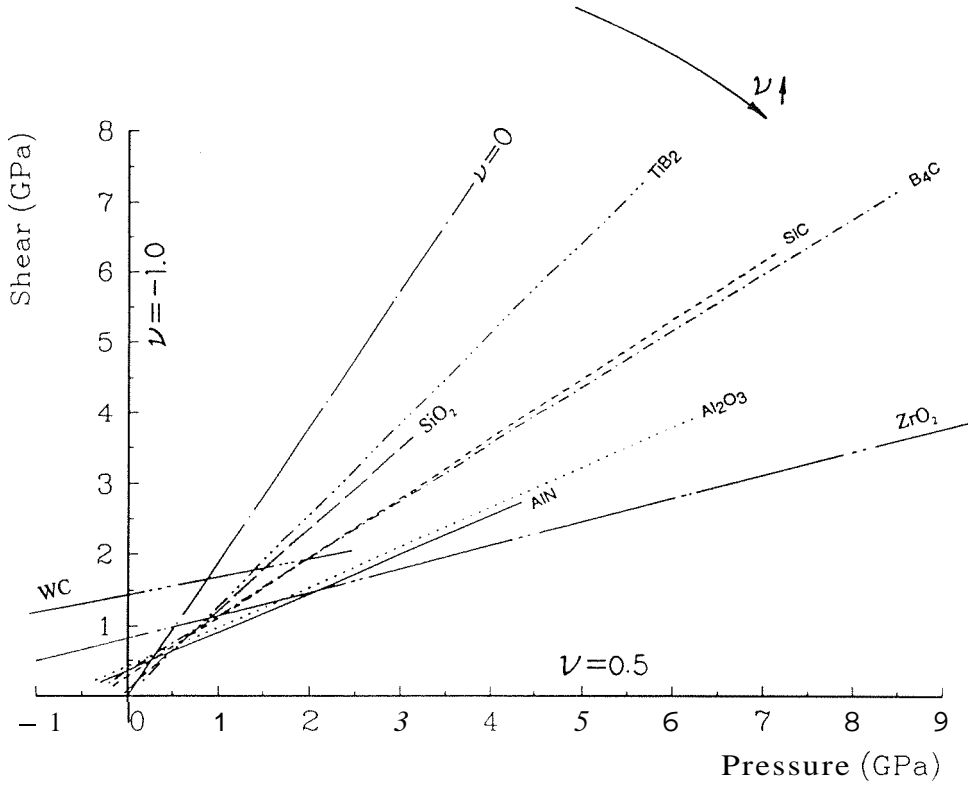
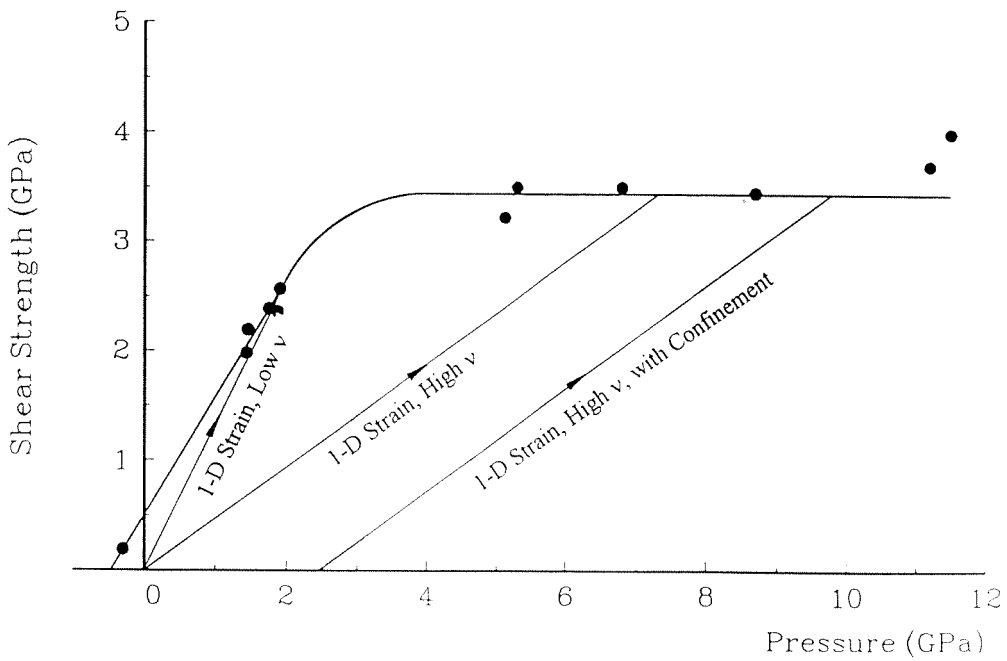**Figure 6.11 Variation of the lower bound failure surface with Poisson's ratio.**

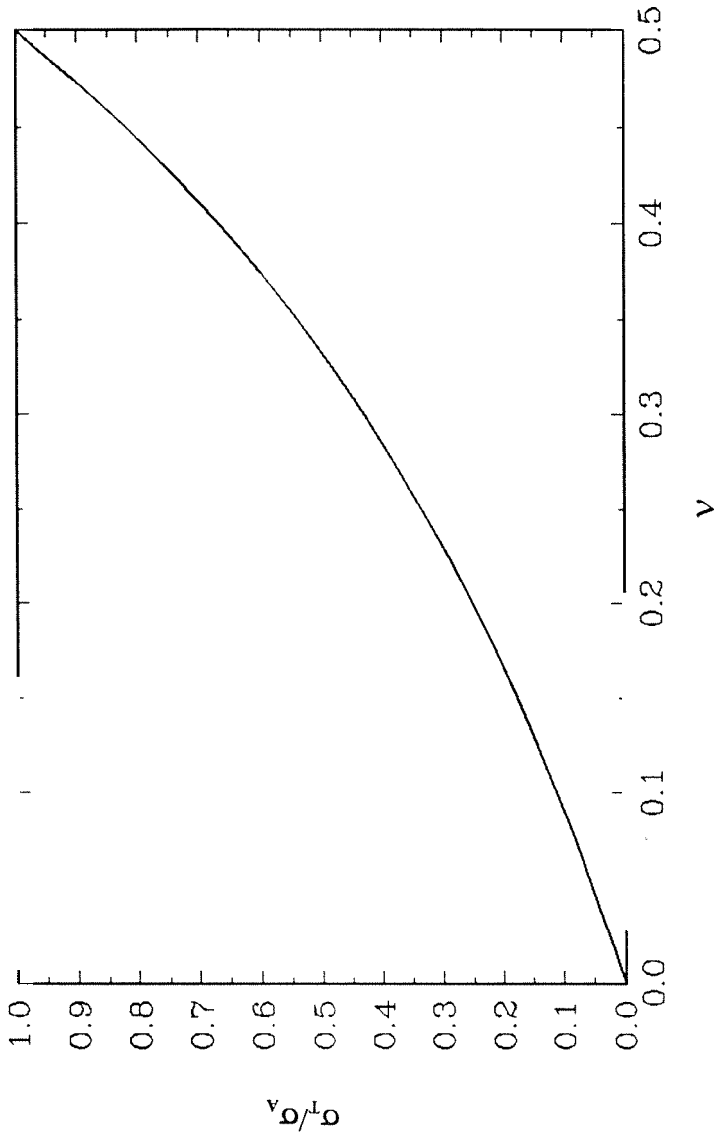**Figure 6.12 The effect of Poisson's ratio and pre-stress on the loading path.**
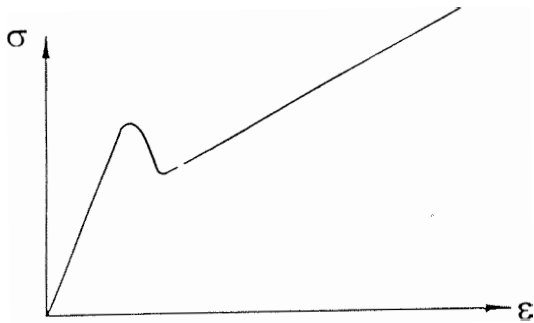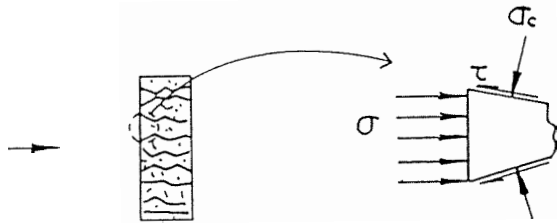
Figure 6.13 Variation of σ_T/σ_A with ν in uniaxial strain compression.
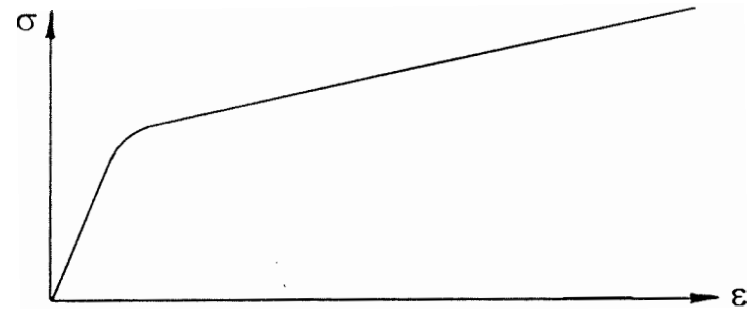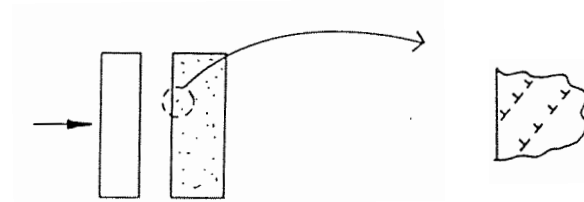
Figure 6.14 Effect of Poisson's ratio on the stress-strain behavior under uniaxial strain loading.

Chapter 7

Summary and Future Work

7.1   Summary

An experimental technique has been developed that is capable of (1) dynamically loading the specimen in multiaxial compression; (2) controlling the stress state in the specimen in the range from uniaxial stress to uniaxial strain; and (**3**) allowing the recovery of the sample after loading by a single, well defined pulse for characterization of the failure mode. In this technique, cylindrical ceramic specimens were loaded in the axial direction using a split Hopkinson (Kolsky) pressure bar modified to apply a single loading pulse, and were confined laterally either by shrink fit sleeves, or by eletro-magnetic force. The plastically deformed metal sleeves retained the tested specimens for failure mode characterization and were used under both quasi-static and dynamic axial loading conditions, whereas the electro-magnetic confinement was an ideal approach to apply dynamic proportional loading.   However, before it can be used to do extensive experimental research on engineering ceramics, the current experimental technique of applying electro-magnetic confinement needs major improvements to reduce electrical noise, measure strain accurately and increase the confinement pressure.

Quasi-static and dynamic multiaxial compression experiments have been performed on a machinable glass ceramic, Macor, and a monolithic poiycrystalline engineering ceramic, sintered aluminum nitride (AIN).   The cylindrical ceramic specimens were confined laterally by shrink fit sleeves: the amount of confining pressure (0-230 MPa) was varied by using different sleeve materials. The quasi-static axial load was applied by a hydraulic driven Material Test System (MTS), whereas the dynamic axial load was

provided by a modified split Hopkinson pressure bar (SHPB). For both materials under both quasi-static and dynamic loading conditions, the experimental results showed that the failure mode changed from fragmentation by axial splitting under conditions of uniaxial stress to localized deformation on faults under moderate lateral confinement. The fault initiation process was studied experimentally in detail under moderate confinement. Based on the experimental results, a compressive failure mechanism was proposed for brittle materials under moderate lateral confinement. A transition from brittle to ductile behavior was observed for the first time in Macor under high confinement pressure which was achieved using a second sleeve around the inner sleeve. The compressive failure strengths of both materials increased with increasing confinement pressure under both quasi-static and dynamic loading conditions. The highest dynamic compressive strengths of Macor and AlN measured in the experiments were 1.35 GPa and 5.40 GPa, respectively, whereas their quasi-static compressive strength were measured to be 0.43 GPa and 2.5 GPa, respectively.

Based on the experimental results on AlN together with available data in the literature, a failure/flow criterion was developed for ceramic materials under multiaxial loading. The Mohr-Coulomb criterion and the improved Johnson-Holmquist model were found to fit the experimental data for brittle failure at low pressures, whereas the materials exhibited pressure insensitive plastic flow at high pressures. Experimental observations made in shock wave loading and other types of experiments were rationalized based on the postulated failure mechanisms and the possibility of plastic flow beyond HEL. The effect of various material properties on the failure behavior was investigated using the proposed failure criterion. The applicability of the present model to a range of ceramics was also explored and the limitations of the model were outlined.

7.2 Future Work

This dissertation represents the first thorough experimental investigation into the dynamic failure behavior of ceramic materials under multiaxial compression. However, additional work is required for a complete understanding of the mechanical behavior of ceramics under various dynamic loading conditions. The following issues should be addressed in future work.

(1) Existence of a Failure Surface

As mentioned in Chapter 6, stable crack propagation under quasi-static compressive loading may ensure the existence of a compressive failure criterion. In the case of dynamic loading conditions, the stability of dynamic crack propagation under overall compressive loading is not well understood and thus needs to be studied. The stability could be affected in part by the inertia, the boundary conditions, the reflected waves, the unloading waves, and the geometry. The failure surface can exist only if the dynamic microcrack propagation under compressive loading is stable, such that the cracks will stop propagating when the load level is not increasing. The kinetics of damage accumulation needs to be studied in further detail.

(2) Effect of Spall Strength on the Failure Mechanism

As mentioned in Chapter 6, the failure criterion and its dependence on Poisson's ratio are only suitable for brittle materials with low spall strength. If the spall strength of a ceramic is high such as in WC and ZrO_2, the failure mechanism will differ from that discussed in Chapter 6. In that case, the failure criterion may not be applicable, and further research is necessary to determine the failure behavior of ceramics with high spall strength.

(**3**) Effect of Strain Rate on the Failure Surface

In the brittle failure region of the failure surface introduced in Chapter 6, the effect of strain rate on the failure surface was clear from experimental results and the Mohr-Coulomb failure criterion and the improved Johnson-Hoimquist model. However, in the region where pressure is near or over the brittle-ductile transition, the effect of strain rate is not understood due to the lack of both experimental evidence and theoretical models. Controlled experiments are needed to establish the effect of strain rate on the behavior of ceramics beyond their brittle-ductile transition.

(4) Role of Poisson's Ratio

The Poisson's ratio appears to play an important role in the explanation of the observed ceramic material behavior under shock wave loading as discussed in Chapter 6. **A** lower value of Poisson's ratio indicates that the plastic deformation is more difficult to activate even under uniaxial strain loading, and hence failure occurs in a brittle manner. Materials with higher Poisson's ratio may deform plastically under high magnitude impact loading. It is interesting to note that most ceramics have a Poisson's ratio greater than 0 and less than *0.25* and most metals have a Poisson's ratio higher than *0.25* and less than *0.5*. The factors which determine the value of the Poisson's ratio of a material and its relation to the degree of brittleness of a solid are not well understood.

(5) Damage Parameter: Loading and Unloading

It was pointed out that the failure surface constructed from the available experimental data was only for undamaged or intact materials since the strength data were obtained from the intact materials. For damaged materials, a damage parameter, which cannot be isotropic, as argued in Chapter 6, should be defined. **A** series of failure surfaces using the damage parameters can then be constructed based on the degree of damage. These subsequent failure surfaces are important in governing the post-failure behavior of

the material. It is interesting to note that after loading with a sufficiently high stress, ceramics will be comminuted upon load reversal, which completely changes the material properties. On the other hand, ductile materials will be affected by reversal of loading only by the Bauschinger effect. Therefore, the subsequent unloading after a sufficiently high stress level is a very important part of the loading path for ceramic materials. The effect of this part of the loading path needs to be investigated.

(6) Model Ceramic Material

In this research, a dynamic brittle-ductile transition was observed for Macor, but not for the AlN due to the limitations of the experimental facility. Although Macor is a ceramic material, its two-phase composition (glass and mica) makes it an atypical monolithic engineering ceramic. Therefore, it is desirable to find a low strength ceramic material with microstructural features similar to the engineering ceramics to serve as a model material. The experimental investigation of such a material could be performed with the current experimental facility, and the results may provide better understanding of the failure behavior of engineering ceramics. Magnesium Oxide (MgO) may be a good choice due to its low HEL ($-$ 1.5 GPa) and monolithic composition. Duffy and Ahrens (1995) have performed extensive shock wave experiments on MgO, which provides the necessary information regarding its behavior under uniaxial strain.

(7) Strain Measurement

Strains should be measured accurately in the experiments with ceramic materials since they are usually small in magnitude yet very important in obtaining stress-strain curves. The reflected pulse in the incident bar of the SHPB is not expected to give detailed information on the deformation behavior of the specimen because the small axial failure strains of the engineering ceramics such as AlN or Al_2O_3 as mentioned in Chapter 2. A specimen gage approach was introduced in Chapter 2. However, as in the cases of the

electro-magnetic confinement introduced in Chapter 4 and the double sleeve confinement described in Chapter 5, the lateral surface of the specimen was used by the confinement devices, and strain gages could not be mounted on specimens directly. New approaches to measure axial and/or lateral strains of the specimen must be developed. Optical interferometric strain measurement techniques and fiber optic sensors may prove to be viable approaches.

(8) Electo-Magnetic Noise Elimination

The electro-magnetic confinement is an ideal approach to apply dynamic proportional loading as mentioned in Chapter 4. However, further work needs to be done on the current technique of applying electro-magnetic confinement before it can be used to perform extensive experimental research on engineering ceramics. During the discharge of the capacitor bank, the electro-magnetic noise obscured signals obtained from the strain gages mounted on the bars. Since the steel Hopkinson bars are excellent magnetic conductors and are aligned perfectly along the direction of maximum flux of the magnetic field, the strain gages mounted on the Hopkinson bar surfaces inevitably picked up the high amplitude noise signal. Therefore, either the noise should be shielded, or non-electro-magnetic measurement devices such as fiber-optic strain gages should be used.

208 -

7.3 References

Duffy, T. S. and Ahrens, T. J., (1995), "Compressional Sound-Velocity, Equation of State, and Constitutive Response of Shock Compressed Magnesium-Oxide," *J. Geophysical Research Solid Earth*, 100, pp. 529-542.